Liquid Jets for Experiments on Complex Fluids

Dissertation zur Erlangung des Doktorgrades

an der Fakultät für Mathematik, Informatik und Naturwissenschaften
Fachbereich Physik
der Universität Hamburg

vorgelegt von

Ingo Steinke
aus Castrop-Rauxel

Hamburg
2015

Abstract

The ability of modern storage rings and free-electron lasers to produce intense x-ray beams that can be focused down to μm and nm sizes offers the possibility to study soft condensed matter systems on small length and short time scales. Gas dynamic virtual nozzles (GDVN) offer the unique possibility to investigate complex fluids spatially confined in a μm sized liquid jet with high flow rates, high pressures and shear stress distributions. In this thesis two different applications of liquid jet injection systems have been studied. The influence of the shear flow present in a liquid jet on colloidal dispersions was investigated via small angle x-ray scattering and a coherent wide angle x-ray scattering experiment on a liquid water jet was performed. For these purposes, liquid jet setups that are capable for x-ray scattering experiments have been developed and the manufacturing of gas dynamic virtual nozzles was realized. The flow properties of a liquid jet and their influences on the liquid were studied with two different colloidal dispersions at beamline P10 at the storage ring PETRA III. The results show that high shear flows present in a liquid jet lead to compressions and expansions of the particle structure and to particle alignments. The shear rate in the used liquid jet could be estimated to $\dot{\gamma} \geq 5.4 \cdot 10^4$ Hz. The feasibility of rheology studies with a liquid jet injection system and the combined advantages is discussed.

The coherent x-ray scattering experiment on a water jet was performed at the XCS instrument at the free-electron laser LCLS. First coherent single shot diffraction patterns from water were taken to investigate the feasibility of measuring speckle patterns from water.

Zusammenfassung

Die Fähigkeit mit modernen Speicherringen und Freien-Elektronen-Lasern (FEL) intensive und kohärente Röntgenstrahlung auf wenige μm undnm zu fokussieren ermöglichten Studien von Materialien auf kleinen Längen- und kurzen Zeitskalen. Gasfokusierte Düsen, sogenannte "Gas dynamic virtual nozzles" (GDVN) bieten die einzigartige Möglichkeit, komplexe Fluide in einen μm-dünnen Flüssigkeitsstrahl zu untersuchen. Die Bildung des Flüssigkeitsstrahls ist begleitet von hohen Flussraten und Drücken, welche zu Scherungen in der Flüssgkeit führen. In der vorliegenden Arbeit wurden zwei verschiedene Anwendungen von Flüssigkeitsstrahlen untersucht. Der Einfluss des Scherflusses auf kolloidale Dispersionen wurde mit Röntgenkleinwinkelstreuung untersucht und ein Experiment mit kohärenter Röntgenweitwinkelstreuung wurde an einem Wasserstrahl durchgeführt. Hierfür wurden Aufbauten, die es ermöglichen Röntgenstreuexperimente durchzuführen, entwickelt und gebaut. Zusätzlich wurde ein Laborplatz eingerichtet an dem GDVNs gebaut werden können. Die Flusseigenschaften des Flüssigkeitsstrahls und der Einfluss von Scherflüssen auf die Flüssigkeit wurde mit zwei verschiedenen kolloidalen Dispersionen an der Strahllinie P10 am Speichering PETRA III untersucht. Die Ergebnisse zeigten, dass hohe Scherflüsse im Flüssigkeitsstrahl zu Kompressionen und Expansionen der Partikelstruktur und zu Partikelausrichtungen führen. Die Scherrate im Flüssigkeitsstrahl konnte auf $\dot{\gamma} \geq 5.4 \cdot 10^4$ Hz abgeschätzt werden. Hiermit konnte die mögliche Nutzung einer Flüssigkeitsstrahlanlage für Rheologie-Studien gezeigt werden.

Das Röntgenstreuexperiment an Wasser wurde am XCS Instrument am Freien-Elektronen-Laser LCLS durchgeführt. Im rahmen einer Machbarkeitsstudie wurden erste kohärente Diffraktionsbilder von Wasser aufgenommen.

Ein Leben ohne Mops ist möglich, aber sinnlos.

Bernhard-Viktor Christoph-Carl von Bülow

Contents

1 Introduction

The ability of modern storage rings and free-electron lasers to produce intense x-ray beams that can be focused down to μm and nm sizes offers the possibility to study soft condensed matter systems on small length and short time scales.[1] Liquid jets offer the unique possibility to investigate nano-particles spatially confined in a liquid environment and thus avoiding wall effects of a sample chamber.[2] Within the last years such injection systems have become an essential tool for studying liquid samples in high flux scattering experiments.[3] The concept of gas dynamic virtual nozzles (GDVN) using a flow focusing technique is often used in x-ray scattering experiments on complex liquids at modern x-ray sources. Because of the small dimension and flow rates, GDVNs impose high pressure and shear stress distributions onto the liquid jet.[4] The knowledge about shear flow distributions on the liquid sample is essential for x-ray scattering experiments on liquid jets. Colloidal dispersions are sensitive to shear flows by either forming sheared structures[5] or aligned particle structures[6]. This behavior makes it possible to study shear induced effects on distribution on soft condensed matter by probing the structure or alignment of the colloidal particles within the jet. Moreover, liquid jet systems are a promising sample environment for rheology studies on complex fluids under extreme shear flow.

Liquid jets also offer the possibility to study molecular and atomic liquids such as water or liquid metals via x-ray scattering. Their structure can be probed over a wide thermodynamical regime either within the liquid jet or in droplets that are formed when the jet breaks up.[7] The local structure of such sample systems in the liquid phase are up to now controversially

[1]Emma, P. et al. *Nat. Photonics* **4**, (2010), 641.

[2]Deponte, D.P. et al. *J. Phys. D: Appl. Phys.* **41**, (2008), 195505.

[3]Koopmann, R. et al. *Nature Methods* **9**, (2012), 259; Boutet, S. et al. *Science* **337**, (2012), 362; Chapman, H.N. et al. *Nature* **470**, (2011), 73.

[4]A.M.Gañán-Calvo et al. *Phys. Fluids* **26**, (2014), 061701; Lin, S.P. et al. *Annu. Rev. Fluid. Mech.* **30**, (1998), 85.

[5]Vermant, J. et al. *J. Phys.: Condense Matter* **17**, (2005), R187; Brader, J.M. *J. Phys.: Condense Matter* **22**, (2010), 363101; Martys, N.S. et al. *Eur. Phys. J. E* **35**, (2012), 20.

[6]Trebbin, M. et al. *PNAS* **110**, (2012), 6706; Junaid, S. et al. *Langmuir* **26**, (2010), 18701; Gunes, D.Z. et al. *J. Non-Newtonian Fluid Mech.* **155**, (2008), 39.

[7]Sellberg, J. A. et al. *Nature* **510**, (2014), 381; Gañán-Calvo, A.M. et al. *Small* **6**, (2010), 822; Weierstall, U. et al. *Exp. Fluids* **44**, (2008), 675; Faubel, M. et al. *Z. Phys. D* **10**, (1988), 269.

discussed. Coherent x-ray diffraction techniques are a promising tools for studying the local structure of complex liquids.

In this thesis the influence of shear flow present in a liquid jet on colloidal dispersions is studied in order to characterize the flow properties of the liquid jet. For this purpose a setup, which includes diagnostics that are required for measurements with liquid jets, has been developed incorporating gas dynamic virtual nozzles (GDVN). Small angle x-ray scattering (SAXS) experiments have been performed at the storage ring PETRA III to probe shear modified structures of a dispersion of spherical colloids and the alignment of spindle-shaped colloids in a liquid jet. Furthermore, the setup has been designed for coherent x-ray scattering experiments on molecular liquids at free-electron lasers with the pnCCD detector. A first experiment on liquid water was performed with this setup at the free-electron laser LCLS in order to test the feasibility of coherent x-ray diffraction from a thin liquid jet and µm-sized droplets.

The thesis is structured as follows: **Chapter 2** gives the theoretical basis and the background of the experimental methods. The scattering from colloidal particles and the conditions for coherent x-ray scattering experiments are presented. In **chapter 3**, a short introduction to the physics of liquid jets is given. Furthermore, the operating principle of a GDVN is explained and properties of a liquid jet system are described. In **chapter 4**, the studies on colloidal dispersions in the liquid jet are presented. It consists of a short introduction to the physics of colloidal particles in shear flows. SAXS experiments on two different colloidal dispersions in a liquid jet are described. In **Chapter 5** the coherent x-ray scattering experiment on a liquid water jet is presented. At the end of this thesis in **chapter 6**, a summary and an outlook are given.

2 X-ray scattering

The interactions of x-rays with matter offer the possibility to study matter down to the atomic scale. To this end different x-ray methods have been developed to study different properties of matter. X-ray scattering is a method to analyze structural properties. This chapter contains an introduction into the theory of elastic x-ray scattering that is necessary to understand and to interpret the results of the performed experiments.

In section 2.1 the theoretical background of elastic x-ray scattering is introduced. In section 2.2 the scattering from a single particle and in section 2.3 the scattering from many particles are presented. In section 2.4 the coherence of x-ray light and its use for scattering experiments is discussed.

2.1 Elastic scattering

X-ray waves interact with matter via absorption and scattering processes depending on their energy.[1] In this work the interaction can be mostly described by scattering processes. Thus, absorption processes will not be discussed. A typical geometry for a scattering process is shown in figure 2.1. An x-ray wave with an initial wave vector $\vec{k}_i$ and wavelength λ_i is scattered by a sample. After the scattering process the scattered x-ray wave changes its propagation direction by an angle 2θ and propagates with wave vector $\vec{k}_f$ and wavelength λ_f. In the elastic approximation no energy transfer from the x-ray wave to the sample is assumed ($\lambda_i = \lambda_f = \lambda$). The wave vector and the wavelength are connected by $|\vec{k}| = k = \frac{2\pi}{\lambda}$. Due to the change of the propagation direction of the scattered x-ray wave the momentum $\hbar\vec{q}$ is transferred from the x-rays to the sample where $\hbar$ is the reduced Planck constant and $\vec{q}$ is the wave vector transfer. It is defined to be the difference between the final and initial wave vector[2]

$$\vec{q} = \vec{k}_f - \vec{k}_i. \tag{2.1}$$

---

[1] James, R.W. *The optical principles of the diffraction of X-rays.* Bell and sons, London, UK, 1948.
[2] Als-Nielsen, J. *Elements of Modern X-Ray Physics.* Wiley and Sons, Ltd, 2001.
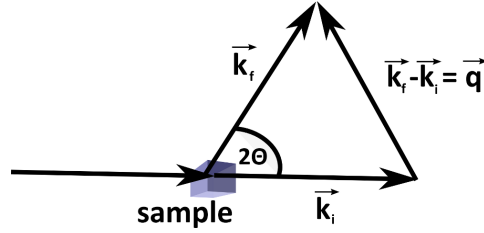
Figure 2.1: Sketch of a scattering process and the wave vector transfer $\vec{q} = \vec{k}_i - \vec{k}_f$.

The modulus of the wave vector transfer $\vec{q}$ is related to the scattering angle 2θ via

$$|\vec{q}| = q = \frac{4\pi}{\lambda} \sin(\theta). \tag{2.2}$$

The scattered intensity $I(\vec{q})$ in a scattering experiment is defined as the number of scattered x-ray photons per unit-time and unit-area and is given by

$$I(\vec{q}) = I_0 \frac{d\sigma}{d\Omega}(\vec{q})d\Omega, \tag{2.3}$$

where $\frac{d\sigma}{d\Omega}$ is the differential scattering cross-section, $d\Omega$ a solid angle increment, and I_0 is the number of incident x-ray photons per unit cross section of the incident beam. The differential scattering cross-section describes the interaction of the sample with the x-ray wave and is given by

$$\frac{d\sigma}{d\Omega} = \frac{\text{number of scattered x-rays into } d\Omega}{\Phi d\Omega}. \tag{2.4}$$

In case of x-ray scattering from a single electron[3] the differential cross-section is given by the classical electron radius $r_e = 2.818 \cdot 10^{-15}$ m and the polarization of the x-rays $p_{\text{x-ray}}$[4]

$$\frac{d\sigma}{d\Omega} = r_e^2 \cdot p_{\text{x-ray}}. \tag{2.5}$$

2.2 Form factor

For x-ray scattering from a single particle, one may describe the involved electrons by an electron density $\rho(\vec{r})$. The scattering from the electron density $\rho(\vec{r})$ is described by the so-called scattering factor $f(\vec{q})$. The scattering factor can be calculated using two approximations. First, in the far-field approximation, it is assumed that the particle size is much smaller than the

---

[3]Known as Thomson scattering

[4]Spieß, L. et al. *Moderne Röntgenbeugung*. B.G. Teubner Verlag/ GWV Fachverlag GmbH, 2005.

sample-detector distance of the scattering experiment. Second, in the first Born approximation, it is assumed that multiple scattering events of photons can be neglected. The scattering factor $f(\vec{q})$ is given by the sum of all contributions $f_j(\vec{q}, \vec{r}_j)$ of all electrons j at positions $\vec{r}_j$ taking into account their corresponding phase shifts $e^{i\vec{q}\cdot\vec{r}}$. For a charge distribution $\rho(\vec{r})$ the scattering factor $f(\vec{q})$ can be expressed by a Fourier transform

$$f(\vec{q}) = \int_V \rho(\vec{r}) e^{i\vec{q}\cdot\vec{r}} d\vec{r}, \tag{2.6}$$

where the limits of the integral are given by the particle volume V. The scattering cross section of a single particle can be written as[5]

$$\frac{d\sigma}{d\Omega} = r_e^2 \cdot \left| f(\vec{q}) \right|^2 \cdot p_{\text{x-ray}}, \tag{2.7}$$

and the scattered intensity within the solid angle $d\Omega$ is given by

$$I(q) = \Phi \cdot r_e^2 \cdot \left| f(\vec{q}) \right|^2 \cdot p_{\text{x-ray}}. \tag{2.8}$$

The absolute square of the scattering factor $f(\vec{q})$ is defined as form factor $P(\vec{q})$.[6] The form factor depends on the electron density and the particle shape. In this thesis particles with two different shapes (sphere and spindle) have been used. Thus, the form factors of these particles are discussed in the following section.

2.2.1 Form factor of spherical particles

For a spherical particle with radius R_0 and a homogenous electron distribution the charge density can be expressed by

$$\rho(\vec{r}) = \begin{cases} \rho_0, & |\vec{r}| \leq R_0 \\ 0, & |\vec{r}| > R_0 \end{cases} \tag{2.9}$$

Because of the particle symmetry the charge density depends only on the modulus $|\vec{r}| = r$. Consequently, the form factor is a function of the modulus of the wave vector transfer $|\vec{q}| = q$.[7] The isotropic particle shape leads to the isotropic $\vec{q}$ dependence of the form factor for a single

---

[5]Als-Nielsen, J. *Elements of Modern X-Ray Physics*. Wiley and Sons, Ltd, 2001.
[6]Spieß, L. et al. *Moderne Röntgenbeugung*. B.G. Teubner Verlag/ GWV Fachverlag GmbH, 2005.
[7]Guinier, A. et al. *Small-Angle Scattering of X-Rays*. New York, USA: Wiley and Sons, Ltd, 1955.

spherical particle

$$P_{\text{single}}(q, R_0) = \left(3 \frac{\sin(qR_0) - qR_0 \cos(qR_0)}{q^3 R_0^3} \right)^2 . \tag{2.10}$$

In figure 2.2 a) the form factor is shown as function of the wave vector transfer q for $R_0 = 20$ nm. At $q = 0$ nm^{-1} the form factor equals 1 ($P(0) = 1$). At values $q > 0$ nm^{-1} the form factor decreases with characteristic oscillations depending upon R_0. The asymptotic behavior of the form factor is proportional to a power law $P(q) \propto q^{-4}$, see figure 2.2 b). The experiments in
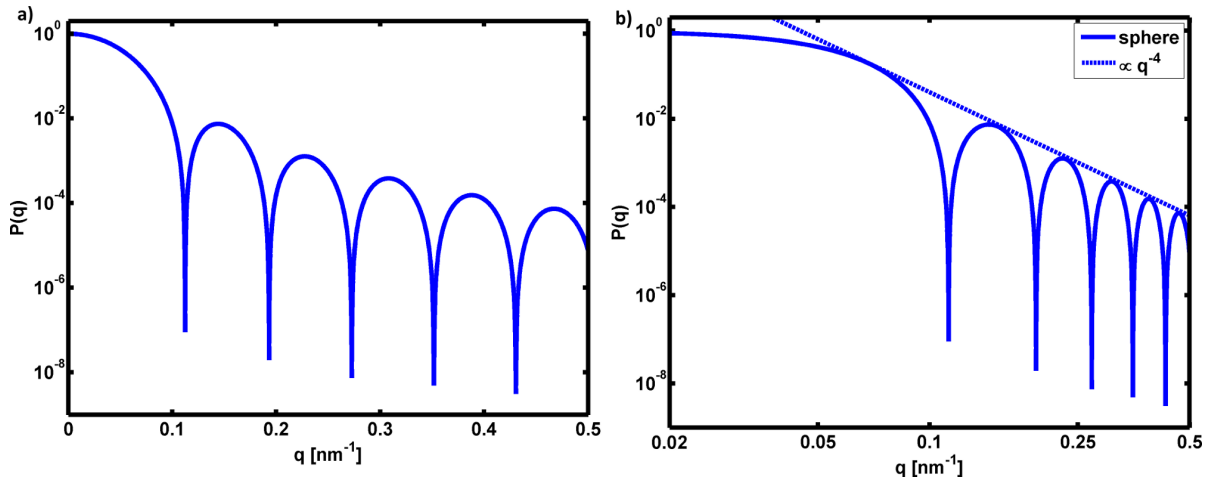

Figure 2.2: a) Calculated form factor of a spherical particle as function of the wave vector transfer q in linear scale. b) Form factor of a spherical particle as function of the wave vector transfer q in logarithmic scale. Additionally a power law with exponent -4 is plotted.

this work were performed with dispersions of polydisperse particles. For such sample systems a Schulz-Flory distribution function was used to model the size distribution $c(R, R_0, Z)$ with mean radius R_0 and width ΔR. It is given by[8]

$$c(R, R_0, Z) = \frac{1}{\Gamma(Z+1)} \left(\frac{Z+1}{R_0} \right)^{Z+1} R^Z \cdot e^{-\frac{Z+1}{R_0}}, \tag{2.11}$$

where Γ is the gamma function and the parameter Z is related to the polydispersity p. It is given by

$$p = \frac{\Delta R}{R_0} = \sqrt{\frac{1}{Z+1}}. \tag{2.12}$$

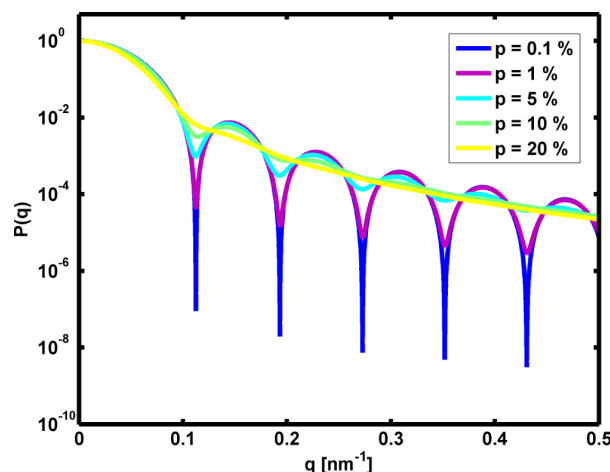[8]Schulz, G. Z. *Phys. Chem.* **46**, (1949), 155.

Figure 2.3: Calculated form factors using equation 2.13 with radius $R = 40\,\mathrm{nm}$ and different polydispersities p.

Using the size distribution the form factor can be written as

$$P(q, R_0, Z)_{\mathrm{poly}} = \int_0^\infty c(R, R_0, Z) P_{\mathrm{single}}(q, R) dR. \qquad (2.13)$$

In figure 2.3 form factors with different degrees of polydispersity are shown. For small polydispersities the form factor is comparable to the form factor in figure 2.2 a). With increasing p the oscillations of the form factor are smeared out due to the averaging of form factors arising from spheres with slightly different sizes.

A comprehensive list of various different form factors arising from different geometries can be found in literature.[9] For a non-spherical particle shape the particle orientation influences the form factor. The form factor of spindle-shaped particles is presented in the following section.

2.2.2 Form factor of spindle-shaped particles

A model for the form factor of a spindle-shaped particle has been published recently.[10] The particle shape can be described as a body of revolution resulting from two intersecting circles with the radius R_2. In figure 2.4 a) the geometry of a spindle with a major semi-axis L and a minor semi-axis R_1 is depicted. The minor semi-axis is parallel to the x-axis, while the major semi-axis is parallel to the z-axis. As this is a non-spherical geometry for $L \neq R_1$ the form

---

[9]Lindner, P. et al. *Modelling of small-angle scattering: Data from colloids and polymer systems.* New York, USA: Elsevier Science, 2002. Chap. X-Ray and Light: Scattering Methods Applied to Soft Condensed Matter; Mittelbach, P. *Acta Physica Austriaca* **19**, (1964), 54.

[10]Märkert, C. et al. *J. App. Cryst.* **44**, (2011), 441.

factor will be anisotropic. Thus, the orientation of the wave vector transfer $\vec{q}$ relative to the particle has to be considered. The coordinates of the wave vector transfer $\vec{q}$ are shown in figure 2.4 b). The angle θ_q defines the orientation of the wave vector transfer $\vec{q}$ relative to the major particle axis. For $\theta_q = \frac{\pi}{2}$ it is perpendicular to the major semi-axis, while it is parallel for $\theta_q = 0$. The form factor is independent from the angle ϕ_q because of the particle symmetry along the z-axis. The form factor can be expressed for a single spindle-shaped
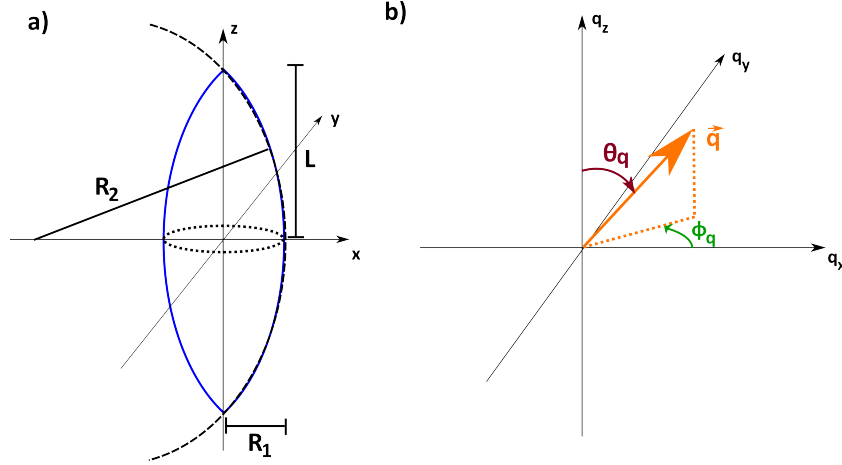

Figure 2.4: a) Sketch of the geometry of a spindle-shaped particle. b) Sketch of the spherical coordinates of the wave vector transfer $\vec{q}$.

particle by

$$
P_{\text{single}}(q, \theta_q, R_1, R_2, \nu) = \left(\frac{4\pi}{V(R_1, \nu)} \int_0^{L/2} \cos(qz \cos(\theta_q)) \frac{R_1 - R_2 + (R_2^2 - z^2)^{\frac{1}{2}}}{q \sin(\theta_q)} \right.
$$
$$
\left. \cdot J_1 \left\{ q \sin(\theta_q) \left[R_1 - R_2 + (R_2^2 - z^2)^{\frac{1}{2}} \right] \right\} dz \right)^2, \quad (2.14)
$$

where $V(R_1, \nu)$ is the particle volume, J_1 is the Bessel function of the first kind, dz is a differential increment of L, and the radius R_2 is given by $R_2 = (L^2 + R_1^2)/4R_1$. The particle volume is given by

$$
V(R_1, \nu) = \frac{2\pi}{3} \left\{ \frac{(2R_1)^3}{8} \nu \left[\frac{3}{4} \left(1 + \nu^2 \right)^2 - \nu^2 \right] \right\} +
$$
$$
\frac{2\pi}{3} \left\{ \frac{3(2R_1)^3}{32} \left(1 + \nu^2 \right)^2 \left[1 - \frac{1}{2} \left(1 + \nu^2 \right) \right] \arcsin\left(\frac{2\nu}{1 + \nu^2} \right) \right\}, \quad (2.15)
$$

where $\nu = \frac{L}{R_1}$ is the aspect ratio. The form factor of a single spindle-shaped particle depends on the particle geometry (R_1, L), the modulus of the wave vector transfer $q = |\vec{q}|$, and the
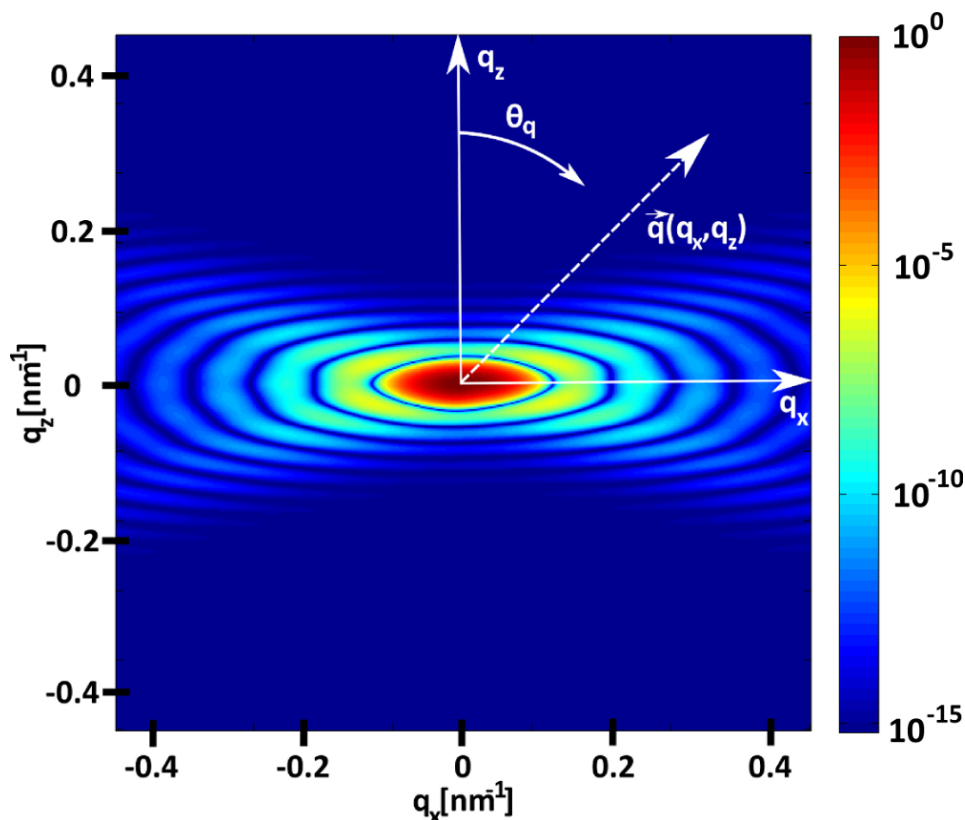
Figure 2.5: Calculated form factor of a spindle-shaped particle aligned parallel to the q_z-axis with $L = 160\,\text{nm}$, $R_1 = 40\,\text{nm}$ and $p = 0.1$. The form factor is normalized to the maximum. It is at $q_x = q_z = 0$.

orientation of the wave vector transfer $\vec{q}$ relative to the major semi-axis of the particle, see equation 2.14. The form factor is normalized to the volume of the particle to ensure that $\lim\limits_{q\to 0} P(q) = 1$. In the experiment performed in this work the particle size varies slightly and influences the form factor. To consider this polydispersity a Schulz-Flory distribution (equation 2.11) can be used to modulate the size of the minor semi-axis.[11] The form factor with the distribution is given by

$$P_{\text{poly}}(q,\theta_q,R_1,R_2,Z,\nu) = \frac{1}{\langle V^2 \rangle} \int_0^\infty c(R,R_1,Z)V^2(R,\nu) \cdot P_{\text{single}}(q,\theta_q,R,R_2,\nu)dR, \quad (2.16)$$

with

$$\langle V^2 \rangle = \int_0^\infty c(R,R_1,Z)V^2(R,\nu)dR. \quad (2.17)$$

---

[11] Wagner, J. *J. Appl. Cryst.* **37**, (2004), 750.

Integration of equation 2.17 yields

$$\langle V^2 \rangle = \frac{1}{9216} \frac{\Gamma(Z+7)}{\Gamma(Z+2)} \cdot \frac{1}{(Z+1)^5} \pi^2 R_1^6$$
$$\left[3 \arcsin\left(\frac{2\nu}{1+\nu^2} \right)(\nu^6 + \nu^4 - \nu^2 - 1) - 2(3\nu^5 + 2\nu^3 + 2\nu) \right]^2 \quad (2.18)$$

An example of the form factor calculated with equation 2.16 for $L = 160\,\text{nm}$, $40\,\text{nm}$, $p = 0.1$, and $\phi_q = 0$ is shown in figure 2.5. The form factor is anisotropic reflecting to the anisotropic particle shape shown in figure 2.4 a). Line profiles of the form factor for different θ_q values are shown in figure 2.6 a). The periodicity of the form factor oscillations differ for different θ_q values. For $\theta_q = 0$ (along the q_z-axis) the period of the oscillations is shorter as compared to the period for $\theta_q = \pi/2$ (along the q_x-axis). Furthermore, the asymptotic behavior is different for different θ_q values, see figure 2.6 b). For $\theta_q = 0$ the form factor falls proportional to a power law $(P(q, \theta_q = 0) \propto q^n)$ with exponent $n = -6$. At $\theta_q = \pi/2$ the form factor falls proportional to a power law with exponent $n = -4$. For $0 < \theta_q < \frac{\pi}{2}$ the form factor falls proportional to a power law with exponents between $n = -4$ and $n = -6$. The decay of the exponent n at $\theta_q = 0$ is a function of the aspect ratio of the particle. It can be approximated by an exponential[12]

$$n = -6 + 2 \cdot \exp\left[-\alpha(\nu - 1)^\beta \right], \quad (2.19)$$

with the parameters $\alpha = 1.555$ and $\beta = 0.855$. This empirical formula is plotted in figure 2.7. The decay of the exponent of the asymptotic power law reaches the value $n = -6$ at aspect ratios $\nu > 4$. At $\nu = 1$ the asymptotic behavior is similar to the asymptotic behavior of a sphere $(n = -4)$. The example shown in figure 2.5 corresponds to a particle with an aspect ratio of $\nu = \frac{40\,\text{nm}}{160\,\text{nm}} = 4$. Thus the form factor $P(q, \theta_q = 0)$ falls proportional to a power law with exponent $n = -6$, see figure 2.6 b). The anisotropy of the form factor can be visualized with the help of profiles along a semi-circle $(0 < \theta_q < \frac{\pi}{2})$ for a constant q. Such profiles are shown in figure 2.8 for $q = 0.05\,\text{nm}^{-1}$ and different aspect ratios and polydispersities. One observes peaks with angular widths $\Delta\theta_q$. These widths $\Delta\theta_q$ are influenced by the particle shape, see figure 2.8 a). The angular width $\Delta\theta_q$ increases as the aspect ratio increases. This indicates, that the form factor (shown in figure 2.5) becomes more isotropic for increasing aspect ratio ν, while it gets wider for decreasing ν. For $\nu = 1$ the particle is a sphere and the form factor is isotropic. For increasing polydispersity the angular width $\Delta\theta_q$ of the form factor increases and the scattering strength of the form factor decreases, see figure 2.8 b). This

---

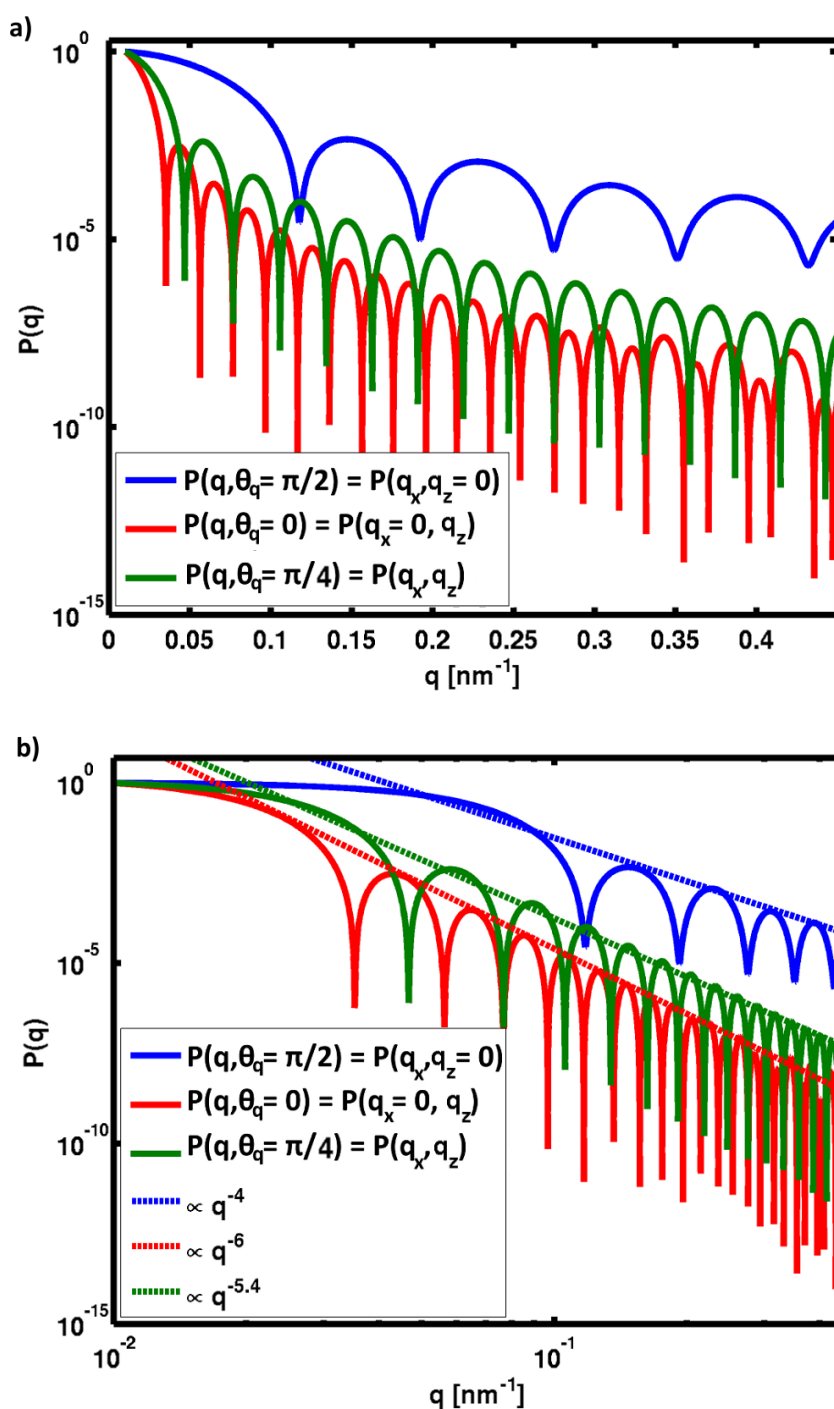[12]Märkert, C. et al. *J. App. Cryst.* **44**, (2011), 441.

Figure 2.6: Line profiles of the calculated form factor in figure 2.5. a) Form factors at different θ_q values as function of the wave vector transfer q. b) Asymptotic behavior of the form factors. Furthermore, three power laws are plotted. The calculations have been performed using $L = 160\,\text{nm}$, $R_1 = 40\,\text{nm}$ and $p = 0.1$.
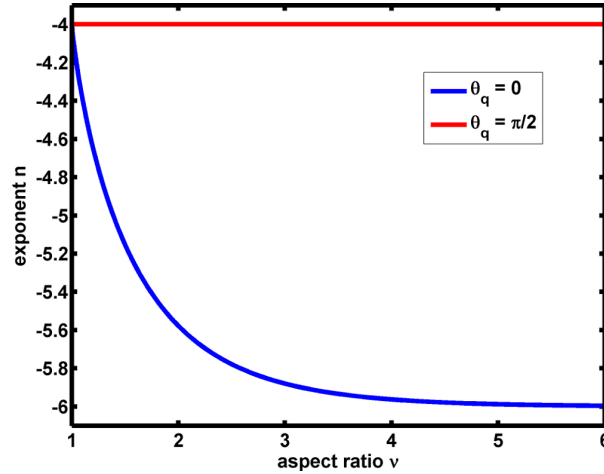
Figure 2.7: Exponent of the power law $P(q, \theta_q) \propto q^n$ as function of the aspect ratio ν. The exponent is shown for $P(q, \theta_q = 0) = P(q_z)$ and for $P(q, \theta_q = \pi/2) = P(q_x)$.

is expected since the polydispersity describes a change of the particle size and thus a change of the aspect ratio. Therefore, the plots in figure 2.8 b) describe a convolution of slightly different particle geometries.

So far in this section the form factor of spindle-shaped particles with a single orientation was considered, see figure 2.4 a). Now, particles with different orientations are considered. As the form factor depends on the angle enclosed of the major semi-axis and the wave vector transfer $\vec{q}$, a transformation of the coordinates is necessary. In the case shown in figure 2.4 a) the enclosed angle between the major semi-axis and $\vec{q}$ is θ_q. This is not the case for other particle orientations. Thus, spherical coordinates describing the particle orientation are introduced, see figure 2.9 a). Here, the unit vector $\vec{g}(\theta_g, \phi_g)$ describes the orientation of the major semi-axis of the particles, see figure 2.9 b). The angle enclosed by $\vec{g}$ and $\vec{q}$ is ζ. It can be obtained via the addition theorem of spherical harmonics[13]

$$\cos(\zeta) = \cos\theta_q \cos\theta_g + \sin\theta_q \sin\theta_g \cos\phi_g. \tag{2.20}$$

The form factor of a particle with orientation $\vec{g}(\theta_g, \phi_g)$ can be calculated by substituting the angle θ_q with the angle ζ in equation 2.16. The particle orientation that was discussed in the beginning of this section is described by $\theta_g = 0$, see in figure 2.4 a). Because of the particle symmetry the angle ϕ_g does not influence the form factor in this particle orientation. As can be seen from equation 2.20 for $\theta_g = 0$ the angle ζ equals θ_q, which is in line with the form factor description above. Three examples for different particle orientations ($\theta_g = 0$,

---

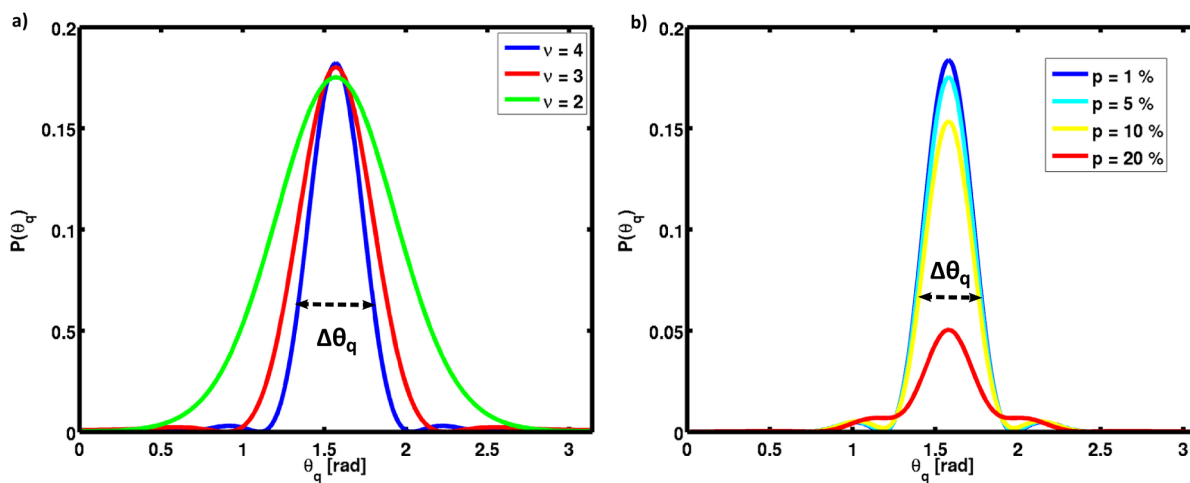[13]Bronstein, I.N. et al. *Taschenbuch der Mathematik*. Frankfurt am Main: Harri Deutsch GmbH, 2005.

Figure 2.8: Profiles along a semi-circle of a two dimensional form factor at constant $q = 0.1\,\mathrm{nm}^{-1}$. a) The influence of the particle shape on the width $\Delta\theta_q$ for $p = 0.1$ and $R_1 = 40\,\mathrm{nm}$. b) Influence of the polydispersitie on the width $\Delta\theta_q$ for $L = 160\,\mathrm{nm}$, $R_1 = 40\,\mathrm{nm}$.
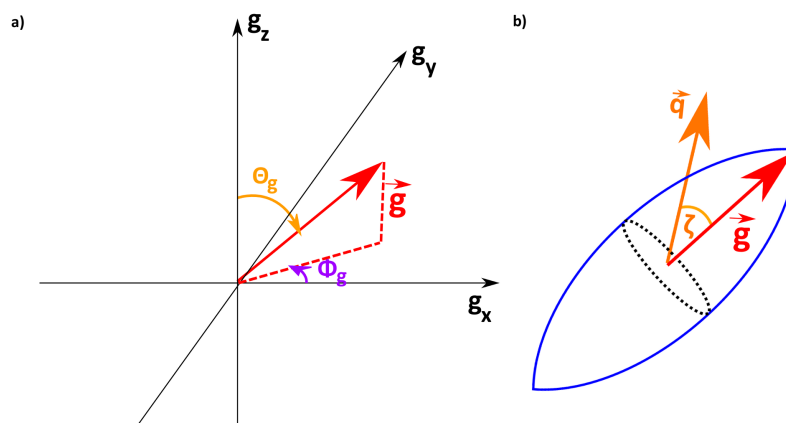

Figure 2.9: a) Sketch of spherical coordinates to describe the orientation of spindle shape particles. b) Sketch of the particle orientation $\vec{g}$ relative to the wave vector transfer $\vec{q}$.
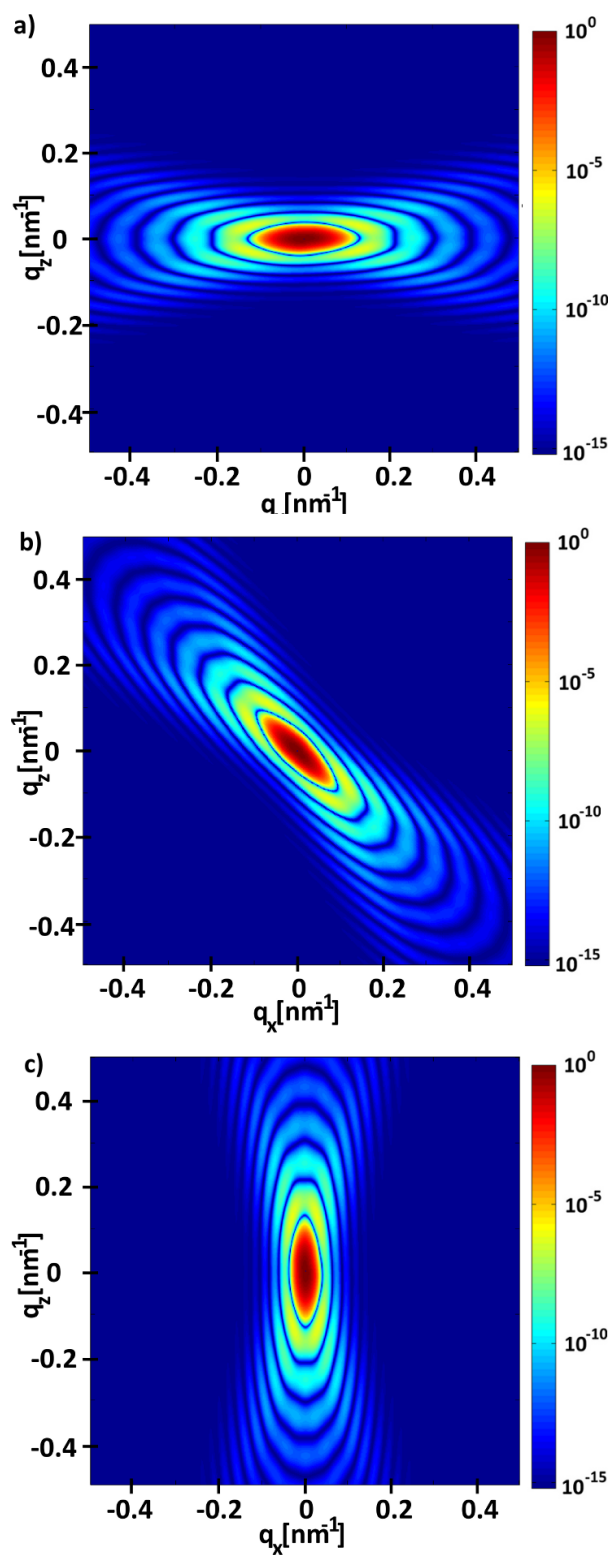
Figure 2.10: Calculated form factors for different particle orientations using $L = 160\,\text{nm}$, $R_1 = 40\,\text{nm}$, $p = 0.1$, and $\phi_g = 0$. a) $\theta_g = 0$, b) $\theta_g = \frac{\pi}{4}$, c) $\theta_g = \frac{\pi}{2}$. The calculation was done with equation 2.16 and angle ζ instead of angle θ_q.

$\theta_g = \frac{\pi}{4}, \theta_g = \frac{\pi}{2}$) are shown in figure 2.10. The form factor changes relative to the particle orientation $\vec{g}(\theta_g, \phi_g)$. Thus, the particle orientation can be deduced out of the observation of the form factor.

With the spherical coordinates of figure 2.9 a) an orientation distribution function (ODF) $f(\theta_g, \phi_g)$ can be formulated to calculate form factors originating from particles with different orientations. The form factor of spindle-shaped particles with an ODF is given by

$$P_{\text{dist}}(q, \zeta, R_1, R_2, Z, \nu) = \int_0^{2\pi} \int_0^{\pi} f(\theta_g, \phi_g) P_{\text{poly}}(q, \zeta, R_1, R_2, Z, \nu) \sin \theta_g \, d\theta_g \, d\phi_g. \quad (2.21)$$

Inserting equation 2.16 into equation 2.21 it can be written as

$$P_{\text{dist}}(q, \theta_q, R_1, L, Z, \nu) = \int_0^{2\pi} \int_0^{\pi} f(\theta_g, \phi_g) \left(\frac{1}{9216} \frac{\Gamma(Z+7)}{\Gamma(Z+2)} \cdot \frac{1}{(Z+1)^5} \pi^2 R_1^6 \right)^{-1} \left[3 \arcsin \left(\frac{2\nu}{1+\nu^2} \right) \right.$$

$$(\nu^6 + \nu^4 - \nu^2 - 1) - 2(3\nu^5 + 2\nu^3 + 2\nu) \right]^{-2} \int_0^{\infty} \frac{1}{\Gamma(Z+1)} \left(\frac{Z+1}{R_1} \right)^{Z+1} R^Z \cdot e^{-\frac{Z+1}{R_1}} \left(4\pi \int_0^{L/2} \cos(qz) \right)$$

$$\cos \theta_q \cos \theta_g + \sin \theta_q \sin \theta_g \cos \phi_g) \frac{R - \left(\frac{L^2+R^2}{4R} \right) + \left(\left(\frac{L^2+R^2}{4R} \right)^2 - z^2 \right)^{\frac{1}{2}}}{q \sin(\arccos(\cos \theta_q \cos \theta_g + \sin \theta_q \sin \theta_g \cos \phi_g))}$$

$$J_1 \left\{ q \sin(\arccos(\cos \theta_q \cos \theta_g + \sin \theta_q \sin \theta_g \cos \phi_g)) \left[R - \left(\frac{L^2+R^2}{4R} \right) + \left(\left(\frac{L^2+R^2}{4R} \right)^2 - z^2 \right)^{\frac{1}{2}} \right] \right\} dz \right)^2$$

$$dR \sin \theta_g \, d\theta_g \, d\phi_g \quad (2.22)$$

With equation 2.22 the scattering signal of spindle-shaped particles with major semi-axis L, minor semi-axis R_1, and polydispersity $p = \sqrt{\frac{1}{Z+1}}$ can be calculated for a given orientation distribution function $f(\theta_g, \phi_g)$. One possible approach for an ODF is a Gaussian distribution

$$f(\theta_g, \phi_g) = \exp \left(-1 \cdot \left(\frac{[\theta_g - \theta_{g,c}]^2}{\sigma_{\theta,s}} + \frac{[\phi_g - \phi_{g,c}]^2}{\sigma_{\phi,s}} \right) \right), \quad (2.23)$$

where $\theta_{g,c}$ and $\phi_{g,c}$ are the center locations with $\sigma_{\phi,s}$ and $\sigma_{\theta,s}$ as standard deviations. The degree of alignment of the particles is described by the full width at half maximum of the Gaussian distribution. In the following the particles are assumed to be randomly oriented about angle θ_g. Thus the standard deviation yields $\sigma_{\theta,s} \to \infty$ and the first term in the exponent
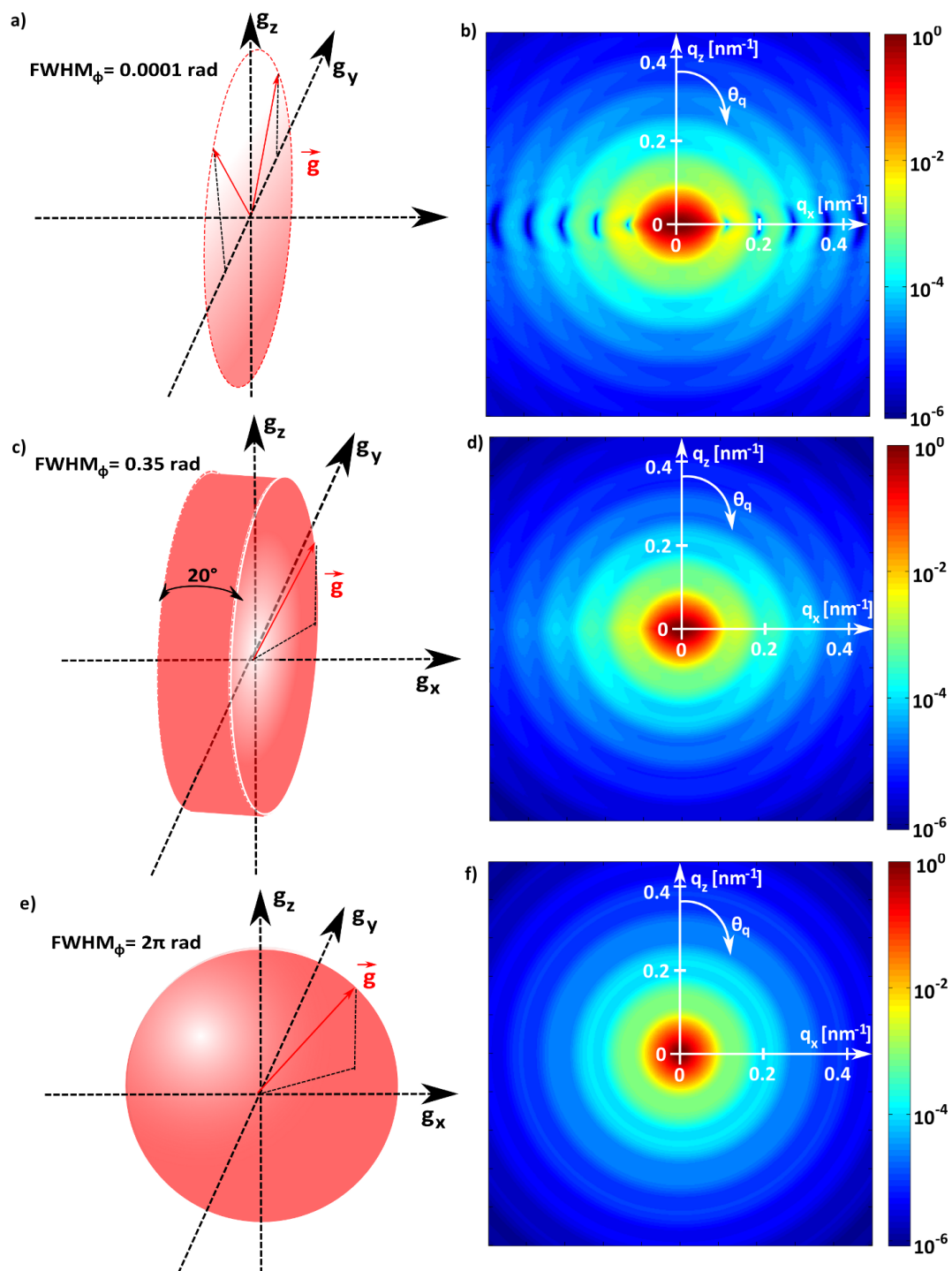
Figure 2.11: Calculated form factors of spindle-shaped particles with different orientations described by the ODF in equation 2.23 using $L = 160$ nm, $R_1 = 40$ nm, $p = 0.01$. The ODFs are schematically shown in a), c), and d). The volume that is covered by the ODF is colored red. b) Form factor with $FWHM_\phi = 0.0001$ rad b) Form factor with $FWHM_\phi = 0.35$ rad(20°) c) Form factor with $FWHM_\phi = 2\pi$ rad.
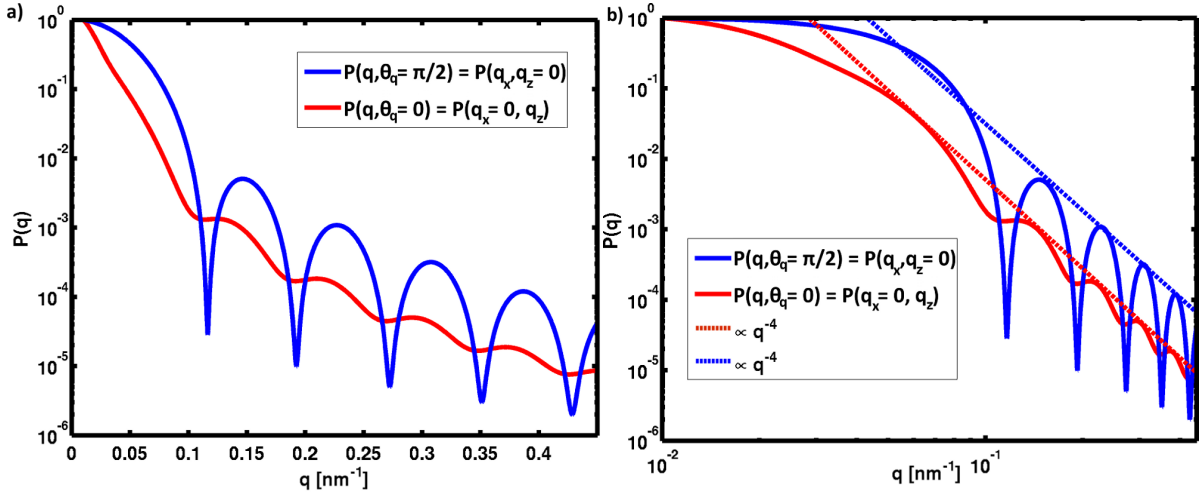
Figure 2.12: a) Line profiles of the form factor shown in figure 2.11 a) along the q_z-axis and the q_x-axis. b) Asymptotic behavior of the cuts of the form factor as function of wave vector transfer. The ODF of the particles is given by $\text{FWHM}_\phi = 0.0001\,\text{rad}$ and $\phi_{g,c} = \frac{\pi}{2}$.

in equation 2.23 reduces to 0. With this convention all particle orientations with $0 < \theta_g < \pi$ are possible. In the following the particle orientation about angle ϕ_g is considered with the full with at half maximum $\text{FWHM}_\phi = 2\sqrt{2\ln 2} \cdot \sigma_{\phi,s}$. Three examples ($\text{FWHM}_\phi = 0.0001\,\text{rad}$, $\text{FWHM}_\phi = 0.35\,\text{rad}$, $\text{FWHM}_\phi = 2\pi$,) of the form factor with the ODF were calculated with equation 2.23 and 2.22. The results are shown in figure 2.11. In appendix A.2 the numerical calculation of the shown results is explained.

The calculated form factor for a narrow distribution ($\text{FWHM}_\phi = 0.0001\,\text{rad}$ and $\phi_{g,c} = \frac{\pi}{2}$) represents an complete alignment of the minor particle semi-axis parallel to the g_x-axis (see figure 2.9). With $\phi_g = \frac{\pi}{2}$ equation 2.20 simplifies to $\cos(\zeta) = \cos(\theta_g)\cos(\theta_q)$. The angle between the q_x-axis ($\theta_q = \frac{\pi}{2}$) and $\vec{g}$ is $\zeta = \frac{\pi}{2}$, see figure 2.11 b). Thus, the form factor along the q_x-axis is described by a single angle ζ, while along the q_z-axis ($\theta_q = 0$) it is given by $\cos(\zeta) = \cos(\theta_g)$. Thus, at the q_z-axis all particle orientations θ_g contribute with different ζ to the form factor, while at the q_x-axis all particle orientations θ_g contribute with $\zeta = \frac{\pi}{2}$. Line profiles along the q_z-axis and the q_x-axis are shown in figure 2.12 a). The form factor along the q_x-axis shows pronounced oscillations, while along the q_z-axis the oscillations are smeared out due to the average of form factors originating from particles with different orientations. This is also visible in the form factor shown in figure 2.11 b). The form factor along both axes falls asymptotically to a power law with exponent $n = -4$, see figure 2.12 b). This differs from the form factor of a spindle-shaped particle with a single orientation. The exponential decrease with exponent $n = -6$ does not occurs due to the average of different particle orientations. As the form factor along the q_x-axis is described by a single particle orientation $\zeta = \frac{\pi}{2}$ the
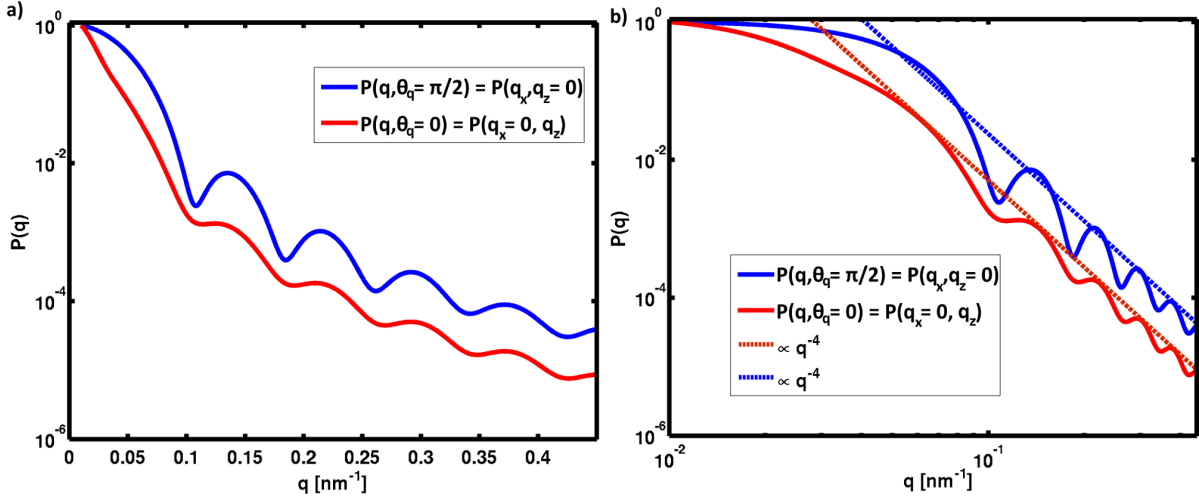
Figure 2.13: a) Line profiles of the form factor shown in figure 2.11 b) along the q_z-axis and the q_x-axis. b) Asymptotic behavior of the cuts of the form factor as function of wave vector transfer. The ODF of the particles is given by $\mathrm{FWHM}_\phi = 0.35\,\mathrm{rad}$ and $\phi_{g,c} = \frac{\pi}{2}$.

plotted graph for $P(q_x, q_z = 0)$ in figure 2.12 is identical with the graph $P(q_x, q_z = 0)$ showing the form factor of a particle with a single orientation in figure shown in figure 2.6. Thus, in an experiment with a particle orientation about one angle (equation 2.16) the form factor can be fitted with the form factor of a particle with a single orientation. Experimentally, such an ODF is present when spindle-shaped hematite particles become aligned due to a magnetic field. In this case the minor semi-axis is aligned parallel to the magnetic field and the major semi-axis can rotate perpendicular to the field.

The form factor calculated with $\mathrm{FWHM}_\phi = 0.35\,\mathrm{rad}$ (20°) and $\phi_{g,c} = \frac{\pi}{2}$ describes particles that do not show a full alignment of their minor semi-axis parallel to the g_x-axis, see figure 2.11 d). Thus, the scattering signal of particles with this ODF exhibit smeared compared to figure 2.11 a). However the anisotropy of the form factor is still visible. Along the q_x-axis where $\theta_q = \frac{\pi}{2}$ the equation 2.20 simplifies to $\cos(\zeta) = \sin(\theta_g)\cos(\phi_q)$, while along the q_z-axis ($\theta_q = 0$) the equation 2.20 is reduced to $\cos(\zeta) = \cos(\theta_g)$. Therefore, the form factor along the q_z-axis is described by an average of form factors of particles with orientations θ_g and the form factor along the q_x-axis is restricted by the Gaussian distribution about angle ϕ_g. The form factors along these axes are shown in figure 2.13. Along the q_z-axis the form factor is identical with the form factor along the q_z-axis in figure 2.12. This is expected since both form factors are described by $\cos(\zeta) = \cos(\theta_g)$. The change of the ODF does not influence the form factor along the q_z-axis. However, the ODF leads to an average over different form factors originating from particles with different orientations about angle ϕ_g. The form factor along the q_x-axis shown in figure 2.13 differs from the form factor along the q_x-axis in figure
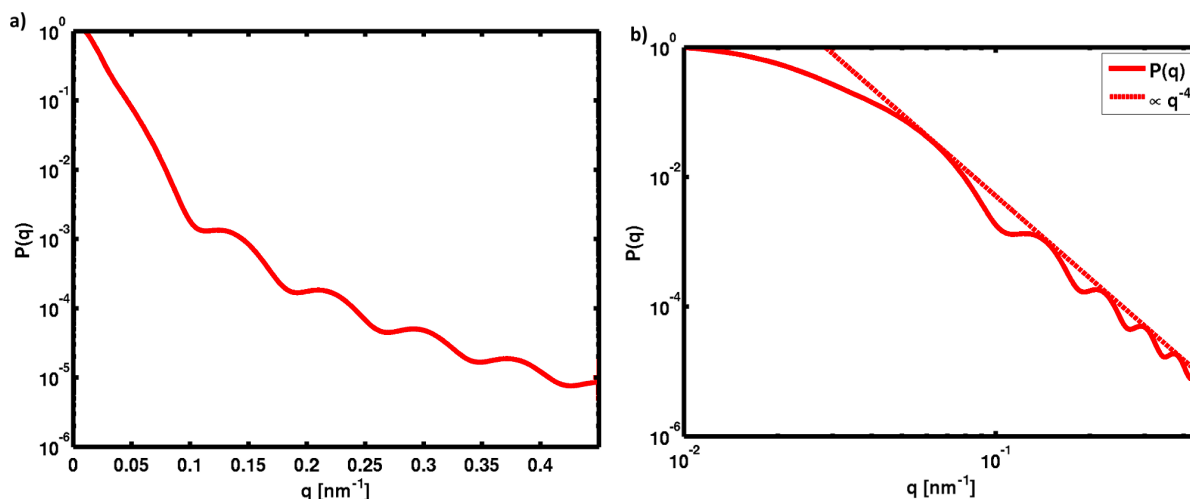
Figure 2.14: a) Line profile of the form factor shown in figure 2.11 c) along the q_z-axis and the q_x-axis. b) Asymptotic behavior of the line profiles of the form factor as function of wave vector transfer.

2.12. The oscillations are less pronounced and the form factors exhibit a smeared shape. Because of the average of form factors with different particle orientations, both form factors shown in figure 2.13 falls asymptotically to a power law with exponent $n = -4$.

The form factor calculated with $\text{FWHM}_\phi = 2\pi$ and $\phi_{g,c} = \frac{\pi}{2}$ describes a random particle orientation, see figure 2.11 f). The particles are orientated about the angle $0 < \theta_g < \pi$ and $0 < \phi_g < 2\pi$. Therefore, every particle orientation is allowed in this case. Along the q_z-axis the angle enclosed by the particle orientation $\vec{g}$ and the wave vector transfer $\vec{q}$ is given by $\cos(\zeta) = \cos(\theta_g)$, while along the q_x-axis it is $\cos(\zeta) = \sin(\theta_g)\cos(\phi_q)$. As the ODF allows every particle orientation the form factors along both axis are identical and the scattering signal is isotropic, see figure 2.11 f). A line profile of the form factor is shown in figure 2.14. The form factor shown in figure 2.14 is identical to the form factor shown in figure 2.12 along the q_z-axis. This is reasonable because along this axis form factors of all particle orientations are averaged, while form factors of all particle orientations are averaged for every θ_q in figure 2.11 f). Furthermore, the form factor falls asymptotically to a power law with exponent $n = -4$, see figure 2.14 b).

Besides line profiles, the angular width $\Delta\theta_q$ of the form factor is influenced by the orientation distribution of the particles. An example is shown in figure 2.15 for $q = 0.05\,\text{nm}^{-1}$ using $L = 160\,\text{nm}$, $R_1 = 40\,\text{nm}$, $p = 0.01$. The angular width $\Delta\theta_q$ of the form factor changes as function of the FWHM_ϕ of the ODF. Beside the intrinsic angular width of the form factor, which arises from the particle shape (see figure 2.8), the orientation distribution of the particles leads to an increase of the angular width $\Delta\theta_q$ of the form factor proportional to
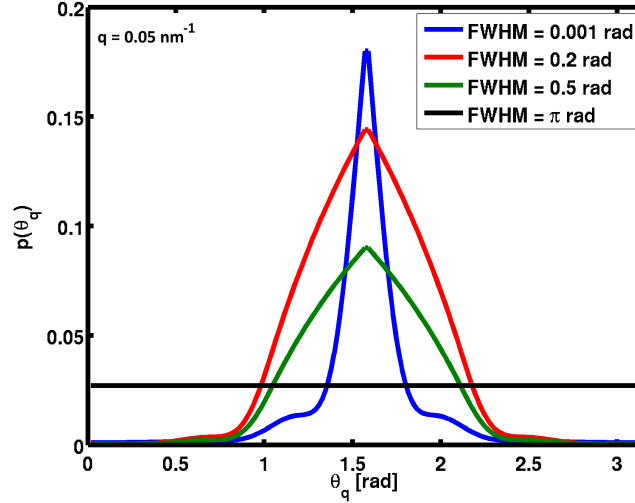
Figure 2.15: Calculated form factors as function of θ_q for different FWHM_ϕ of the ODF. The calculation was carried out using $L = 160\,\text{nm}$, $R_1 = 40\,\text{nm}$, $p = 0.01$, and equation 2.22.

the FWHM_ϕ of the distribution function. For $\text{FWHM}_\phi = 0.001\,\text{rad}$ the angular width $\Delta\theta_q$ is comparable to the angular width of the form factor of a particle with a single orientation (compare figure 2.15 and 2.8). This ODF describes a distribution of particles with minor semi-axis parallel to the g_x-axis. The angular width $\Delta\theta_q$ is therefore less influenced by the ODF. For large FWHM_ϕ values the angular width increases. Moreover, the height of the maximum decreases and smears out. At a random distribution of the particle orientation the maximum vanishes and the angular width $\Delta\theta_q \rightarrow 2\pi$. The angular width is thus a measure for the FWHM_ϕ of the ODF.

2.3 Structure factor

The description of the differential scattering cross section for a system with N particles is given by a sum of the scattering factors $f_j(\vec{q})$ and their corresponding phase shift

$$\frac{d\sigma}{d\Omega}(\vec{q}) = \left| \sum_{j=1}^{N} f_j(\vec{q}) e^{i\vec{q}\cdot\vec{r}_j} \right|^2 = \sum_{h,j}^{N} f_h(\vec{q}) f_j^*(\vec{q}) e^{i\vec{q}\cdot\vec{r}_{hj}}, \qquad (2.24)$$

where the vector $\vec{r}_{hj} = \vec{r}_h - \vec{r}_j$ is the relative position of the particles h and j. Assuming that there is no correlation between the scattering factors and positions of different particles in the sample and $f_h(\vec{q}) f_j^*(\vec{q}) = |f(\vec{q})|^2$ for $f_h(\vec{q}) = f_j(\vec{q})$, the differential cross section in equation

2.24 is given by[14]

$$\frac{d\sigma}{d\Omega}(\vec{q}) = |f(\vec{q})|^2 \sum_{i,j\neq h}^{N} e^{i\vec{q}\cdot\vec{r}_{hj}} + Nf^2(\vec{q}). \tag{2.25}$$

This is valid for identical spherical particle. Equation 2.25 is separated into two different terms. The sum describes the contribution of the diffraction interference from scattering from different particles while the second term describes the contribution of the isotropic diffraction from an individual particle. The first term of the differential cross-section can be expressed by a dimensionless interference function[15]

$$H(\vec{q}) = \frac{1}{N} \sum_{h,j\neq h}^{N} e^{i\vec{q}\cdot\vec{r}_{hj}}, \tag{2.26}$$

which converges for a disordered structure to 0 for $q \to \infty$. The scattering cross-section can be written as

$$\frac{1}{N}\frac{d\sigma}{d\Omega}(\vec{q}) = |f(\vec{q})|^2 H(\vec{q}) + f^2(\vec{q}), \tag{2.27}$$

which shows that the scattering signal is given by scattering from single scattering centers by $f^2(\vec{q})$ and by an interference term $f^2(\vec{q})H(\vec{q})$. The interference term can be expressed with the so called static structure factor. It is given by

$$S(\vec{q}) = \frac{1}{N} \sum_{h,j}^{N} e^{i\vec{q}\cdot\vec{r}_{hj}} = H(\vec{q}) + 1, \tag{2.28}$$

which converges to 1 for $q \to \infty$. The differential cross-section is now given by

$$\frac{1}{N}\frac{d\sigma}{d\Omega} = |f(\vec{q})|^2 \cdot S(\vec{q}). \tag{2.29}$$

Thus, the scattering signal is a product of the form factor and the structure factor. The structure of a sample can be described in real space in terms of the so-called radial pair-distribution function $g(|\vec{r}|)$. It is proportional to the probability of finding a particle at a distance $|\vec{r}|$ relative to a reference particle, see figure 2.16. The structure factor $S(|\vec{q}|)$ and the radial pair-distribution function $g(|\vec{r}|)$ are related by a Fourier transform

$$S(q) - 1 = \rho_0 \int [g(r) - 1]e^{iq\cdot r} dr, \tag{2.30}$$

---

[14]Glatter, O. et al. *Small Angle X-ray Scattering*. Academic Press INC., New York, 1982.
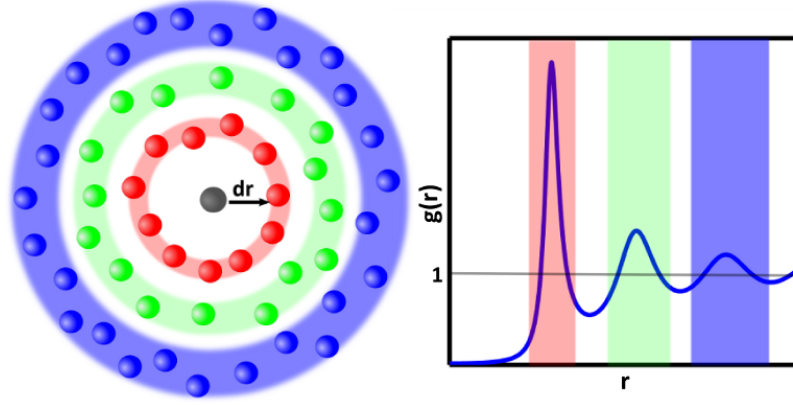[15]Als-Nielsen, J. *Elements of Modern X-Ray Physics*. Wiley and Sons, Ltd, 2001.

Figure 2.16: Schematic description of the pair distribution function g(r).

and

$$g(r) - 1 = \frac{1}{\rho_0 \cdot (2\pi)^3} \int [S(q) - 1] e^{-iq \cdot r} dq, \tag{2.31}$$

where ρ_0 is the density of scattering centers. Thus, the structure factor describes the structure of particles in Fourier space. For different structures different models are known. In this thesis the structure factor of disordered charged spherical particles and the structure factor of crystalline hematite were measured. Therefore, models for these structures are presented in the following two sections.

2.3.1 Structure factor of charged spheres

To model the radial pair distribution function $g(|\vec{r}|)$ from the particle pair interaction potential $V_{\mathrm{pot}}(\vec{r})$ is a common approach. Here, a disordered sample system of charged spheres with radius R_0 and density n dispersed in an electrolyte suspension is considered. For this system the so-called total correlation function $h(\vec{r})_{h,j}$ between two particles h and j can be written as a sum of the direct particle correlation $c(\vec{r})_{h,j}$ of the two particles and the indirect correlations $c(|\vec{r} - \vec{r}'|)_{h,j}$ involving other particles. With these functions the Ornstein-Zernike equation can be written as[16]

$$h(\vec{r}) = c(\vec{r}) + n \int c\left(|\vec{r} - \vec{r}'|\right) h(\vec{r}') d^3 r. \tag{2.32}$$

The total correlation function is related to the pair distribution function by $h(\vec{r}) = g(\vec{r}) - 1$. This equation can be solved iteratively by using the mean spherical approximation (MSA) for electrolyte suspensions at moderate high particle concentrations.[17] The closure-relation of

[16]Ornstein, L.S. et al. *KNAW Proceedings* **17**, (1914), 793.
[17]Lebowitz, J.L. et al. *Phys. Rev.* **144**, (1966), 251; Percus, J. K. et al. *Phys. Rev.* **136**, (1964), 290.

the MSA model is given by

$$h(\vec{r})_{h,j} = -1 \qquad |\vec{r}| < (R_h + R_j),\tag{2.33}$$

and

$$c(\vec{r})_{h,j} = -\frac{V(\vec{r})}{k_B \cdot T} \qquad |\vec{r}| > (R_h + R_j),\tag{2.34}$$

where T is the temperature, k_B the Boltzmann constant, and $V_{pot}(\vec{r})$ the electrostatic potential. Typically a screened Yukawa potential is used

$$V_{Yu}(r) = \begin{cases} \infty & |\vec{r}| < (R_h + R_j) \\ \frac{e_0}{4\pi\epsilon}\left(Z_h \frac{e^{\varkappa \cdot R_h}}{1 + \varkappa \cdot R_h}\right)\left(Z_j \frac{e^{\varkappa \cdot R_j}}{1 + \varkappa \cdot R_j}\right)\frac{e^{-\varkappa \cdot r}}{\varkappa \cdot r} & |\vec{r}| > (R_h + R_j) \end{cases}\tag{2.35}$$

where e_0 is the elementary charge, $\varkappa$ is the Debye-Hückel constant, and ϵ is the permittivity of the electrolyte. The inverse of the Debye-Hückel constant $\varkappa$ describes the exponential decay of the potential as distance from the particle.[18] The length $\varkappa^{-1}$ is called Debye length. The Debye-Hückel constant is given by

$$\varkappa^2 = \frac{e_0^2}{\epsilon\epsilon_0 k_B T} \frac{2c_s + \frac{3|\Psi|\phi}{R_0 e_o}}{1 - \phi},\tag{2.36}$$

where e_0 is the elementary charge, ϵ_0 is the vacuum permittivity, c_s is the salt concentration, ϕ is the volume fraction of the particles, and Ψ is the surface charge of the particle. It is given by

$$\Psi = \frac{z_p}{4\pi R_0^2},\tag{2.37}$$

where z_p is the particle charge. This model was extended to arbitrary low particle densities by using the rescaled mean spherical approximation (RMSA).[19] With these assumptions and using equation 2.32 the pair distribution function $g(r)$ can be extracted. A model for the calculation of the structure factor with the RMSA model was published by Ruiz-Estrada.[20] This model was used to describe the structure factor of charge spheres in this thesis. It allows to model the structure factor with respect to the particle radius R_0, the volume fraction ϕ, the charge of the particles z_p, the temperature T, the dielectric permittivity ϵ, and a concentration of a screening material. Because the screening of the potential is typically described by the present

---

[18]Larson, R.G. *The Structure and Rheology of Complex Fluids*. New York: Oxford University Press, 1999.
[19]Hansen, J.P. et al. *Mol. Phys.* **46**, (1982), 651.
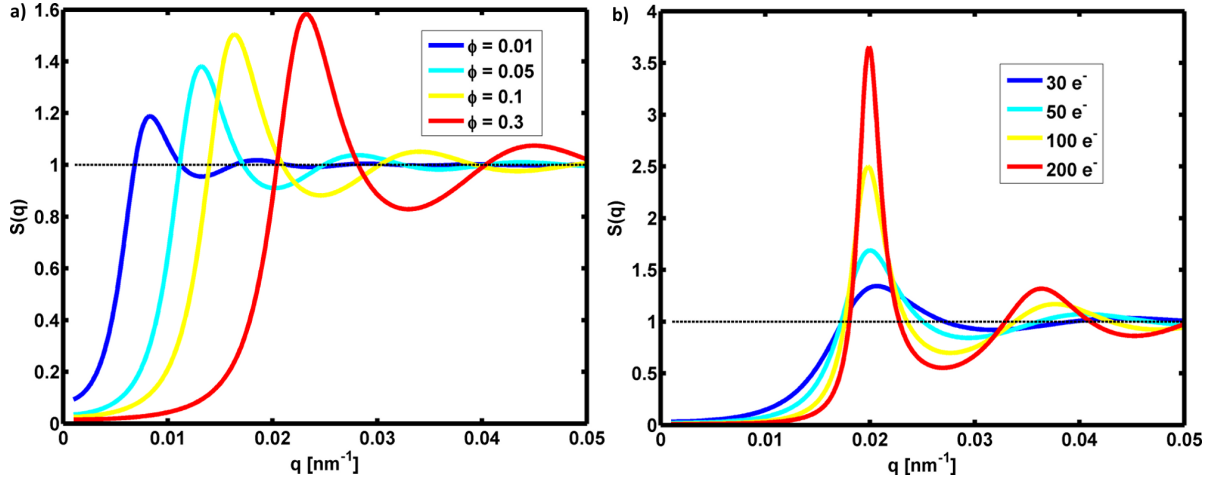[20]Ruiz-Estrada, H. *Physica A* **168**, (1990), 919.

Figure 2.17: (a) Calculation of the structure factor $S(q)$ within the RMSA model for different particle concentrations. (b) Calculation of the RMSA $S(q)$ for different particle charges. The results are calculated using $R_0 = 125\,\mathrm{nm}$, $T = 300\,\mathrm{K}$, $\epsilon_r = 80$, $c_s = 100\,\mu\mathrm{Mol}$.

of salt the screening parameter can be interpreted as salt concentration in the dispersion. In figure 2.17 the influence of the volume fraction and particle charge on the structure factor obtained with the RMSA model is illustrated. The position of the first maximum of the structure factor is a function of the volume fraction of the particles in the dispersion while the height is mainly a function of the particle charge.

2.3.2 Structure factor of crystals

In this section a short introduction to the structure factor from crystalline structures is presented. A comprehensive overview can be found in literature.[21] The defining property of a solid crystal is the periodicity of the particles. The structure of scattering centers leads to symmetries that generate constructive and deconstructive interferences of scattered photons. The periodic structure is typically described by unit cells which is the unit element of the structure. The periodic structure can show different symmetries such as cubic, trigonal, or hexagonal. These symmetries are also present in the unit cell. The structure factor of a crystal can be expressed with two different terms

$$S_{\mathrm{crystal}}(\vec{q}) = \sum_h f_h(\vec{q}) e^{i\vec{q}\vec{r}_h} \sum_{\vec{R}_n} e^{i\vec{q}\vec{R}_n}, \tag{2.38}$$

---

[21] Warren, B.E. *X-Ray diffraction.* Addison-Wesley, 1969; Als-Nielsen, J. *Elements of Modern X-Ray Physics.* Wiley and Sons, Ltd, 2001.

where $\vec{R}_n$ is the so called lattice vector. It is directed to the origin of the unit cell and $\vec{r}_h$ is the position of a particle h with respect to the origin of the unit cell. The first term in equation 2.38 describes the contribution from one unit cell to the structure factor. The second term is the so called lattice sum and describes the interferences of scattered photons from different unit cells. The second term differs from 1 only for

$$\vec{q} \cdot \vec{R}_n = 2\pi \cdot n, \tag{2.39}$$

where n is an integer. In this case the lattice sum contributes to the structure factor. The lattice vector is in general given by

$$\vec{R}_n = n_1 \vec{a}_1 + n_2 \vec{a}_2 + n_3 \vec{a}_3, \tag{2.40}$$

where $\vec{a}_1$, $\vec{a}_2$ and $\vec{a}_3$ are the basis vectors of the lattice coordinates and n_1, n_2 and n_3 are integers. Corresponding to this a so-called reciprocal lattice vector can be defined as[22]

$$\vec{G} = h\vec{a}_1^* + k\vec{a}_2^* + l\vec{a}_3^*, \tag{2.41}$$

where h, k and l are integers such that the product of the lattice vectors $\vec{G}$ and $\vec{R}_n$ is then

$$\vec{G} \cdot \vec{R}_n = 2\pi (hn_1 + kn_2 + ln_3) = 2\pi \cdot n. \tag{2.42}$$

This is the solution of equation 2.39. Thus the structure factor $S_{\text{crystal}}(q)$ is non-vanishing when the reciprocal lattice vector coincides with the lattice vector, $\vec{q} = \vec{G}$. This is the Laue condition for the observation of diffraction from a crystalline lattice. The integers (h, k, l) are known as Miller indices. For constructive interference of scattered photons they describe a lattice vector $\vec{G}$ in reciprocal space which belongs to the scattering plane in the crystal. With this information Bragg's law for constructive interference can be expressed by

$$n \cdot \lambda = 2d \sin(\theta), \tag{2.43}$$

where λ is the wavelength, d the lattice constant, and θ the scattering angle. The integer n describes the interference maximum. In this thesis the trigonal structure of hematite was measured. This structure has a lattice constant of $a = 5.038\,\text{Å}$ and $b = 13.772\,\text{Å}$ at the space group R$\bar{3}$c.[23] One example of a calculated structure factor of this structure is depicted in

---

[22] Als-Nielsen, J. *Elements of Modern X-Ray Physics*. Wiley and Sons, Ltd, 2001.
[23] Blake, R.L. et al. *Am. Mineral* **51**, (1966), 123; Pauling, L. et al. *J. Am. Chem. Soc.* **47**, (1925), 781.
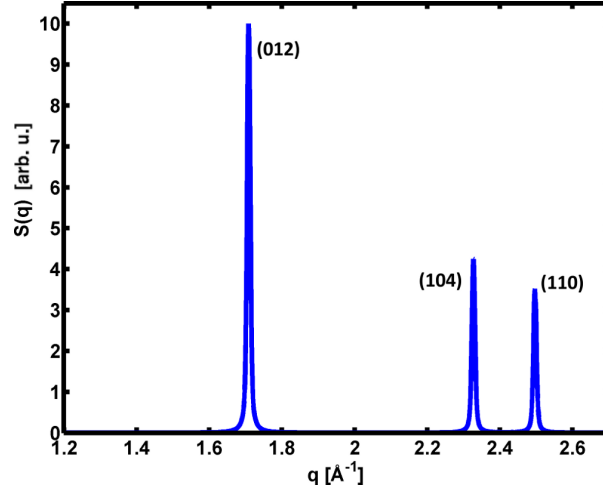
Figure 2.18: Calculated structure factor of a crystalline sample of hematite.

figure 2.18.[24] The interference maxima are labled according to their Miller indices h, k, l.

2.4 Coherence

Coherence describes the property of waves to interfere. It is the correlation between waves in an electromagnetic field. An electromagnetic wave $\vec{E}(\vec{r}, t)$ is a function of time t and the three dimensional real space $\vec{r}$. The first order correlation function for this field is the so-called mutual coherence function (MCF)[25]

$$\Gamma(\vec{r}_1, \vec{r}_2, \Delta t) = \left\langle E(\vec{r}_1, t) E^*(\vec{r}_2, t + \Delta t) \right\rangle, \tag{2.44}$$

where the brackets denotes the ensemble average of all possible realizations of the field and Δt is a time delay. The degree of coherence is given by the normalized MCF

$$\gamma(\vec{r}_1, \vec{r}_2, \Delta t) = \frac{\left\langle E(\vec{r}_1, t) E^*(\vec{r}_2, t + \Delta t) \right\rangle}{\sqrt{\left\langle I(\vec{r}_1, t) \cdot \left\langle I(\vec{r}_2, t) \right\rangle \right\rangle}}, \tag{2.45}$$

where $I(\vec{r}, t)$ stands for the intensity at location $\vec{r}$ and time t. Coherence can be divided into two kinds, the transverse coherence, which is also known as spatial coherence, and the longitudinal coherence or temporal coherence.

---

[24]The calculation were carried out with the scientific program Poudrix. (http://www.inpg.fr/lmgp)
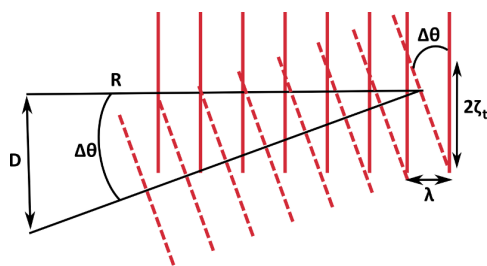[25]Nugent, K.A. *Adv. Phys.* **59**, (2010), 1.

Figure 2.19: Sketch to illustrate the definition of the transverse coherence length ζ_t. Propagation of two waves (solid line, dashed line) in different directions originating from two different sources separated by distance D.

- **Spatial coherence**

  The spatial coherence length ξ_t is defined to be the distance along a wavefront over which two waves of the same wavelength, which originate from two different points in direct space, are completely out of phase, see figure 2.19. From this geometrical consideration it is possible to extract $\frac{\lambda}{2\xi_t} = \tan(\Delta\theta)$ and $\frac{D}{R} = \tan(\Delta\theta)$. Thus, the transverse coherence length can be written as[26]

  $$\xi_t = \frac{\lambda R}{2D}. \tag{2.46}$$

- **Temporal coherence**

  The temporal coherence length describes the wavelength spread based on the fact that an electromagnetic field is never fully monochromatic. The longitudinal coherence length ξ_l is defined to be the distance over which two waves from the same source point with different wavelengths will completely be out of phase, see figure 2.20. To propagate the longitudinal coherence length the first wave needs N oscillations and the second wave needs $N+1$ oscillations. Therefore, the longitudinal coherence length is described by $N\lambda = (N+1)(\lambda + \Delta\lambda)$. With $2\xi_l = N\lambda$ it can be written as[27]

  $$\xi_l = \frac{\lambda^2}{2\Delta\lambda}, \tag{2.47}$$

  where λ is the wavelength and $\Delta\lambda$ is the wavelength or energy spread.

---

[26] Als-Nielsen, J. *Elements of Modern X-Ray Physics*. Wiley and Sons, Ltd, 2001.
[27] Veen, F. Van der et al. *J. Phys.: Condens Matter* **16**, (2004), 5003; Als-Nielsen, J. *Elements of Modern X-Ray Physics*. Wiley and Sons, Ltd, 2001.
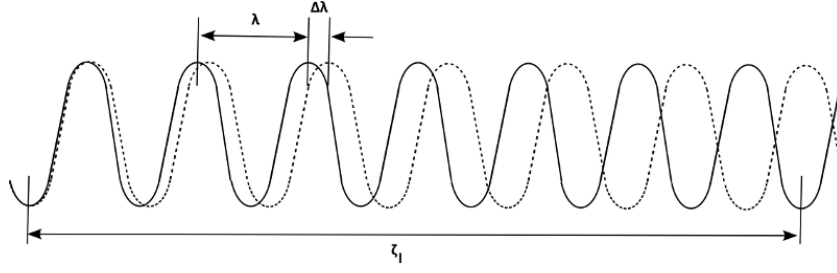
Figure 2.20: Sketch of two waves with wavelength λ and $\lambda + \Delta\lambda$ to illustrate the definition of the longitudinal coherence length ξ_l.
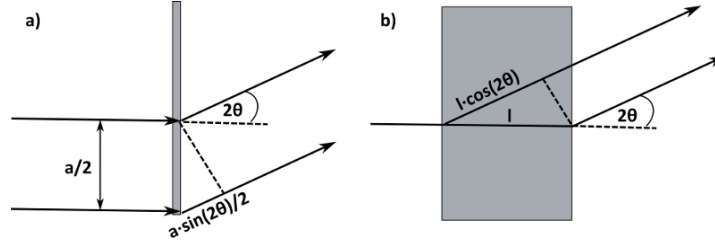

Figure 2.21: Two different scattering geometry. a) Scattering along the width of the sample. b) Scattering along the thickness of the sample.

Interference of x-ray waves in a scattering experiment occurs if the path length difference (PLD) of the scattered x-ray waves within the sample is of the order of the coherence lengths.[28] The impact of the coherence lengths on a coherent scattering event from a sample with width a and thickness l depends on the scattering geometries, see figure 2.21. The PLD between two scattered waves along the width of the sample equals $PLD = a \cdot \sin(2\theta)/2$, where 2θ is the scattering angle. The restriction for full illumination of coherent light is $PLD < \xi$.[29] Thus one condition for coherent scattering is given by

$$\xi_t > a \cdot \sin(2\theta)/2. \qquad (2.48)$$

The contribution of the sample thickness on the PLD is shown in figure 2.21 (b). Here, the path length difference equals $PLD = l - l\cos(2\theta) = 2l\sin^2(\theta)$. The condition for coherent scattering in this geometry is given by

$$\xi_l > 2l \cdot \sin^2(\theta). \qquad (2.49)$$

When a sample is illuminated by coherent x-ray waves speckle pattern can occur in scattering

---

[28] Goodman, J.W. *Statistical Optics*. New York, USA: John Wiley and Sons. Inc., 2000; Nugent, K.A. *Adv. Phys.* **59**, (2010), 1.

[29] Veen, F. Van der et al. *J. Phys.: Condens Matter* **16**, (2004), 5003.

experiments.[30] In general, a speckle pattern is produced whenever randomly distributed regions of scattering centers introduce different phase shifts into the scattering signal.[31] The size of a speckle S_p is given by

$$S_p = \frac{\lambda d}{b}, \tag{2.50}$$

where d is the sample-detector distance and b the beam size. The contrast of a speckle pattern equals the coherence degree at $\vec{R} = \vec{r}_1 - \vec{r}_2 = 0$ and $\Delta t = 0$. It is given by[32]

$$\beta = \left| \gamma(\vec{R} = 0, \Delta t = 0) \right| = \frac{\sqrt{\langle I^2 \rangle - \langle I \rangle^2}}{\langle I \rangle} = \frac{1}{\sqrt{M}}, \tag{2.51}$$

where the brackets $\langle . \rangle$ denote an average, and M is the mode number. In case of full coherence the contrast β equals 1 and the mode number is $M = 1$. It can be shown that the contrast is connected to the coherence lengths and the geometry of the sample by $\beta = \beta_z \beta_r$ with

$$\beta_z = \frac{\xi_t^2}{a^2} \left[\frac{a}{\xi_t} \sqrt{\pi} \cdot \text{erf}\left(\frac{a}{\xi_t} \right) + \exp\left(\frac{-a^2}{\xi_t^2} \right) - 1 \right], \tag{2.52}$$

and

$$\beta_r = \frac{1}{(lb)^2} \int_0^b dx (b-x) \int_0^l dy (l-y) \exp\left(\frac{-x^2}{\xi_t^2} \right)$$
$$\left[\exp(-2 |(A + B \tan(-\theta))x + By|) + \exp(-2 |(A + B \tan(\gamma))x \pm By|) \right], \tag{2.53}$$

where erf is the error function, θ is half of the scattering angle 2θ, and the coefficient $A = \frac{\Delta \lambda}{\lambda} q \sqrt{1 - \frac{q^2}{4k^2}}$, $B = -\frac{\Delta \lambda}{2\lambda} \frac{q^2}{k_0}$ with $k = \frac{2\pi}{\lambda}$. In figure 2.22 a) the contrast β as function of the momentum transfer q calculated for different sample thicknesses l is shown. The contrast decreases with increasing wave vector transfer. For an x-ray scattering experiment at large scattering angles (large $\vec{q}$) the contrast is smaller compared to an experiment at small scattering angles (small $\vec{q}$). Furthermore, the contrast decreases with increasing sample thickness. Therefore, a thin sample is required in coherent x-ray scattering experiments at large scattering angles to resolve speckles. In figure 2.22 b) the speckle contrast at $q = 3\,\text{Å}^{-1}$ as function of

[30]Sutton, M. et al. *Nature* **352**, (1991), 608; Sinha, S.K. et al. *Phys. Rev. B* **57**, (1998), 2740; Lengeler, B. *Naturwissenschaften* **88**, (2001), 249.

[31]Goodman, J.W. *Speckle Phenomena in Optics*. Greenwood Village, USA: Roberts and Company Publishers, 2007; Goodman, J.W. *J. Opt. Soc. Am.* **66**, (1976), 1145.

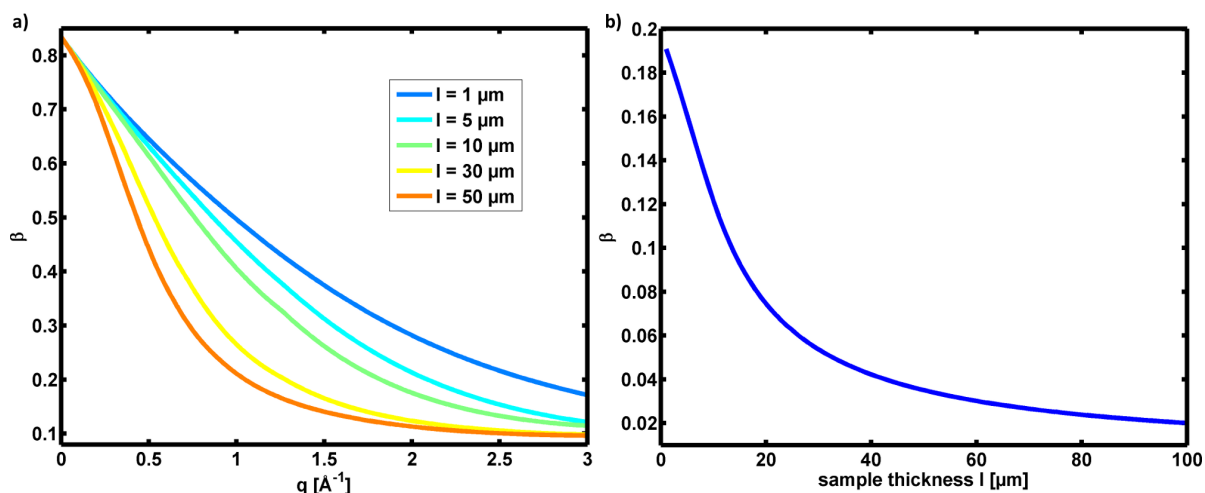[32]Gutt, C. et al. *Phys. Rev. Lett.* **108**, (2012), 024801; Sutton, M. *Evaluation of coherence factor for high Q data*. 2014. URL: http://www.physics.mcgill.ca/~mark/coherence/yorick/highqbeta.pdf.

Figure 2.22: Results of a calculation of the contrast of speckle pattern. The following values were used for the calculation: $a = 10\,\mu m$, $b = 5\,\mu m$, $\lambda = 1.65$ Å, $\frac{\lambda}{\Delta\lambda} = 3.5\cdot 10^{-5}$ and $\xi_t = 10\,\mu m$. a) Contrast β as function of the momentum transfer q at different sample thicknesses. b) Contrast β as function of the sample thickness l at $q = 3\,\text{Å}^{-1}$

the sample thickness l is shown. From this example one can see that the sample thickness should be in the order of the longitudinal coherence length $l \approx \xi_l$ for coherent scattering experiments at large wave vector transfer $\vec{q}$.

Different analysis methods for speckle patterns have been developed to extract dynamical[33] and structural[34] information of the sample (XPCS, XCCA, CDI). In this work one goal is to attempt measurements of speckles at large wave vector transfer $\vec{q}$ from molecular liquids for enabling such analysis methods. Thus, a thin sample system is required. In the next chapter different injection systems to form a thin liquid sample are presented and discussed.

---

[33]Grübel, G. et al. *Nuc. Instr. Meth. Phys. Res. B* **262**, (2007), 357; Grübel, G. et al. *J. Alloys Comp.* **362**, (2004), 3; Grübel, G. et al. *Soft-Matter Characterization*. New York, USA: Springer Science+Buisness Media, LLC, 2008. Chap. X-Ray Photon Correlation Spectroscopy (XPCS).
[34]Wochner, P. et al. *PNAS* **106**, (2009), 11511; Wochner, P. et al. *Int. J. Mat Res.* **106**, (2011), 874; Pedrini, B. et al. *Nature Com.* **4**, (2013), 1647; D., Starodub et al. *Nature Com.* **3**, (2012), 1276; Saldin, D.K. et al. *New Journal of Physics* **12**, (2010), 035014; Saldin, D.K. et al. *Acta Cryst.* **A66**, (2010), 32; Saldin, D.K. et al. *Phys. Rev. Lett.* **106**, (2011), 115501; Saldin, D.K. et al. *Optics Express* **19**, (2011), 17318; Saldin, D.K. et al. *New Journal of Physics* **12**, (2010), 035014.

3 Sample injection systems

In modern x-ray scattering experiments on liquids, different sample containers have been used during the past years. In contrast to conventional experiments on liquid samples in capillaries an injection system offers the possibility to measure a liquid sample without the influence from a sample chamber or a capillary. Controlling the properties of an injection technique is important for x-ray scattering experiments. To this end different methods have been developed to solve this problem.

In this chapter different injection systems for generating liquid samples of μm size and their corresponding properties are presented. An overview of sample injection techniques is given in section 3.1. The physics of liquid jets, e.g. stability, geometry, and thermodynamics are discussed in section 3.2.

3.1 Injection techniques

In this section the conventionally used injection techniques are presented and discussed together with their application in x-ray scattering experiments on fluids with special emphasis to molecular liquids. A short overview is given in the following list:

- **Liquid film tunnel**
  A liquid film tunnel generates a thin liquid film between two wires.[1] The width of the liquid film can be regulated by expanding the separation between the two wires. A typical film tunnel setup is depicted in figure 3.1. The film thickness f_t is limited by the surface tension of the liquid.[2] High surface tensions result in instabilities. Therefore, sodium dodecyl sulfate (SDS) is often added to the liquid to reduce the surface tension. In this way it is possible to generate liquid water film of a thickness of $f_t \approx 5\,\mu m$.[3]

- **Rayleigh nozzle**
  A Rayleigh nozzle produces a free standing liquid jet that breaks up into droplets

[1]Gharib, M. et al. *Bull. Am. Phys. Soc.* **36**, (1991), 2718.
[2]Couder, Y. et al. *Physica D* **37**, (1989), 384.
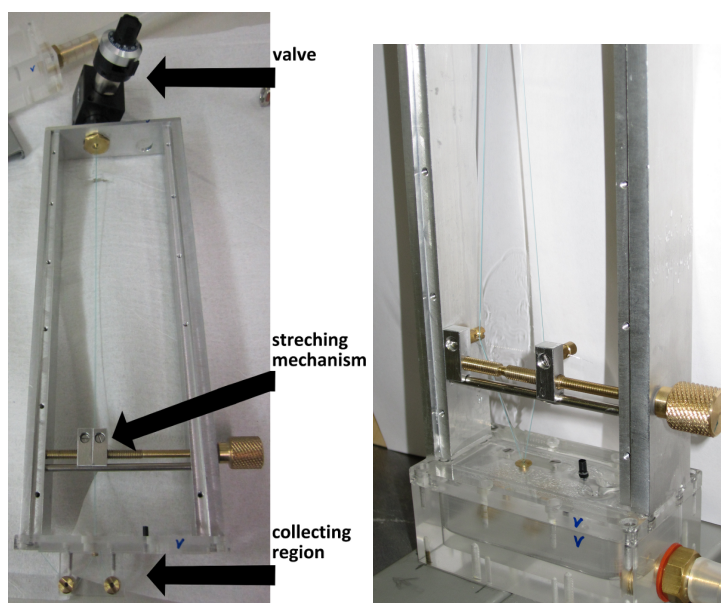[3]Beizaie, M. et al. *Exp. Fluid* **23**, (1997), 130.

Figure 3.1: Two photographs of a film tunnel setup. Left: Overview of the whole film tunnel setup. The flow of the film is directed from the valve to the collecting region by passing the stretching mechanism. Right: Liquid film between two wires.

Figure 3.2: Scheme of a Rayleigh nozzle.

after a break-up length L. The formation of liquid jets and the understanding of their properties dates back to Rayleigh in 1878.[4] Thus, this nozzle design are named after Rayleigh and the break-up process of the jet is called Rayleigh break-up. A sketch of a Rayleigh nozzle is shown in figure 3.2. The liquid is compressed in a reservoir with pressure p_l. Thus, it flows through an exit orifice of the nozzle. The minimum pressure that is necessary to form a jet depends on fluid parameters such as viscosity, surface tension and density. Faubel et al.[5] investigated Rayleigh nozzles with laminar flowing liquid water jets with jet diameters on the micrometer scale. They reported on stable liquid jets with diameters down to $d_{jet} = 5\,\mu m$. The formation of such thin liquid jets

[4]Rayleigh, L. *Proc. Lond. Math. Soc.* **S1-10**, (1878), 4–13.
[5]Faubel, M. et al. *Z. Phys. D* **10**, (1988), 269; Faubel, M. et al. *J. Chem. Phys.* **106**, (1997), 9013; Faubel, M. et al. *J. Electron Spectrosc. Relat. Phenom.* **95**, (1998), 159.
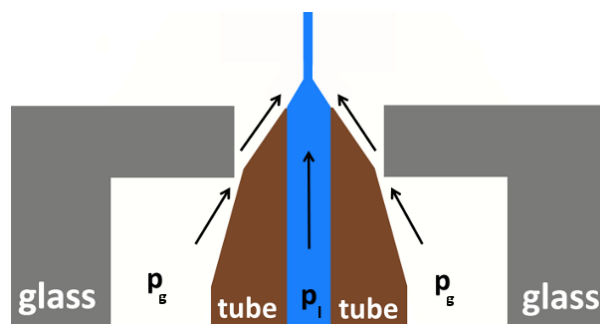
Figure 3.3: Schematic cut along a gas dynamic virtual nozzle (GDVN). The liquid pressure p_l and the gas pressure p_g are pointed out. Furthermore, the arrows denote to the flow direction.

needs liquid pressures up to $p_l = 100\,\mathrm{bar}$. This results in liquid flow rates Q of around a few hundred $\frac{\mathrm{ml}}{\mathrm{h}}$ and high flow velocities v_{jet} in the order of $50\,\frac{\mathrm{m}}{\mathrm{s}}$ to $100\,\frac{\mathrm{m}}{\mathrm{s}}$.

- **Gas dynamic virtual nozzle**

  The concept of a gas dynamic virtual nozzle (GDVN) is basically a modification of the Rayleigh nozzle and dates back to Gañán-Calvo et al.[6] They developed the gas-focusing technique, which works with a gas stream surrounding the liquid jet. This technique allows to produce liquid jets of diameters down to the µm regime with break-up lengths L of a few hundred µm.[7] The jet breaks into a train of droplets similar to a jet produced by a Rayleigh nozzle. Deponte et al.[8] combined the advantages of the flow focusing technique with a nozzle suitable for x-ray scattering experiments (GDVN). This nozzle mainly consists of a micro tube in a glass plenum, see figure 3.3. The liquid is flowing through the tube and the gas is guided by the glass plenum. At the tip of the nozzle the gas presses the liquid to a thin jet. The flow rates of jets formed by these nozzles are typically in the range of $Q = 1\,\frac{\mathrm{\mu l}}{\mathrm{min}}$ to $Q = 50\,\frac{\mathrm{\mu l}}{\mathrm{min}}$, which is much lower compared to the Rayleigh nozzle. Such a small material flow allows to work in moderate vacuum ($p_{vac} = 10^{-3}\,\mathrm{mbar}$). The flow velocity v_{jet} ranges from $1\,\frac{\mathrm{m}}{\mathrm{s}}$ to $50\,\frac{\mathrm{m}}{\mathrm{s}}$.

- **Electrospinning**

  Electrospinning is a technique to produce a liquid jet guided by electric fields.[9] An electrostatic fiber with diameters ranging from $10\,\mathrm{\mu m}$ to $10\,\mathrm{nm}$ accelerates the liquid. By this means a thin liquid jet is generated. For this technique the liquid has to be charged to interact with the electric fields. If this is not the case, the liquid can be made

[6]Gañán-Calvo, A.M. *Phys. Rev. Lett.* **80**, (1998), 285.
[7]Deponte, D.P. et al. *Micron* **40**, (2009), 507; Deponte, D.P. et al. *Microsc. Microanal.* **14**, (2009), suppl 2.
[8]Deponte, D.P. et al. *J. Phys. D: Appl. Phys.* **41**, (2008), 195505.
[9]Fridrikh, S.V. et al. *Phys. Rev. Lett.* **90**, (2003), 144502.

Figure 3.4: Microscope image of a supersonic microjet with $v_{jet} = 490\,\frac{m}{s}$. The edge of the capillary is at the right side and the jet is visible at the left side. The laser illuminates the liquid in the capillary. It is not visible in this figure. Image is adapted from: Tagawa, Y. et al. *Phys. Rev. X* **2**, (2012), 031002.

charged by adding charged substances.[10] The jets generated with this technique offer to work with small flow rates down to a few $\frac{nl}{min}$.[11] The geometrical properties of the jets are comparable with the properties resulting from the GDVN.

- **Supersonic microjets**

  Supersonic liquid microjets are produced by an instantaneous expansion of a small fraction of the liquid located in a capillary.[12] This is done by a laser beam that heats up the liquid, which afterwards evaporates and expands. The remaining liquid in the capillary gets accelerated up to $v_{jet} = 850\,\frac{m}{s}$.[13] The smallest reported diameter of such a liquid jet is $d_{jet} = 10\,\mu m$ for a jet length of $L = 500\,\mu m$, see figure 3.4.[14] The lifetime of such jets is in the order of a few ms.

- **Gas-phase injector**

  The gas-phase injector works with the use of aerodynamic lenses to form a gaseous suspension of wet particles, see figure 3.5.[15] Hence, it offers the possibility to study suspended particles in a gaseous atmosphere and not in a solvent. In this device particles are injected by a nebulizer and focused to a colliminated particle beam. The aerodynamic lenses are basically apertures that the particles in a gaseous atmosphere are passing by. In a gas-phase injector several of such apertures are mounted in a row, see figure 3.5. The diameter of the apertures decreases from the first lens to the last one. While passing this stack of lenses the solvent evaporates in the vacuum and the particles are dispersed in the resulting gaseous atmosphere.[16] This technique can be used for particles

---

[10]Sierra, R.G. et al. *Acta Cryst. D* **68**, (2012), 1584.

[11]Gañán-Calvo, A.M. et al. *New J. Phys.* **15**, (2013), 033035.

[12]Aniskin, V.M. et al. *Tech. Phys. Lett.* **37**, (2011), 1046; Aniskin, V. et al. *Microfluid Nanofluid* **14**, (2013), 605; Phalnikar, K.A. et al. *Exp. Fluids* **44**, (2008), 819.

[13]Scroggs, S.D. et al. *Exp. Fluids* **21**, (1996), 401.

[14]Tagawa, Y. et al. *Phys. Rev. X* **2**, (2012), 031002.

[15]Wang, X. et al. *Aerosol Sci. Technol.* **39**, (2005), 611; Murphy, W.K. et al. *J. Appl. Phys.* **35**, (1964), 1986.

[16]Spence, J.C.H. et al. *Rep. Prog. Phys.* **75**, (2012), 102601.
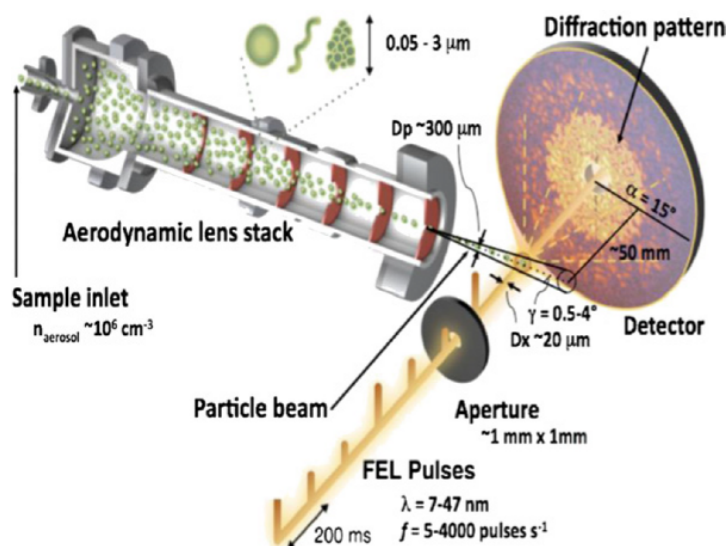
Figure 3.5: Sketch of a diffraction experiment with an gas-phase injector. Bogan, M.J. et al. *J. Phys. B: Mol. Opt. Phys.* **43**, (2010), 194013.

of diameters from 0.05 μm up to 10 μm.[17] The particle velocity in the focused beam can reach velocities of up to $v = 150 \frac{m}{s}$.[18] In contrast to liquid jets the particle beam allows measurements of dispersed particles in a gaseous atmosphere instead of a liquid solvent.

X-ray scattering experiments on liquids require certain conditions. Thus, some techniques are not adequate for such experiments and can therefore be excluded. Four different requirements can be pointed out so far:

1. **Pure sample**
   For experiments on complex liquids it is necessary that the sample system is not affected by additives.

2. **Sample geometry**
   For measurements of speckle pattern the liquid sample needs to be thin as possible, see section 2.4.

3. **Stability**
   X-ray scattering experiments can last several hours or days. Therefore, a stable liquid sample for this time period is necessary.

---

[17]Wang, X. et al. *Aerosol Sci. Technol.* **39**, (2005), 611.
[18]Bogan, M.J. et al. *J. Phys. B: Mol. Opt. Phys.* **43**, (2010), 194013.

4. **Vacuum**

   The material flow into the vacuum has to be minimized to affect the vacuum condition as little as possible. In this way, background scattering can be reduced.

The gas dynamic virtual nozzle (GDVN) is the only technique that fulfills all requirements mentioned above. It provides a stable liquid jet in vacuum with a weak flow rate. Furthermore, no additives influence the liquid sample. These advantages of the GDVN technique are the reason why it is used in many scattering experiments performed recently at modern FEL sources.[19] The work with a liquid jet environment and the GDVN technique requires a vacuum chamber with different diagnostic methods to control the liquid jet and to align it to the x-ray beam. Therefore, the development of a liquid jet environment with a GDVN and the needed diagnostics for experiments on liquids to enable the research of complex fluids such as colloidal dispersions and molecular liquids with x-ray scattering is one goal of this work. For this purpose, first experiments with Rayleigh nozzles were performed. This technique can operate in atmosphere and does not need a vacuum chamber. Hence, in the framework of this thesis the GDVN and the Rayleigh nozzle are used to form liquid jets. In the following section the physics of liquid jets are discussed.

3.2 Physics of liquid jets

For the description of the liquid jets a general liquid jet geometry is considered. It is illustrated in figure 3.6. The liquid jet is injected by a nozzle into a volume. This volume can be evacuated or containing gas. The break-up length L is the length of a continuous liquid jet until it breaks into droplets. These droplets are formed at an interaction length Λ where the jet diameter decreases. An undisturbed liquid jet is formed if $L > \Lambda$. If this is not the case ($L < \Lambda$) a liquid jet cannot be formed and only droplets exit the nozzle. Thus, to form a liquid jet the interaction length Λ has to be minimized or the break-up length L has to be maximized.

The break-up length L and the interaction length Λ depend on the flow stability of the liquid jet. For the description of stable and laminar flows dimensionless flow parameters are often used. Therefore, two dimensionless flow parameters can be introduced. The Reynolds

---

[19]Koopmann, R. et al. *Nature Methods* **9**, (2012), 259; Johansson, L.C. et al. *Nature Methods* **9**, (2012), 263; Boutet, S. et al. *Science* **337**, (2012), 362; Aquila, A. et al. *Opt. Exp.* **20**, (2012), 2706; Lomb, L. et al. *Phys. Rev. B* **84**, (2011), 214111; Chapman, H.N. et al. *Nature* **470**, (2011), 73.
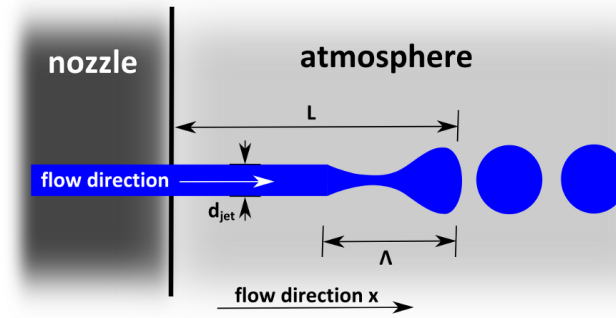
Figure 3.6: Sketch of a liquid jet that is injected from a nozzle to an atmosphere. Depicted are the jet diameter d_{jet}, break-up length L, interaction length Λ, and the flow direction.

number Re, which is named after Osborne Reynolds. It is given by[20]

$$Re = \frac{\rho_l \cdot v \cdot d}{\eta},\tag{3.1}$$

where ρ_l denotes the liquid density, v the flow velocity, η is the viscosity and d a characteristic length scale of the flowing system. For a liquid jet system d is equivalent to the jet diameter d_{jet}. In this way the Reynolds number characterize the flow behavior of a liquid jet. Below a critical value Re_{crit} the flow is laminar, above this value the flow can tumble into turbulence.[21] For example, for a cylindrical flow of water the critical value is $Re_{\text{crit}} = 2040$.[22] In general, a high Reynolds number is a sign for a turbulent flow and thus for an unstable liquid jet. A dimensionless flow parameter which can be used to describe the liquid jet break-up is the Weber number.[23] It is given by

$$We = \frac{\rho_l \cdot v^2 \cdot d}{\sigma},\tag{3.2}$$

where σ is the surface tension. The Weber number describes the ratio between the kinetic forces and surface forces. When the surface forces dominate the jet breaks into droplets. Thus a high Weber number describes a stable jet while a low We describes an unstable jet.[24] The break-up mechanism and the instability of liquid jets can be described with respect to these dimensionless flow parameters. Furthermore, the break-up length L, the jet diameter

---

[20]Reynolds, O. *Phil. Trans. R. Soc. Lond.* **174**, (1883), 935.

[21]Avila, M. et al. *J. Fluid Mech.* **646**, (2010), 127; Hof, B. et al. *Nature* **443**, (2006), 59; Wygnanski, I. et al. *J. Fluid Mech.* **69**, (1975), 283.

[22]Tropea, C. et al. *Hanbook of Experimental Fluid Mechanics; Band1.* Springer-Verlag Berlin Heidelberg, 2007.

[23]Reitz, R.D. et al. *The Encyclopedia of Fluid Mechanics, Chapter 10: Mechanisms of Breakup of Round Liquid Jets.* Gulf, Housten, 1986.

[24]Weber, C. *Z. Angw. Math. Mech.* **2**, (1931), 136.

d_{jet}, and the interaction length Λ are discussed. At the end of this section the thermodynamic properties of liquid jets are presented.

3.2.1 Instability

Free standing liquid jets are treated in general as instable because they spontaneously break up.[25] It is assumed that the onset of the break-up mechanism is caused by intrinsic instabilities in the jet. One possible approach to describe the break-up mechanism is to model capillary waves on the jet surface, which can be expressed by a wave packet[26]

$$\eta_{\mathrm{in}}(\omega, k) = A_0 \cdot e^{\omega t + ikx}, \tag{3.3}$$

where k is the complex wave vector, and ω is the complex wave frequency, x is the spatial coordinate along the axis of the jet, A_0 is the amplitude, and t the time. Because a liquid jet breaks up after a certain time and not instantaneously an amplification of the capillary wave is assumed. To consider this property, the wave vector is usually considered to be a complex number $k = k_r + ik_i$, where the real part k_r is the number of waves over the distance 2π and the imaginary part k_i describes the spatial growth rate of the instability.[27] In addition, the wave frequency is considered as a complex number $\omega = \omega_r + i\omega_i$. The real part describes the temporal growth rate of the flow instability and the imaginary part the frequency.[28] When the amplitude of one capillary wave $\eta_{\mathrm{in}}(\omega, k)$ equals the jet radius r_{jet} the jet breaks into droplets. This break-up mechanism of a liquid jet is called capillary pinching[29] and the jets are called capillary jets. To study the influence of flow parameters on the capillary waves the dispersion relation of a wave packet can be derived with the Navier-Stokes equations.[30] Momentum equation:

$$\rho_i \left(\frac{\partial}{\partial t} + v_i \cdot \nabla\right) v_i = -\nabla P_i, \tag{3.4}$$

Mass equation:

$$\frac{\partial}{\partial t}\rho_i + \nabla \cdot (\rho_i v_i) = 0, \tag{3.5}$$

---

[25]Lin, S.P. *Breakup of Liquid Sheets and Jets, Chapter 7: Inviscid Jets.* Cambridge University Press, 2003; Reitz, R.D. et al. *The Encyclopedia of Fluid Mechanics, Chapter 10: Mechanisms of Breakup of Round Liquid Jets.* Gulf, Housten, 1986.

[26]Lin, S.P. et al. *Annu. Rev. Fluid. Mech.* **30**, (1998), 85.

[27]Keller, J.B. et al. *Phys. Fluids* **16**, (1973), 2052; Lin, S.P. et al. *Annu. Rev. Fluid. Mech.* **30**, (1998), 85.

[28]Liu, Z. et al. *Int. J. Multiphase Flow* **23**, (1996), 631.

[29]It is also known as Rayleigh break-up.

[30]Tropea, C. et al. *Hanbook of Experimental Fluid Mechanics; Band1.* Springer-Verlag Berlin Heidelberg, 2007.

Energy equation:

$$(\frac{\partial}{\partial t} + v_i \cdot \nabla)e_i - P_i(\frac{\partial}{\partial t} + v_i \cdot \nabla)\frac{1}{\rho_i} = 0, \tag{3.6}$$

where ρ is the density, t the time, v is the velocity, $P(\rho, T)$ is the dynamic pressure, e is the internal energy, and T is the temperature. The subscripts denotes the fluid ($i = 1$) and the ambient atmosphere ($i = 2$). The dispersion relation of the capillary waves can be derived with a few assumptions: The space for the fluid is limited to $0 < r < r_{\text{jet}}$ and the space of the volume is limited to $r_{\text{jet}} < r < \infty$. The dynamical pressure of the fluid is constant and the pressure of the atmosphere is given by $P_2 = P_1 - \sigma / r_{\text{jet}}$, where σ stands for the surface tension. By solving the differential equations 3.4, 3.5, and 3.6 with these assumptions it can be shown that the relation between the wave frequency ω and the wave vector k is given by[31]

$$(k - \omega)^2 \frac{J_n(\lambda_1)}{\lambda_1} J_n'(\lambda_1) - Q(\frac{k v_{\text{gas}}}{v_{\text{jet}}} - \omega)^2 \frac{K_n(\lambda_2)}{K_n'(\lambda_2)\lambda_2} - We^{-1}k^2 = 0, \tag{3.7}$$

where the primes stands for the differential $\frac{d}{d\lambda_i}$[32] and J_n and K_n denote the Bessel function of first and second kind, respectively. The parameters λ_1 and λ_2 are given by

$$\lambda_1 = \sqrt{k^2 - M_1^2(k - \omega)^2}, \qquad \lambda_2 = \sqrt{k^2 - \left(\frac{v_{\text{jet}}}{v_{\text{gas}}}\right)^2 M_2^2 \left(\frac{k v_{\text{gas}}}{v_{\text{jet}}} - \omega\right)^2}, \tag{3.8}$$

with

$$Q = \frac{\rho_2}{\rho_1}, \qquad M_1 = \frac{v_{\text{jet}}}{c_1}, \qquad M_2 = \frac{v_{\text{gas}}}{c_2}, \tag{3.9}$$

and

$$v_1 = \begin{pmatrix} v_{\text{jet}} \\ 0 \\ 0 \end{pmatrix}, \qquad v_2 = \begin{pmatrix} v_{\text{gas}} \\ 0 \\ 0 \end{pmatrix}, \tag{3.10}$$

where v_{jet} and v_{gas} are the velocities in flow direction, c_1 and c_2 are the speed of sound in the fluid and atmosphere, respectively.[33]

With this dispersion relation a connection between the temporal growth rate ω_r as function of the wave number k_r can be derived, see figure 3.7 a).[34] The maximum ($\omega_{r,\text{max}} = \Omega$) of

[31]Lin, S.P. *Breakup of Liquid Sheets and Jets, Chapter 7: Inviscid Jets.* Cambridge University Press, 2003.

[32]For example: $J_n'(\lambda_1) = \frac{dJ(\lambda_1)}{d\lambda_1}$

[33]The parameters M_1 and M_2 are known as Mach number.

[34]Rayleigh, L. *Proc. Lond. Math. Soc.* **S1-10**, (1878), 4–13; Rayleigh, L. *Proc. R. Soc. Lond.* **29**, (1879), 71.

a)

b)
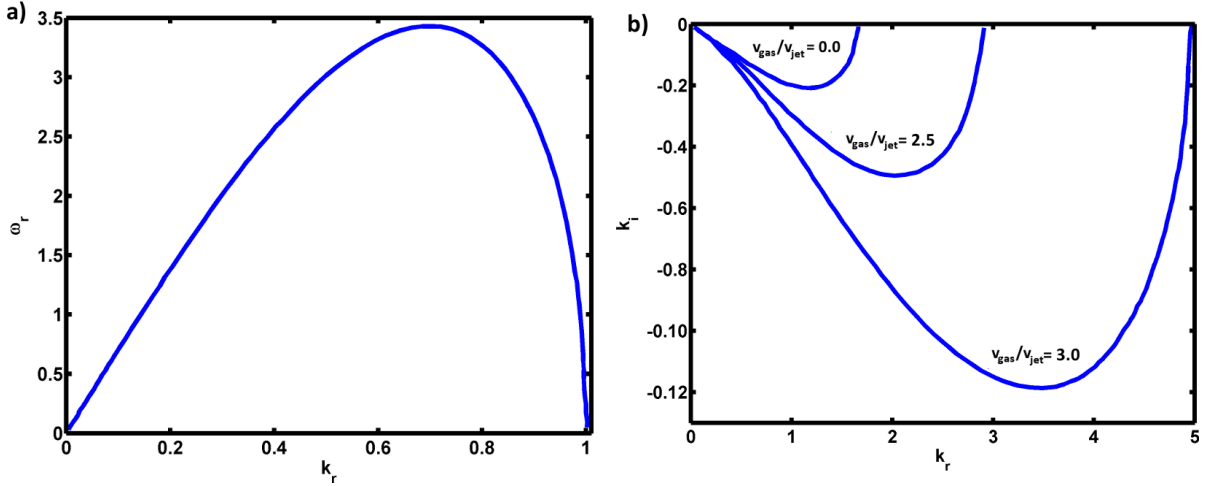
Figure 3.7: a) Temporal growth rate ω_r as function of the wave number k_r. b) Spatial growth rate k_i as function of the wave number k_r. Calculation were performed with $We = 1000$ and $Q = 0.0013$. Images Adapted from: Lin, S.P. *Breakup of Liquid Sheets and Jets, Chapter 7: Inviscid Jets.* Cambridge University Press, 2003.

the growth rate is at $k_r = 0.697$ which leads to a wavelength $\Lambda = \frac{2\pi}{k_r}$ as interaction length of the capillary wave on the jet, see figure 3.6. The cylindrical volume corresponding to Λ compared with the volume of a sphere leads to an estimation of the droplet size resulting from the break-up mechanism

$$r_{\text{droplet}} = 1.89 \cdot r_{\text{jet}}. \tag{3.11}$$

For the description of a GDVN the shear between the jet-gas interfaces has to be considered. The impact of shear on capillary waves on the jet surface was first analyzed by Helmholz and Kelvin at the end of the 19th century.[35] This so-called Helmholz-Kelvin instability was explained in terms of vorticity dynamics in the liquid.[36] The influence of a gas stream around a jet on the dispersion relation is shown in figure 3.7 b). When the gas velocity v_{gas} is faster than the liquid jet velocity v_{jet} the spatial growth rate k_i decreases and the wave number k_r increases. Thus, instabilities with larger wave number are amplified. Because of $k_r = \frac{2\pi}{\Lambda}$ this effect leads to a reduction of the interaction length Λ. Therefore, the size of the interaction region Λ and the size of the droplets decreases at increasing gas velocity v_{gas}. Furthermore, the decrease of the spatial growth rate k_i indicates an increase of the formation rate of droplets.[37] This impact of an gas stream on the amplification of the instabilities in a liquid jet is the working principle of the gas focusing technique that is used in GDVNs, see section 3.1.[38] The

[35]Helmholz, H. *Monat. Königl. Preuss. Akad. Wiss. Berlin* **23**, (1886), 215; Kelvin, L. *Phil. Mag.* **42**, (1871), 362.
[36]Batchelor, G.K. *An Introduction to Fluid Dynamics.* Cambridge University Press, 1967.
[37]Lin, S.P. *Breakup of Liquid Sheets and Jets, Chapter 7: Inviscid Jets.* Cambridge University Press, 2003.
[38]A.M.Gañán-Calvo et al. *Phys. Fluids* **26**, (2014), 061701.
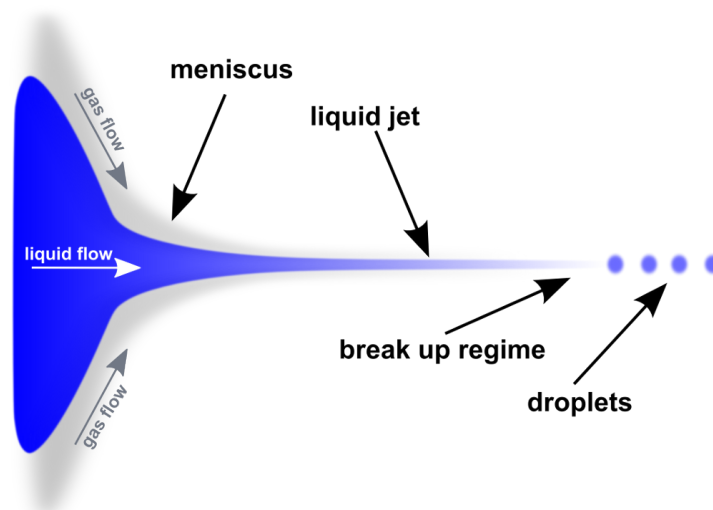
Figure 3.8: Schematic image of different regions of a liquid jet produced by a gas dynamic virtual nozzle.

surrounding gas presses the liquid jet and forms in this way a liquid meniscus, see figure 3.8. The gas stream generates vorticities on the jet and influences the dispersion relation of the capillary waves on the jet surface. This leads to a reduction of the interaction length Λ.

In addition to the capillary pinching other instabilities such as swirling or dithering can occur. To describe all instabilities using the Navier-Stokes equations is difficult because they often end up in complex numerical solutions. Therefore, instabilities are often described by dimensionless flow parameters. One of the first studies on the stability of liquid jets with such parameters was performed by Leib and Goldstein 1986. They predicted a stability-instability transition as function of the Reynolds and Weber numbers.[39] More recently Vega et al. studied the stability of jets formed by a GDVN and identified three different regimes: (I) the steady jetting regime, where the liquid meniscus and the jet is stable; (II) the local instability regime, where the meniscus is stable and the jet is unstable; and (III) the global instability regime, where the liquid meniscus is unstable and the jet is not formed.[40] In figure 3.9 the general shape of a $We\text{-}Re$ plane for a liquid jet system is shown. The red curve represents the stability-instability transition for capillary jets published by Leib et al.[41] The blue curve is valid for jets formed by GDVNs. Furthermore, the stability regions of a GDVN are depicted. A more detailed classification of these regions can be found in literature.[42] The locations of these

[39]Leib, S.J. et al. *Phys. Fluids* **29**, (1986), 952.
[40]Vega, E.J. et al. *Phys. Fluids* **22**, (2010), 064105.
[41]Leib, S.J. et al. *Phys. Fluids* **29**, (1986), 952.
[42]Si, T. et al. *J. Fluid Mech.* **629**, (2009), 1.
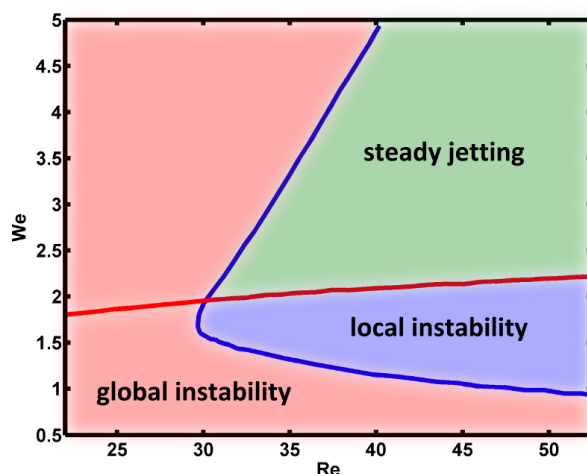
Figure 3.9: General shape of a *We-Re* plane. The red curve shows the Leib and Goldstein prediction for instability transition and the blue curve represents the stability prediction for jet formed by a GDVNs. Image adapted from: Vega, E.J. et al. *Phys. Fluids* **22**, (2010), 064105.

regions in the *We-Re* plane are defined by the geometry of the nozzle and can shift to higher and lower Reynolds number *Re*.[43] Therefore, the nozzle predefine the jetting regimes and thereby flow parameters for the jet formation.[44] How to build a nozzle and which parameters are important for the production is explained in appendix A.1. The different instability regions in the *We-Re* plane of a liquid jet are used in combination with other applications such as a micro mixer.[45] Recently, a newly designed of a GDVN that offers the mixing of two liquids at the nozzle tip was published.[46]

3.2.2 Geometry

A liquid jet can be treated as a cylinder with break-up length L and diameter $d_{\text{jet}} = 2 \cdot r_{\text{jet}}$. The break-up length L is defined by a break-up time τ_b which is given by[47]

$$\tau_b = \frac{1}{\Omega \ln\left(\frac{r_{\text{jet}}}{A_0}\right)}. \tag{3.12}$$

[43] Vega, E.J. et al. *Phys. Fluids* **22**, (2010), 064105.
[44] Acero, A.J. et al. *J. Micromech. Microeng.* **22**, (2012), 065011; Montanero, J.M. et al. *J. Micromech. Microeng.* **20**, (2010), 075035.
[45] Gañán-Calvo, A.M. et al. *Microfluid Nanofluid* **11**, (2011), 65; Marmiroli, B. et al. *J. Synch. Rad.* **21**, (2013), 1.
[46] Wang, D. et al. *J. Synchrotron Rad.* **21**, (2014).
[47] Lin, S.P. et al. *Annu. Rev. Fluid. Mech.* **30**, (1998), 85.

The break-up length is then given by

$$L = v_{\text{jet}} \tau_b = \frac{v_{\text{jet}}}{\Omega \ln\left(\frac{r_{\text{jet}}}{A_0}\right)}. \tag{3.13}$$

It can be seen from equation 3.13 that the flow velocity v_{jet} is proportional to the break-up length L. This is the working principle of a Rayleigh nozzle. The flow velocity of the liquid is maximized to increase the break-up length and thereby to form a liquid jet. Reitz et al. calculated the maximum break-up length L of capillary jets with numerically fits from the dispersion relation.[48] For the maximum growth rate Ω and the corresponding interaction length Λ of the instabilities they found

$$\frac{\Lambda}{r_{\text{jet}}} = 9.02 \frac{(1 + 0.45 Z^{0.5})(1 + 0.4 T^{0.7})}{(1 + 0.87 We_2^{1.67})^{0.6}}, \tag{3.14}$$

$$\Omega \frac{\rho_1 r_{\text{jet}}^3}{\sigma^{0.5}} = \frac{0.34 + 0.38 We_2^{1.5}}{(1 + Z)(1 + 1.4 T^{0.6})}, \tag{3.15}$$

where $Z = \frac{\sqrt{We_1}}{Re_1}$, $T = Z\sqrt{We_2}$, $We_1 = \rho_1 U^2 \frac{r_{\text{jet}}}{\sigma}$, $We_2 = \rho_2 U^2 \frac{r_{\text{jet}}}{\sigma}$, $Re_1 = \frac{U r_{\text{jet}}}{v_{\text{jet}}}$, and $U = \frac{v_{\text{jet}}}{v_{\text{gas}}}$. It can be seen from equations 3.14 and 3.15 that the interaction length Λ is inversely proportional to the Weber number We while the maximum growth rate Ω is proportional to it. Thus an increase of flow velocity leads to an increase of the break-up length L and to a decrease of the interaction length Λ. The impact of viscosity on flow, which is described by the Reynolds number Re, reduces the break-up length and expands the interaction length (equation 3.14 and 3.15).

In figure 3.10 different regimes of the break-up length as function of the flow velocity are shown. At low v_{jet} (ABC) the kinetic energy of the flowing liquid is not sufficient for the jet formation. At least a minimum kinetic energy to form a jet is necessary. Therefore, the nozzle forms only droplets. Above this limit (region CD) the break-up length can be approximately described by[49]

$$L = 12 \cdot v \left[\sqrt{\frac{\rho_l \cdot d^3}{\sigma}} + \frac{3\eta \cdot d}{\sigma} \right]. \tag{3.16}$$

---

[48] Reitz, R.D. et al. *The Encyclopedia of Fluid Mechanics, Chapter 10: Mechanisms of Breakup of Round Liquid Jets.* Gulf, Housten, 1986.

[49] Goldin, M. et al. *J. Fluid Mech.* **38**, (1969), 689; Sterling, A.M. et al. *J. Fluid Mech.* **68**, (1975), 477; Reitz, R.D. et al. *The Encyclopedia of Fluid Mechanics, Chapter 10: Mechanisms of Breakup of Round Liquid Jets.* Gulf, Housten, 1986.
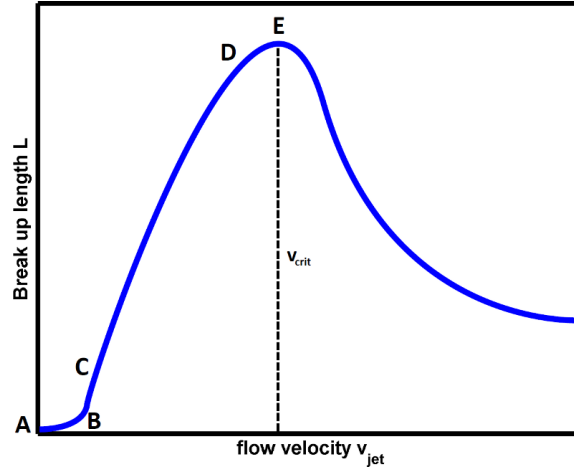
Figure 3.10: Overview of break-up length regimes for a capillary jet. Image adapted from: Lin, S.P. et al. *Annu. Rev. Fluid. Mech.* **30**, (1998), 85.

The break up length is maximized at the critical flow velocity v_{crit} at point E. Any further increase of velocity results in a decrease of the break-up length because the jet tumbles into turbulence and may swirl.[50] Moreover, an increase of flow velocity can lead to a spray.[51]
This general shape of the break-up length L is valid for a jet generated by a Rayleigh nozzle e.g. without surrounding gas stream. Up to now no analytical expression for the break-up length L of a liquid jet formed with a co flowing gas stream is known. However, Eroglu et al. found an empirical expression to describe the break-up length L of such jets[52]

$$L \sim 2 r_{jet} \left(0.5 \cdot W e_{jet}^{-0.4} R e_{gas}^{0.6} \right). \qquad (3.17)$$

It is a numerical relation between the break-up length, the Weber number of the liquid and the Reynolds number of the gas.
For the analytical description of the jet diameter d_{jet} a so called momentum-equation can be used.[53] The mathematical problem is a non-linear differential equation and was first solved by Clarke, 1966.[54] However, for the full description of the liquid jet geometry some approximations have to be taken into account. This was first done by Eggers et al. with the so called slender approximation.[55] It is assumed that the flow is along one axis and that the velocity profile is effectively one-dimensional. These approximations are valid for thin and

[50]Eggers, J. et al. *Rep. Prog. Phys.* **71**, (2008), 036601; Brenner, M.P. et al. *Phys. Fluids* **9**, (1997), 1573.
[51]Eggers, J. *Phys. Fluids* **7**, (1994), 941; Toennies, J.P. et al. *J. Chem. Phys.* **66**, (1977), 3965; Stone, H.A. *Annu. Rev. Fluid Mech.* **26**, (1994), 65.
[52]Eroglu, H. et al. *Phys. Fluids A* **3**, (1991), 303.
[53]Gañán-Calvo, A.M. *Phys. Rev. Lett.* **80**, (1998), 285.
[54]Clarke, N.S. *Mathematika* **12**, (1966), 51.
[55]Eggers, J. *Rev. Mod. Phys.* **69**, (1997), 865; Eggers, J. *Phys. Rev. Lett.* **71**, (1993), 3458.

long liquid jets, which are mainly driven by one force coming from one direction. Taking this into account the mathematical problem for the description of the liquid jet diameter simplifies to[56]

$$\frac{d}{dx}\left(\frac{\sigma}{r} + \frac{\rho_l Q^2}{2\pi^2 r^4}\right) + \frac{6\eta Q}{\pi r^2}\frac{d}{dx}\left(\frac{1}{r}\frac{dr}{dx}\right) = F(x),\tag{3.18}$$

where $F(x)$ represents the driving forces of the flow. These forces depend on the nozzle design. For a pressure driven flow the general shape is $F(x) = \frac{dp_{\text{jet}}}{dx} - \frac{2\eta}{r}$, where the pressure p_{jet} is the liquid pressure p_l. For a GDVN it is characterized by the pressure drop Δp which is the absolute difference between the co-flowing gas pressure p_g and the liquid pressure p_l. These forces are converted into surface energy and kinetic energy, given by $\frac{\sigma}{r}$ and $\frac{\rho_l Q^2}{2\pi r^4}$ on the left side of the equation. In addition to these terms the extensional viscous stress is given by $\frac{6\rho_l Q}{\pi r^2}\frac{d}{dx}\left(\frac{1}{r}\frac{dr}{dx}\right)$. A further simplification is to neglect these terms to obtain the following equation

$$\frac{d}{dx}\left(\frac{\rho_l Q^2}{2\pi^2 r^4} - p_{\text{jet}}\right) = 0.\tag{3.19}$$

The integration of this equation leads to an estimation of the jet radius

$$r_{\text{jet}} = r = \left(\frac{\rho_l Q^2}{2\pi p_{\text{jet}}}\right)^{1/4}.\tag{3.20}$$

This result was first calculated and verified for GDVN jets by comparisons with experimental results by Gañán-Calvo et al.[57] Montanero et al. verified these results by comparing experimental and numerical results calculated with the Navier Stokes equitations 3.4, 3.5, and 3.6.[58] They found that the universal solution of the momentum equation 3.18 is a good estimate for the shape and size of liquid jets.

3.2.3 Thermodynamics

Gañán-Calvo et al. studied by numerical simulations the pressure and temperature distribution of a liquid jet formed by a GDVN.[59] They showed that the focusing gas cools down to $T = 150\,\text{K}$ due to expansion while exiting the nozzle, see figure 3.11. In contrast to this, the temperature of the liquid does not change in the jet. The liquid jet is not significantly

---

[56]Gañán-Calvo, A.M. et al. *J. Fluid Mech.* **670**, (2011), 427; Montanero, J.M. et al. *Phys. Fluids* **23**, (2011), 122103.
[57]Gañán-Calvo, A.M. *Phys. Rev. Lett.* **80**, (1998), 285.
[58]Montanero, J.M. et al. *Phys. Fluids* **23**, (2011), 122103.
[59]Gañán-Calvo, A.M. et al. *Small* **6**, (2010), 822.

expanding due to the surrounding gas pressure and therefore the volume of the fluid is not changing in contrast to the focusing gas.

However, the droplets cool down due to evaporation in the vacuum and to the corresponding latent heat.[60] The modeling of the evaporation of water droplets formed in a break-up process in vacuum was performed by Faubel et al. with five assumptions:[61]

- Free-molecular flow away from the droplet surface.

- Uniform temperature within the droplet.

- Effusive mass loss from the droplet surface at a rate set by the vapor pressure of the liquid at the droplet temperature.

- Evaporative cooling of the droplet via latent heat of evaporative mass loss.

- Negligible changes of the surface area and hence of the total surface energy.

Taking these assumptions into account it is possible to show that for a spherical droplet of temperature T and radius r_d as function of distance x from the jet break-up the temperature gradient and the droplet radius are described by[62]

$$\frac{dT(x)}{dx} = -\frac{3\Pi}{c_p r_d(x)} \cdot \frac{dr(x)}{dx}, \tag{3.21}$$

$$\frac{dr(x)}{dx} = -\frac{P[T(x)]}{v_d \rho} \cdot \sqrt{\frac{m}{2\pi k_B T(x)}}, \tag{3.22}$$

where Π is the latent heat of vaporization of the liquid, c_p is the specific heat capacity at constant temperature T, m the mass of a molecule, v_d the droplet velocity, $P[T(z)]$[63] is the vapor pressure at the instantaneous temperature T of the droplet. Numerical calculations of the differential equations 3.21 and 3.22 can be done with the Runge-Kutta method. Results for five different initial water droplets are shown in figure 3.12. Each droplet reaches temperatures below the freezing temperature of water. Moreover, small droplets cool to lower temperatures than large droplets. This is connected to a pronounced change of the droplet size.[64] These predictions were verified with Raman spectroscopy.[65] The cooling rate of the droplets in this

[60]Weierstall, U. et al. *Exp. Fluids* **44**, (2008), 675; Deponte, D.P. et al. *J. Phys. D: Appl. Phys.* **41**, (2008), 195505.
[61]Faubel, M. et al. Z. *Phys. D* **10**, (1988), 269.
[62]Faubel, M. et al. Z. *Phys. D* **10**, (1988), 269.
[63]The empirical Goff-Gratch equation can be used to estimate the saturation water vapor pressure.
[64]French, J.B. et al. *Anal. Chem.* **66**, (1994), 685; Grisenti, R.E. et al. *Europhys. Lett.* **73**, (2006), 540.
[65]Wilson, K.R. et al. *Rev. Sci. Inst.* **75**, (2004), 725; Faubel, M. et al. Z. *Phys. D* **10**, (1988), 269.
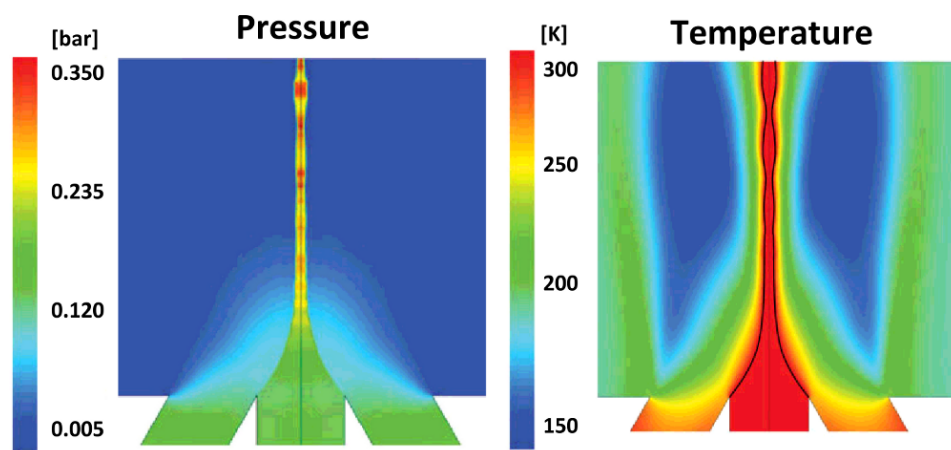
Figure 3.11: Two results from numerical simulations of a jet formed by a GDVN. The jet is injected from the bottom to the top. Left: Pressure distribution. Right: Temperature distribution. Images adapted from: Gañán-Calvo, A.M. et al. *Small* **6**, (2010), 822.

region depends on the droplet size varying between $10^4 \frac{K}{s}$ and $10^6 \frac{K}{s}$. Thus, for a uniform droplet temperature at a certain distance from the break up a uniform droplet size is necessary. The spontaneous break-up is not uniform and results into polydisperse droplet sizes, see figure 3.13 a). For a monodisperse droplet size a single wave number k_r of a single instability can be stimulated. This can be done by e.g. mechanic vibrations from a piezo actuator mounted at the nozzle.[66] To excite waves on the jet surface the wavelength of the piezo vibration λ_p has to fulfill the equations[67]

$$\lambda_p > \pi \cdot d_{\text{jet}}. \tag{3.23}$$

Figure 3.13 shows three jets with and without a triggering signal. For higher trigger frequencies the droplets are monodisperse and the break-up length moves upstream into the GDVN. The droplet diameter can be changed by regulating the gas pressure.[68] At a low gas pressure it is approximately twice that of the jet diameter (equation 3.11), while at a high gas pressures the droplets diameter decrease down to the jet diameter. Gordillo et al. studied the stability of this effect and explained it with high shear forces arising from the Helmholtz-Kelvin instability.[69] This property was also studied for the use in the pharmaceutical industry to produce micro droplets.[70]

---

[66]Weierstall, U. et al. *Exp. Fluids* **44**, (2008), 675; Deponte, D.P. et al. *J. Phys. D: Appl. Phys.* **41**, (2008), 195505.
[67]Private communication D.P. Deponte.
[68]Liu, Z. et al. *Int. J. Multiphase Flow* **23**, (1996), 631.
[69]Gordillo, J.M. et al. *J. Fluid. Mech.* **448**, (2001), 23.
[70]Gañán-Calvo, A.M. et al. *Adv. Drug. Del. Rev.* **65**, (2013), 1447.
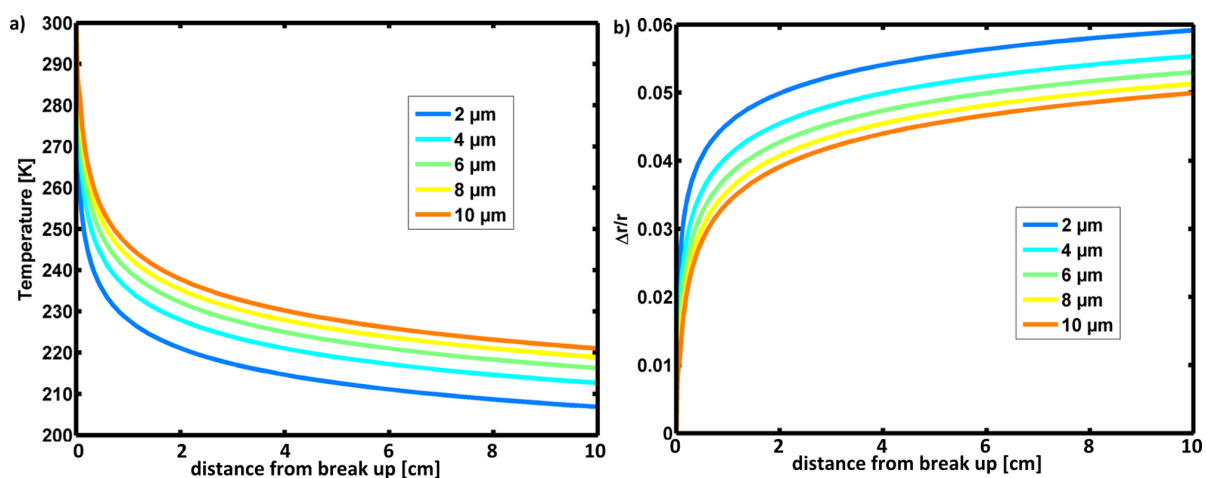
Figure 3.12: Left: Droplet temperature T as function of the distance to the liquid jet break up calculated for different droplet radii. The calculation were performed with a droplet velocity of $v_d = 1\frac{m}{s}$. Right: Relative change of the droplet size due to evaporation in vacuum calculated for different initial droplet diameter.
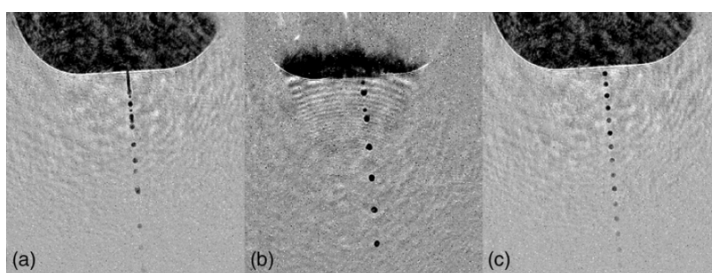
Figure 3.13: Microscope images of a GDVN producing liquid jets. The nozzle appears as a dark object at the top. (a) Untriggered operation showing spontaneous break-up. (b) Breakup triggered at 73 kHz. Droplet diameter is 25 µm. (c) Breakup triggered at 169 kHz. Droplet diameter is 20 μm. Deponte, D.P. et al. *J. Phys. D: Appl. Phys.* **41**, (2008), 195505.

4 Flow characterization

Liquid jets allow investigating complex liquids, spatially confined under shear flow conditions in small dimensions. In particular, fluid samples, that are sensitive to shear, can be affected by the jet. Therefore, the understanding of the flow properties of a liquid jet and their influence on the liquid sample is of importance.

Colloidal dispersions often serve as model systems for soft condensed matter. They are sensitive to shear flows by agglomerating or aligning to a preferred orientation. Thus, colloidal particles are excellent tracer particles in x-ray scattering experiments with liquid jets.

In this chapter the experiments with liquid jets and colloids as tracer particles are presented. By using small angle x-ray scattering (SAXS) the colloidal dispersions were studied in a liquid jet. In section 4.1 a general introduction into the behavior of colloidal particles under shear is given. In the framework of this thesis experiments with two different colloidal dispersions were performed. In section 4.2 the results and experiments with silica colloids are discussed, while section 4.3 deals with the experiment with dispersed hematite colloids in a liquid jet.

4.1 Colloidal dispersions in shear flows

Colloids are particles dispersed in a continuous medium. This medium can be gaseous, liquid or solid. The size of the dispersed colloids range from a few nm to the μm regime.[1] The particles are not dissociated in the suspending medium. Colloidal dispersions are known to show non-Newtonian behavior under shear by forming agglomerates or particle alignment. As a consequence the viscosity of the dispersion is influenced by the colloidal arrangement or alignment. It can be reduced in the so-called shear thinning regime or it can be increased in the shear-thickening regime. Which regime is present depends on the structure or alignments of the particles. In order to describe the properties of colloidal dispersions under shear a few parameters have to be introduced. In figure 4.1 the geometry of a sheared system is depicted.

---

[1]Larson, R.G. *Soft Matter Physics: An Introduction*. New York: Springer-Verlag, New York, Inc., 2003.
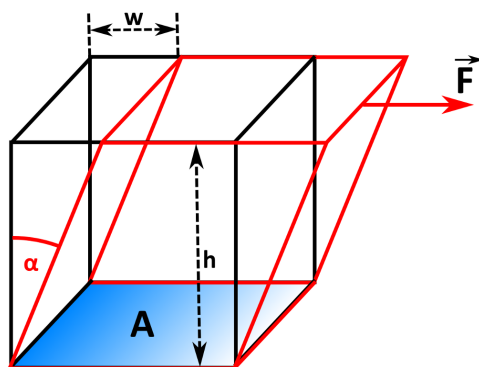
Figure 4.1: Sketch of a sheared box with height h and area A. A force $\vec{F}$ deforms the geometry by an angle α and a length w.

The shear stress $\vec{\tau}$ is the ratio of the shear force $\vec{F}$ and the area A that is affected by this force

$$\vec{\tau} = \frac{\vec{F}}{A}. \tag{4.1}$$

The shear stress thus represents a pressure. The shear strain γ is given by the ratio of the length h and w

$$\gamma = \frac{w}{h} = \tan \alpha. \tag{4.2}$$

The strain change per time is the so-called shear rate $\frac{d\gamma}{dt} = \dot{\gamma}$. In general, the impact of shear on a colloidal dispersion is described by the Péclet number. It is the ratio between the shear rate $\dot{\gamma}$ and the particle diffusion constant D of Brownian motion[2]

$$Pe = \frac{\dot{\gamma}}{D}. \tag{4.3}$$

The particle diffusion constant D depends on the particle shape. For spherical particles it is given by

$$D = \frac{k_B T}{6\pi\eta_0 R_0} \tag{4.4}$$

where η_0 denotes the viscosity of the solvent, and R_0 is the particle radius. For elongated particles with large aspect ratio $\nu \gg 1$ the diffusion can be approximated by

$$D = \frac{3k_B T \left(\ln 2\nu - \frac{1}{2}\right)}{6\pi\eta_0 R_1}, \tag{4.5}$$

---

[2]Macosko, C.W. *Rheology Principles, Measurements, and Applications*. Toronto, Canada: Wiley-VCH, 1994.

where R_1 is the minor semi-axis of the particle. The colloids used in this work have two different particle shapes. Furthermore, the particle concentration of the two dispersions differs from each other. This leads to different pronounced interactions and different effects under shear. At small concentrations, the particle-fluid interaction is pronounced and an interaction with walls from the surrounding plenum (capillary) plays for the rheological response a significant role, while at high concentration the particle-particle interaction dominates the colloidal dispersion.

- **Particle-wall interaction**

  The interaction of colloidal particles with walls in a pressure driven flow[3] can lead to an inertia migration of the particles, see figure 4.2 a).[4] This means that the colloids are inhomogeneously distributed across the flow. A particle migration leads to an increase of volume fraction ϕ, while a depletion of particle leads to an decrease of the volume fraction ϕ, see figure 4.2 b). This effect depends on several properties such as the particle
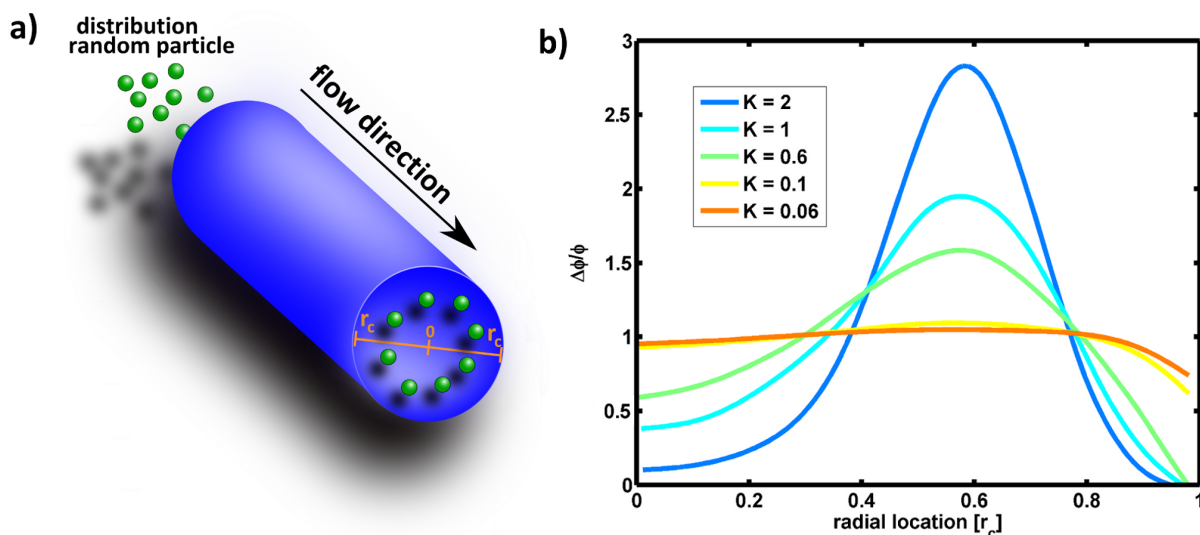
Figure 4.2: a) Sketch of a shear flow with particle migration. b) Concentration distribution across the shear flow for various K values. The plot is adapted from Ho, B.P. et al. *J. Fluid Mech.* **65**, (1973), 365.

shape or flow rate.[5] For spherical particles an empirical criteria for inertia migration in a flow is given by[6]

$$K = \frac{\rho_p v^2 R^4}{2 r_c k_B T} < 0.01 \tag{4.6}$$

---

[3]Known as Poiseuille flow or capillary flow.
[4]Segre, G. et al. *Nature* **189**, (1961), 209.
[5]Carlo, D.D. *Lab Chip* **9**, (2009), 3038.
[6]Ho, B.P. et al. *J. Fluid Mech.* **65**, (1973), 365.

where ρ_p is the particle density, v is the flow velocity, and r_c is the radius of the cross section of the flow. For $K < 0.01$ particle migration can be neglected. If the particle is small and the flow rate is low, Brownian motion can keep the particles uniformly distributed.[7] In case of particle migration ($K > 0.01$) the particles migrate in a pressure driven flow at a radial location of $\frac{3}{5}r_c$, see figure 4.2 b).[8]

- **Particle-fluid interaction**

  In contrast to spherical particles, elongated particles can align in shear flows. The hydrodynamic interaction of elongated colloids leads to an particle alignment, while the Brownian motion of the particle randomizes the particle orientation.[9] For small particles the shear rate and viscosity is low and the Brownian motion randomize the particle orientation and $Pe = 0$, see equation 4.5. At high viscosity and shear rate or large aspect ratios the particles align to a preferred direction as $Pe \to \infty$. Elongated particles in a dispersion are not always aligned in the same direction. Thus, an orientation distribution function as function of the polar and azimuthal angle $f(\theta_g, \phi_g)$ has to be taken into account to describe properties of the dispersion, see figure 2.9. Changes of this distribution can be described by a dynamic conservation equation[10]

  $$\frac{\partial f(\theta_g, \phi_g)}{\partial t} + \nabla \cdot (j_h + j_d) = 0, \tag{4.7}$$

  where j_h is the hydrodynamic convection and j_d the rotation flux from the Brownian motion. With the angular velocity $\vec{\Omega}$ and the particle orientation $\vec{g}$ the angular motion can be described by $\vec{\Omega} \times \vec{g}$ and the Brownian motion can be written with the diffusion coefficient $D\nabla f(\theta_g, \phi_g)$. In this way equation 4.7 modifies to

  $$\frac{\partial f(\theta_g, \phi_g)}{\partial t} + \nabla \cdot (f(\theta_g, \phi_g) \cdot \vec{\Omega} \times \vec{g}) - D\nabla^2 f(\theta_g, \phi_g) = 0. \tag{4.8}$$

  This general equation for rotational motion of elongated particles has to be solved for each flow and particle shape. For the assumption of $Pe \gg 1$ and $D \ll 1$ the angular motion was solved. The trajectory $\Phi(\theta_g, \phi_g)$ of $\vec{g}$ for spheroids under shear is given

---

[7]Macosko, C.W. *Rheology Principles, Measurements, and Applications*. Toronto, Canada: Wiley-VCH, 1994.

[8]Ho, B.P. et al. *J. Fluid Mech.* **65**, (1973), 365; Segre, G. et al. *Nature* **189**, (1961), 209.

[9]Macosko, C.W. *Rheology Principles, Measurements, and Applications*. Toronto, Canada: Wiley-VCH, 1994.

[10]Brenner, H. *Int. J. Multiphaseflow* **1**, (1974), 195; Hinch, E.J. et al. *J. Fluid Mech.* **52**, (1972), 683.
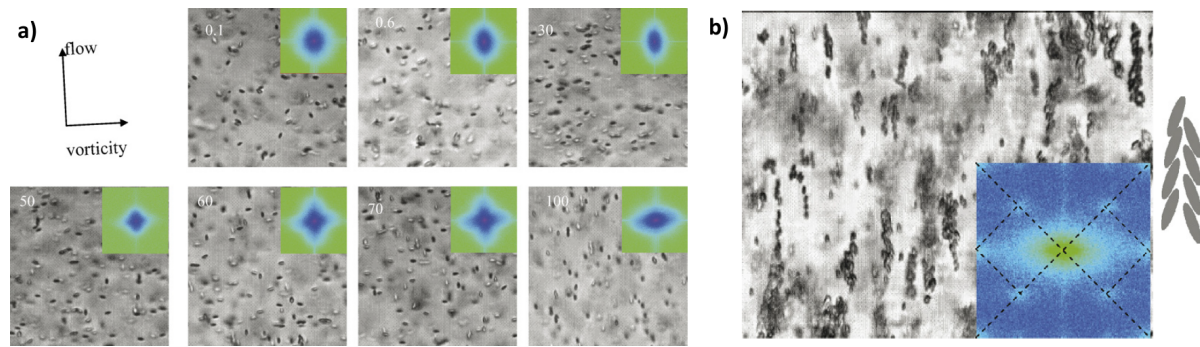
Figure 4.3: Microscope images of spindle-shaped particles (aspect ratio $r = 3.8$, length $l = 2.9\,\mu$m) at different Péclet number Pe. a) Different alignments of elongated particles at different Péclet numbers. The Péclet number is given at the top left corner of each image. Moreover, the Fourier transform of the images are shown top right. b) Microscope image showing the particle alignment at shear rate of $\dot{\gamma} = 50\,\text{s}^{-1}$. The cartoon at the right side represents the agglomerated particles. Gunes, D.Z. et al. *J. Non-Newtonian Fluid Mech.* **155**, (2008), 39.

by[11]

$$\frac{d\Phi}{dt} = \frac{\dot{\gamma}}{v^2 + 1}(v^2 \cos(\Phi) + \sin(\Phi)). \tag{4.9}$$

Integration of equation 4.9 yields

$$\tan(\Phi) = v \tan\left(\frac{\dot{\gamma}t}{v + \frac{1}{v}}\right), \tag{4.10}$$

and the period of rotation is given by

$$T_{\text{rot}} = \frac{2\pi}{\dot{\gamma}}\left(v + \frac{1}{v}\right). \tag{4.11}$$

For high shear rates $\dot{\gamma} \to \infty$ the speed of alignment is fast ($T_{\text{rot}} \to 0$), while it is slow at low shear rate $\dot{\gamma} \to 0$ ($T_{\text{rot}} \to \infty$).

Different experiments show an alignment of elongated particles under shear.[12] As can be seen from equation 4.5 and 4.3 the particle shape influences the impact of shear on dispersions. Thus, during the last years plate-like and rod-like particles attracted

---

[11]Jeffery, G.B. *Proc. R. Soc.* **A 102**, (1922), 161.

[12]Trebbin, M. et al. *PNAS* **110**, (2012), 6706; Junaid, S. et al. *Langmuir* **26**, (2010), 18701; Jia, X. et al. *J. Phys. Chem. B* **115**, (2011), 13441; Bihannic, I. et al. *J. Phys. Chem. B.* **114**, (2010), 16347; Gunes, D.Z. et al. *J. Non-Newtonian Fluid Mech.* **155**, (2008), 39; Wegner, S. et al. *Soft Matter* **8**, (2012), 10950; Philippe, A.M. et al. *Langmuir* **29**, (2013), 5315; Cheng, X. et al. *Science* **333**, (2011), 1276; Joung, C:G. *Rheol. Acta* **46**, (2006), 143.
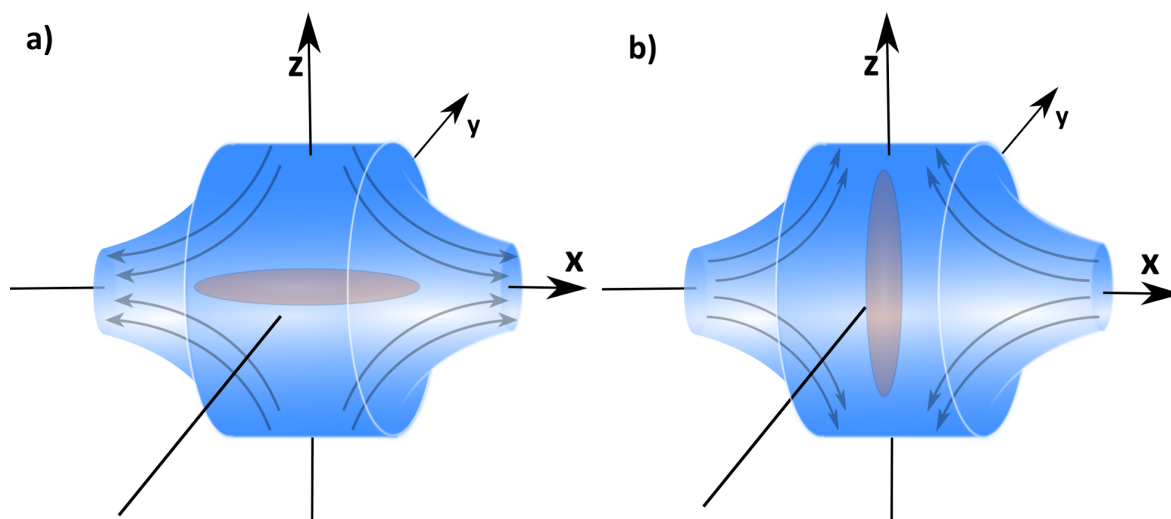
Figure 4.4: Two sketches of dispersions with elongated particles in shear flows . a) The dispersion is compressed parallel to $z-y$-plane and expanse parallel to x-plane. b) The dispersion expands parallel to $z-y$-plane and is compressed parallel to x-plane. Images are adapted from Macosko, C.W. *Rheology Principles, Measurements, and Applications*. Toronto, Canada: Wiley-VCH, 1994

increasing scientific interest and were studied by x-ray scattering and rheology.[13] Gunes et al. investigated experimentally the behavior of spindle-shaped particles under shear at different aspect ratios with rheology and flow microscopy.[14] They showed that different alignments of elongated particles lead to different Péclet numbers Pe, see figure 4.3 a). For $Pe > 70$ a particle alignment in flow direction was measured, while for $Pe < 50$ the particles were aligned perpendicular to the flow direction. At the transition region of these two regimes $(70 > Pe > 50)$ multiple particle orientations were measured, see figure 4.3 b).

 The contribution of the particle orientation to the viscosity in a shear flow was first analyzed by Brenner in 1974.[15] If an elongated particle is aligned with its major axis parallel to the flow direction the flow resistance of the particle is minimized. This particle orientation leads to a shear thinning. If the major axis of the particle is aligned perpendicular to the flow direction, the flow resistance of the particle is maximized and shear thickening is present. In figure 4.4 these two configurations are depicted. In the first configuration (figure 4.4 a)) the dispersion with the elongated particle is compressed parallel to the $y-z$-plane and expands parallel to the x-axis. Elongated

[13]Junaid, S. et al. *Langmuir* **26**, (2010), 18701; Bihannic, I. et al. *J. Phys. Chem. B.* **114**, (2010), 16347; Gunes, D.Z. et al. *J. Non-Newtonian Fluid Mech.* **155**, (2008), 39; Wegner, S. et al. *Soft Matter* **8**, (2012), 10950.

[14]Gunes, D.Z. et al. *J. Non-Newtonian Fluid Mech.* **155**, (2008), 39.

[15]Brenner, H. *Int. J. Multiphaseflow* **1**, (1974), 195.

particles align in this flow configuration parallel to the x-axis. This configuration is called uni-axial expansional flow. An uni-axial compressional flow is depicted in figure 4.4 b). In this configuration is compressed parallel to the x-axis and expanse parallel to the $y-z$-plane. Elongated particles align in such a flow configuration in the $y-z$-plane.

- **Particle-particle interaction**

  At high particle concentrations the inter particle interaction dominates the colloidal dispersion. In this way it contributes to the viscosity of the dispersion. For charged spherical particles the viscosity can be approximated by[16]

$$\eta = \eta_0 \left(1 + \frac{5}{2}\phi + H\phi^2 \right). \tag{4.12}$$

The linear term in equation 4.12 represents the contribution from the particle volume fraction ϕ on the viscosity of the dispersion.[17] The quadratic term represents the electrostatic repulsion in the limit of low shear forces.[18] The coefficient H is given by

$$H = \left(\frac{1}{\varkappa} \right) \ln\left[\frac{\alpha}{\ln(\alpha/\ln\alpha)} \right] \tag{4.13}$$

with $\alpha = 4\pi\epsilon\Psi_s R_0^2 \varkappa \exp(2R_0\varkappa)/k_B T$. Here $\varkappa$ is the Debye-Hückel constant and ϵ the
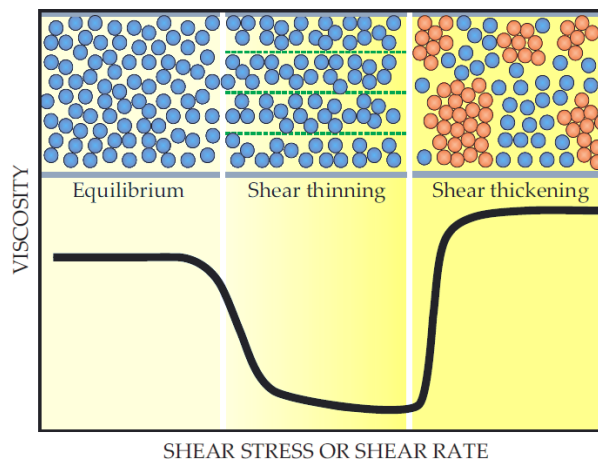
Figure 4.5: Overview about three different non-Newtonian regimes in shear flows in dependency of viscosity and shear rate or stress. Wagner, N.J. et al. *Physics Today* **62**, (2009), 27.

permittivity of the solvent, see section 2.3.1. The parameter Ψ_s is the so-called surface

[16]Macosko, C.W. *Rheology Principles, Measurements, and Applications.* Toronto, Canada: Wiley-VCH, 1994.
[17]Einstein, A. *A. Ann. Phy.* **19**, (1906), 289; Einstein, A. *A. Ann. Phy.* **34**, (1911), 591.
[18]Batchelor, G.K. *J. Fluid Mech.* **83**, (1977), 97.
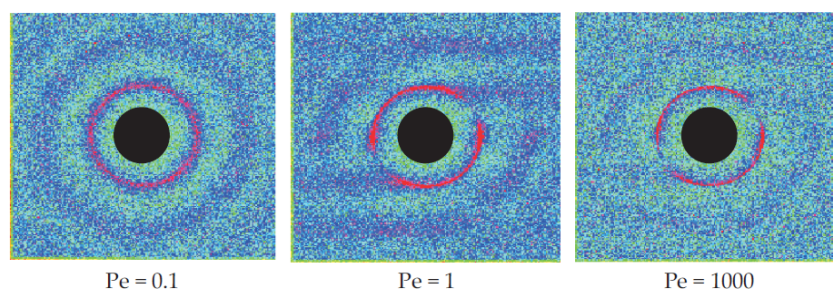
Figure 4.6: Pair distribution functions $g(r)$ from simulations at three different Péclet numbers Pe. Wagner, N.J. et al. *Physics Today* **62**, (2009), 27.

potential which can be calculated from the surface charge Ψ[19]

$$\Psi_s = \frac{\Psi}{\epsilon \epsilon_0 \varkappa}. \tag{4.14}$$

The non-Newtonian behavior under shear is affected by the balance of inter-particle forces, Brownian motion and hydrodynamic interaction. Thus, beside the shear rate and shear stress the impact of shear flow on colloidal dispersion depends on temperature, particle concentration, particle size and shape. No analytical solution is available to consider all these values for a description of a sheared system. Numerical simulations of concentrated colloidal dispersions under shear predict in general particle ordering or agglomeration of particles.[20] This influences the viscosity of the sample system, see figure 4.5.[21] If no shear is present the colloidal dispersions will provide an unordered equilibrium state. At moderate shear rates or shear stress of the colloids can order or align in layers along the flow direction.[22] In this regime, the particle order minimizes the flow resistance in the dispersion. Consequently, the viscosity of the dispersion decreases. This is the shear thinning regime. At high shear rate or stress the hydrodynamic inter-actions are pronounced and the attractive forces can become larger than the repulsion of the inter particle interaction. In this case the particles can remain together when they collide and agglomerates can be formed.[23] Neutron scattering experiments verified

---

[19] Larson, R.G. *The Structure and Rheology of Complex Fluids*. New York: Oxford University Press, 1999.

[20] Vermant, J. et al. *J. Phys.: Condense Matter* **17**, (2005), R187; Brader, J.M. *J. Phys.: Condense Matter* **22**, (2010), 363101; Stickel, J.J. et al. *Annu. Rev. Fluid Mech.* **37**, (2005), 129; Martys, N.S. et al. *Eur. Phys. J. E* **35**, (2012), 20.

[21] Wagner, N.J. et al. *Physics Today* **62**, (2009), 27; Cheng, X. et al. *Science* **333**, (2011), 1276; Brown, E. et al. *Science* **333**, (2011), 1230.

[22] Santos, I.S. et al. *J. Chem. Phys.* **137**, (2012), 204908; Pasquino, R. et al. *Rheol Acta* **49**, (2010), 993; Scirocco, R. et al. *J. Non-Newtonian Fluid Mech.* **117**, (2003), 183; Melrose, J.R. et al. *J. Rheol.* **48**, (2004), 961.

[23] Macosko, C.W. *Rheology Principles, Measurements, and Applications*. Toronto, Canada: Wiley-VCH, 1994.

the existence of such particle compounds.[24] These particle fragments are known as hydrocluster or flocculate systems.[25] They maximize the flow resistance of the particles and the viscosity of the dispersion increases. This regime is called shear thickening regime.

Simulations of concentrated dispersions with spherical particles under high shear rates show different radial pair distribution functions $g(r)$, see figure 4.6.[26] For low Pe the pair distribution function is isotropic as expected from an unordered dispersions. At high Pe the pair distribution function shows an anisotropy. In general, a deviation from a isotropic pair distribution function is a sign for compression and expansion and a pronounced order, see section 2.3. Taking this into account the anisotropic pair distribution functions in figure 4.6 show a density fluctuation that indicate an ordering of particles. In the simulation study it was claimed that the anisotropy of the pair distribution function indicates the formation of flocculate systems or hydroclusters under shear.

The described sensitivity of colloidal dispersions gives the possibility to use colloids as tracer particles in liquid jets to study shear flows by probing particle structures or alignment. For this purpose x-ray scattering experiments on colloidal dispersions in liquid jets were performed. The shear flow of a Rayleigh nozzle was studied with a concentrated dispersion of spherical silica colloids, see section 4.2. Dispersions with spindle-shaped hematite particles at small concentrations were used to study shear flows of GDVNs, see section 4.3.

4.2 Spherical particles in a liquid jet

In this section a small angle x-ray scattering (SAXS) experiment on colloidal particles in a liquid jet is presented. It was performed using a colloidal dispersion of silica particles in a liquid jet formed by a Rayleigh nozzle.

As sample system a dispersion with spherical silica particles was used. It is a commercially available dispersion bought at Sigma-Aldrich.[27] The solvent of the dispersion is distilled water. The density of the spherical silica particles in the dispersion is 34 wt.%. To characterize the sample measurements were recorded on the sample contained in a capillary. The SAXS

[24]Kalman, D.P. et al. *Rheol. Acta* **48**, (2009), 897; Maranzano, B.J. et al. *J. Chem. Phys.* **117**, (2002), 10291; Foss, D.R. et al. *J. Fluid Mech.* **407**, (2000), 167.

[25]Brown, E. et al. *Nature Mat.* **9**, (2010), 220; Cheng, X. et al. *Science* **333**, (2011), 1276; Wagner, N.J. et al. *Physics Today* **62**, (2009), 27.

[26]Wagner, N.J. et al. *Physics Today* **62**, (2009), 27.

[27]Ludox TMA 420859, Sigma-Aldrich GmbH

experiment using a liquid jet was performed at beamline P10 at PETRA III, while the sample characterization was performed at beamline BW4 at DORIS III. In the following sections the experimental setups, the data treatment, and the results of these experiments are presented.

4.2.1 Experimental Setups

- **Beamline BW4**

  The wiggler beamline BW4 was dedicated to small angle x-ray scattering and wide angle x-ray scattering at DORIS III.[28] The storage ring DORIS III was located at DESY[29] and operated with a ring current of 130 mA at 4.5 GeV. The layout of the beamline BW4 is depicted in figure 4.7. The beamline was equipped with a Si(111) double crystal monochromator to provide monochromatic radiations in the x-ray regime. At an x-ray energy of $E_{\text{x-ray}} = 9\,\text{keV}$ the total photon flux was $6.5 \cdot 10^{10}\,\frac{\text{photons}}{\text{s} \cdot \text{mm}^2}$.[30] The beam was focused using beryllium compound refractive lenses to $30\,\mu\text{m} \times 40\,\mu\text{m}$.[31] The sample
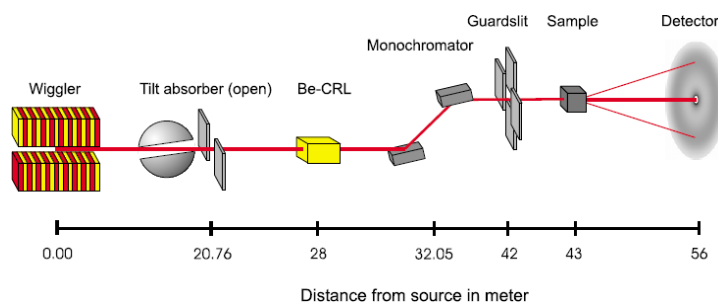
Figure 4.7: Schematic BW4 setup. Timmann, A. et al. *Rev. Sci. Inst.* **80**, (2009), 046103.

- detector distance using the Mar 165 detector was set to $d = 6.26\,\text{m}$. In total ten patterns, each with an exposure time of $t_e = 1\,\text{min}$ were recorded. The inner diameter of the capillary was $0.7\,\text{mm}$ and the outer one $1\,\text{mm}$. In addition, a measurement without sample was taken to determine the background scattering originating from x-ray windows and other components that are hit by the x-ray beam.

- **Beamline P10**

  The undulator beamline P10 is dedicated to coherent scattering techniques such as coherent diffraction imaging (CDI) and x-ray photon correlation spectroscopy (XPCS). The storage ring PETRA III is located at DESY and operates with a ring current of

[28]Perlich, J. et al. *Rev. Sci. Inst.* **81**, (2010), 105105.
[29]Deutsches Elektronen Synchrotron, Hamburg, Germany.
[30]Timmann, A. et al. *Rev. Sci. Inst.* **80**, (2009), 046103.
[31]Roth, S.V. et al. *Rev. Sci. Inst.* **77**, (2006), 085106.
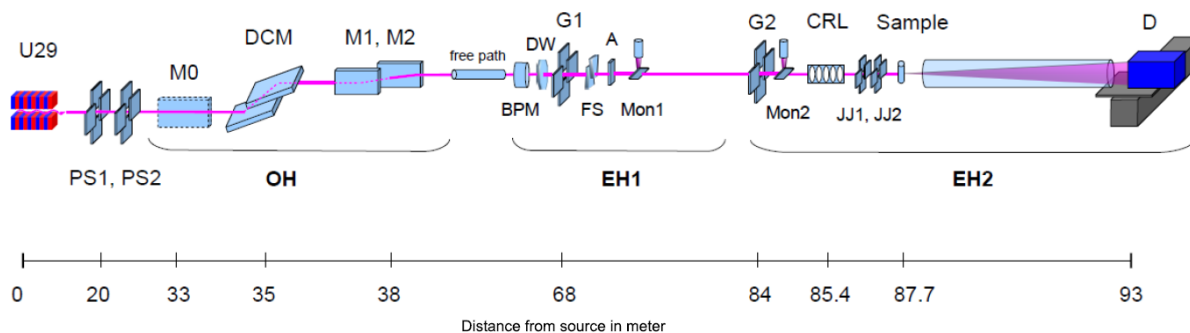
Figure 4.8: Schematic setup of beamline P10 with undulator (U29), monochromator, and slits. The sketch is divided in the optical hutch (OH), experimental hutch 1 (EH1), and experimental hutch 2 (EH2). Sprung, M. *P10 Coherence Beamline User Guide*. 2014. URL: `http://photon-science.desy.de/sites/site_photonscience/content/e58/e176720/e177229/e178737/e179091/e179098/e219987/P10_User_Guide_v01102013_eng.pdf`.

$100\,\text{mA}$ at $6.0\,\text{GeV}$. Beamline P10 is equipped with a Si(111) double crystal monochromator. At $E_{\text{x-ray}} = 8\,\text{keV}$ the total photon flux is $10^7\,\frac{\text{photons}}{\text{s}\cdot\mu\text{m}^2}$. The layout of beamline P10 is depicted in figure 4.8.

The measurements were performed with a focused x-ray beam of beam size $6\,\mu\text{m}$ x $3\,\mu\text{m}$ at an x-ray energy of $E_{\text{x-ray}} = 7\,\text{keV}$. The sample detector distance was set to $d = 5\,\text{m}$. The detector used in this experiment was a Pilatus 300k detector. The jet was formed in air. As Rayleigh nozzle a micro tube (inner diameter $d_i = 100\,\mu\text{m}$, outer diameter $d_o = 375\,\mu\text{m}$[32]) was used. The inner diameter of the micro tube defines the jet thickness to $d_{\text{jet}} = 100\,\mu\text{m}$. Since the focus of the x-ray beam was smaller than the jet diameter, diffraction patterns could be recorded spatially resolved on the liquid jet. The applied liquid pressure was $p_l = 62.2\,\text{bar}$ and the flow rate was approximately $Q \approx 100\,\frac{\text{ml}}{\text{h}}$. Thus the flow velocity can be estimated to $v_{\text{jet}} = 3.5\,\frac{\text{m}}{\text{s}}$. The length of the tube was $l = 12\,\text{cm}$. SAXS patterns were taken $100\,\mu\text{m}$ and $3000\,\mu\text{m}$ downstream of the tube. At these locations the diffraction patterns were recorded in steps of $1\,\mu\text{m}$. In the experiment several hundreds of SAXS patterns were taken on each jet location with an exposure time of $t_e = 0.5\,\text{s}$.

4.2.2 Sample characterization

Ten SAXS pattern have been taken with an exposure time of $t_e = 60\,\text{s}$ on the silica dispersion located in a capillary. A background measurement was subtracted from the diffraction patterns taken on the sample to exclude unintended scattering signals. After this step the

---

[32]TSP100375, Polymicro Gmbh
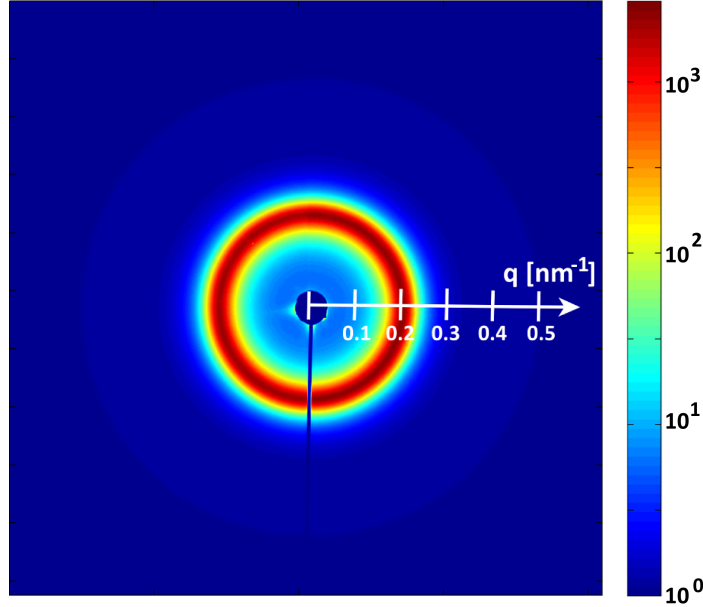
Figure 4.9: Average of ten SAXS patterns ($t_e = 60$ s) on the silica particles ($r = 13\,\mu$m) taken at beamline BW4. The intensity scale represents the detected photons.

ten SAXS patterns have been averaged. The result is shown in figure 4.9. To extract the form factor and the structure factor the pattern was azimuthally integrated. In figure 4.10 a) the result of this integration is shown. In general the scattered intensity is a product of the structure factor and the form factor, see section 2.3. A form factor fit performed with equation 2.10 is plotted in figure 4.10 a). The model is fitted to the data at two q-regimes from $q = 0.28$ nm^{-1} to $q = 0.32$ nm^{-1} and from $q = 0.45$ nm^{-1} to $q = 0.54$ nm^{-1}. The fit results in a particle radius of $R_0 = 12.89$ nm ± 0.65 nm with a polydispersity of $p = 12.4\,\% \pm 0.6\,\%$. The deviations of the form factor fit to the data are however important features in the measured data that are not described by the form factor. These indicate inter-particle correlations described by the structure factor $S(q)$. The structure factor can be extracted via $S(q) = \frac{I(q)}{P(q)}$, see section 2.3. The resulting structure factor is depicted in figure 4.10 b) together with a fit carried out with the RMSA model, see section 2.3.1. The maximum of the first peak of the structure factor is found at $q_{\mathrm{max}} = 0.2$ nm^{-1}. The RMSA model is fitted to the first peak of the structure factor from $q = 0.15$ nm^{-1} to $q = 0.28$ nm^{-1}. The fit of the structure factor results in a volume fraction of $\phi = 19.1$ vol.% ± 0.9 vol.%, a particle charge of $z_p = 44.5\,e^- \pm 2.2\,e^-$, a concentration of a screening material of $c_s = 10.0\,\mu$M $\pm 3.9\,\mu$M, and a permittivity of $\epsilon = 80.85\,\epsilon_0 \pm 1.23\,\epsilon_0$. The constant ϵ_0 is the vacuum permittivity. The expected volume fraction of $\phi = 18.28\,\%$ ($c = 34$ wt.%) agrees to the volume fraction resulting from the fit. The measured colloids were dispersed in distilled water. The fit of the structure factor leads
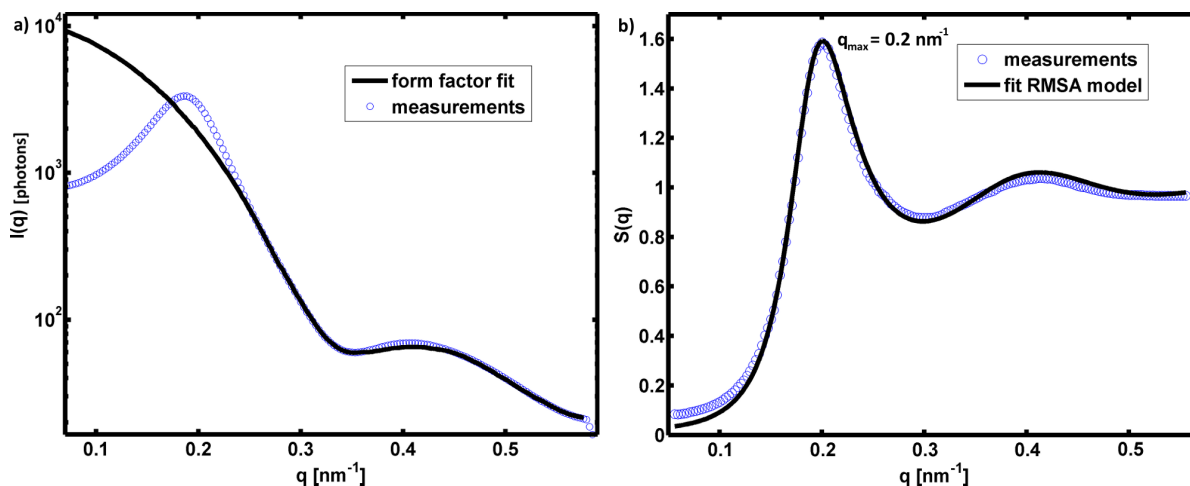
Figure 4.10: a) Integrated intensity $I(q)$ from figure 4.9. Furthermore, the fit of the form factor is shown. b) Resulting structure factor with a fit of the RMSA model.

to a concentration of a screening material of $c_s = 10.0\,\mu\text{M} \pm 3.9\,\mu\text{M}$. Typically, the screening of the potential of charged particles is described with the present of salt in the dispersion. However, in this case this value is treated as a fit parameter only which do not influence the fit of the RMSA-model significantly. With the fit results of the structure factor the viscosity $\eta = 1.48\,\text{mPa} \cdot \text{s}$ can be estimated, see equations 4.12, 4.13, and 2.36.

4.2.3 Liquid jet measurements

Typical SAXS patterns taken on the liquid jet are shown in figure 4.11. The flow direction of the jet is along the negative jet_z-direction, the tip of the nozzle is at $\text{jet}_z = 0$. The pattern taken at the jet center is isotropic, while the patterns taken at the jet sides are anisotropic. The shape of the pattern on the left and right side of the jet are mirror images of each other. Because of the anisotropic shape of the measured SAXS patterns the structure factor was determined segment-wise. This was done in three steps, see figure 4.12. First, the SAXS patterns were integrated in azimuthal segments of $\Delta\alpha = 5°$ (figure 4.12 a)). Then $S(q)$ was obtained by dividing the form factor (figure 4.12 b)). After this step a Gaussian function was fitted to the first peak of the structure factor. The maximum of this Gaussian function was used to locate the first maximum of the structure factor $S(q_{max})$.

In figures 4.13 and 4.14 four structure factors extracted from patterns recorded at different jet_x and jet_z values are depicted. The structure factors measured at the jet sides ($\text{jet}_x = 12\,\mu\text{m}, \text{jet}_x = 82\,\mu\text{m}$) at $\text{jet}_z = -100\,\mu\text{m}$ show a variation of the height and of the location of the first structure factor peak. Moreover, the structure factors are not azimuthally
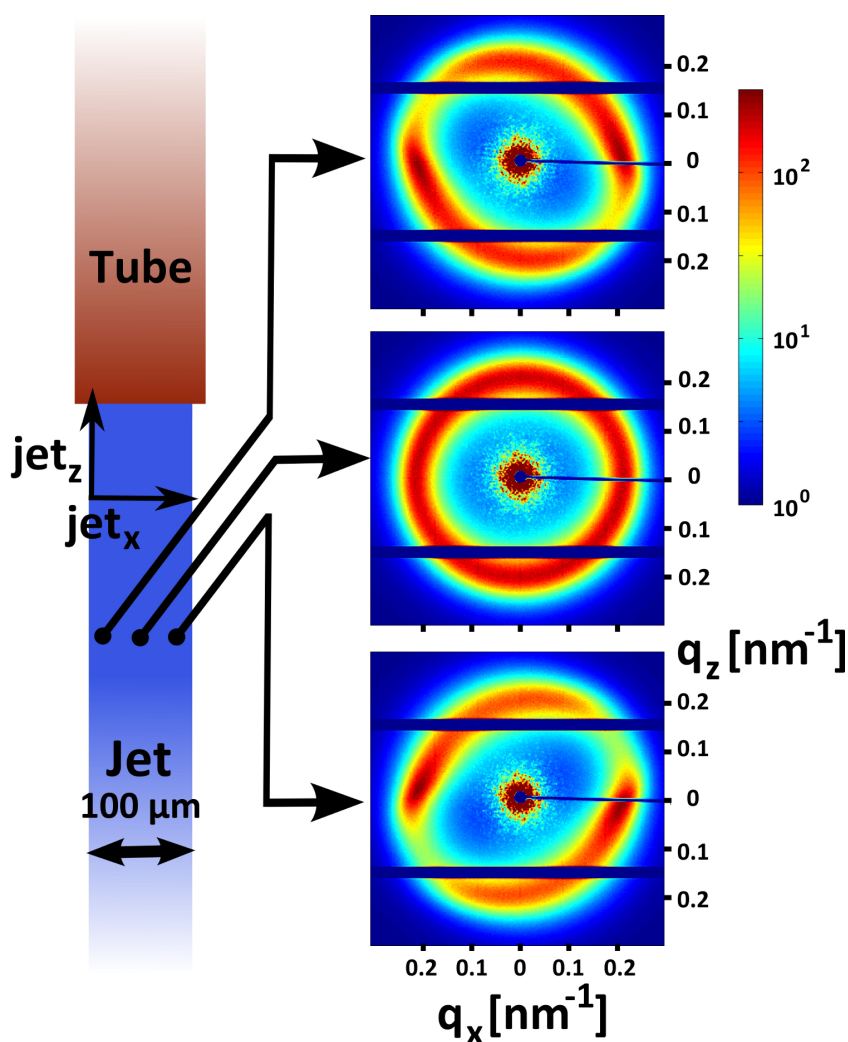
Figure 4.11: Typical SAXS patterns taken on the liquid jet with an exposure time of $t_e = 0.5\,\mathrm{s}$. The shadows on the SAXS pattern originate from the insensitive areas of the detector. The intensity scale represents the measured photons.

symmetric. The structure factor measured at the jet center (jet$_x = 47\,\mu\mathrm{m}$, figure 4.13 b)) is isotropic and its shape is comparable to the structure factor of the non-flowing sample, compare figure 4.10 b). At jet$_x = 47\,\mu\mathrm{m}$ and jet$_z = -3000\,\mu\mathrm{m}$ (figure 4.14) the structure factor is isotropic similar to the measurement in the jet center at jet$_z = -100\,\mu\mathrm{m}$. This isotropy of the structure factor indicates a homogenous structure of the silica particles similar to the non-flowing sample system in the capillary. In contrast, the anisotropic $S(q)$ indicates a inhomogeneous particle structure in the liquid jet. In order to illustrate the anisotropy of the structure factors in figure 4.13 a) and c) compared to the symmetric shape in figure 4.13 b) their maximums position q_{max} are shown in figure 4.15 a). The deviation from the q_{max} of the non-flowing sample is considerable. The peak position measured in the liquid jet differs from
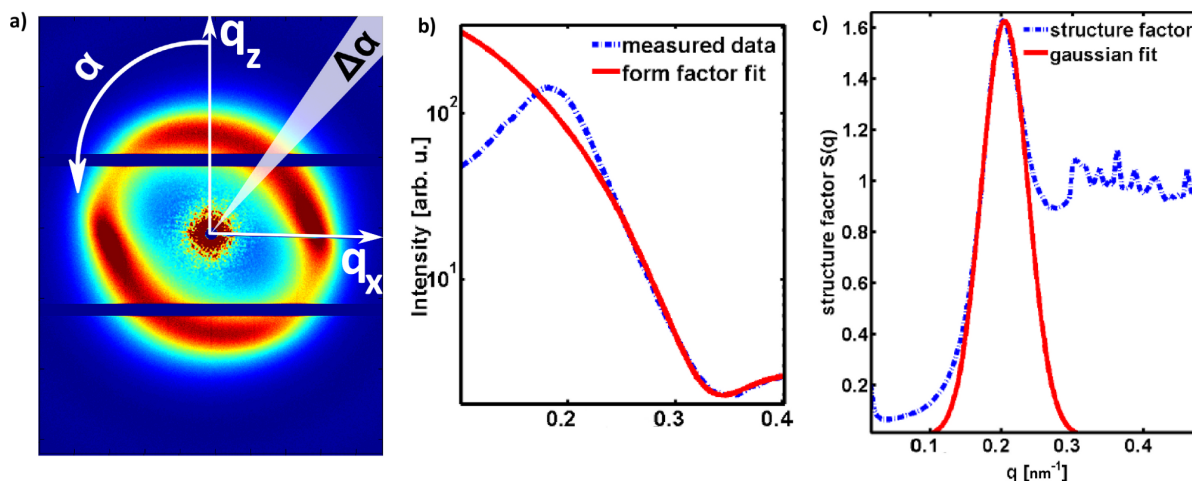
Figure 4.12: Schematic overview over the data treatment to determinate the position and the height of the first peak of the structure factor.

$q = 0.2\,\mathrm{nm}^{-1}$. The difference is pronounced at the jet sides ($\mathrm{jet}_x = 12\,\mu\mathrm{m}, 82\,\mu\mathrm{m}$). There, the position of the structure factor peak is shifted to values up to $q_{max} = 0.231\,\mathrm{nm}^{-1}$ and down to $q_{max} = 0.192\,\mathrm{nm}^{-1}$. This indicates a compression and an expansion of the particle structure in the jet compared the particle structure measured in the capillary. The compression is more pronounced than the expansion, which indicates a net compression of the colloidal dispersion.

The position of the structure factor peak q_{max} measured at the jet center ($\mathrm{jet}_x = 47\,\mu\mathrm{m}$) varies from $q_{max} = 0.202\,\mathrm{nm}^{-1}$ and $q_{max} = 0.198\,\mathrm{nm}^{-1}$. This indicates a less compressed and expanded sample structure compared to the structure measured at the jet sides.

Figure 4.15 b) shows the deviation $\Delta q/q$ of the structure factor peak relative to the q_{max} position in the unsheared case (capillary) at the two sides of the jet. The compression and expansion of the particle structure in the liquid jet is pronounced at the jet sides ($\mathrm{jet}_x = 12\,\mu\mathrm{m}$ and $\mathrm{jet}_x = 82\,\mu\mathrm{m}$). At these positions the compression relative to $q = 0.2\,\mathrm{nm}^{-1}$ is 15 % and the expansion is 8 %.

To visualize the effect a computational model was used, see figure 4.16. Particles were simulated as dots in a computational box (1000 × 1000 pixels) to describe a real space arrangement of spherical particles. In figure 4.16 a) 1800 particles were randomly set. The minimum distance between two particles was restricted to 20 pixels to model a homogenous distribution. In figure 4.16 b) this particle arrangement was compressed and expanded in two different directions. Parallel to the pixel_y-axis a compression was simulated by adding a $\Delta\mathrm{pixel}_y$ to the pixel_y coordinate of each pixel. As a first approach this was done with the Gaussian function
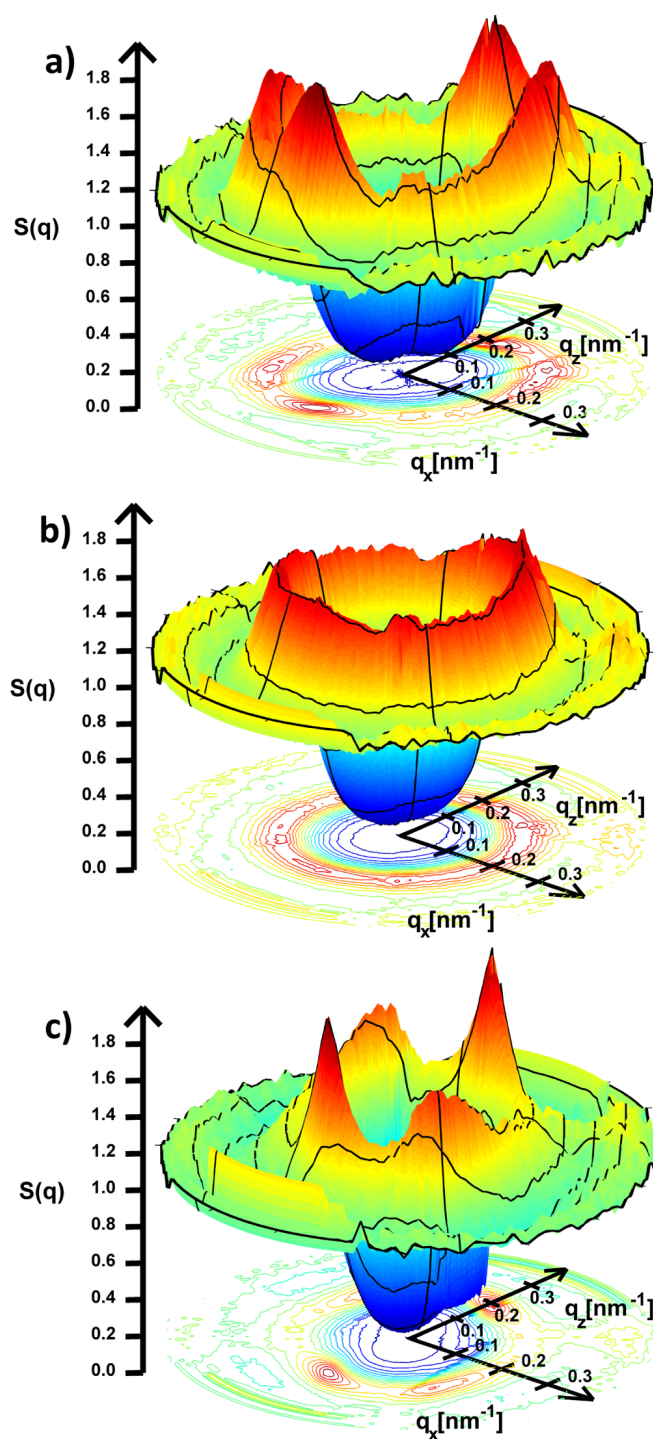
Figure 4.13: The structure factors at different jet positions. a) $jet_x = 12\,\mu m, jet_z = -100\,\mu m$; b) $jet_x = 47\,\mu m, jet_z = -100\,\mu m$; c) $jet_x = 82\,\mu m, jet_z = -100\,\mu m$.
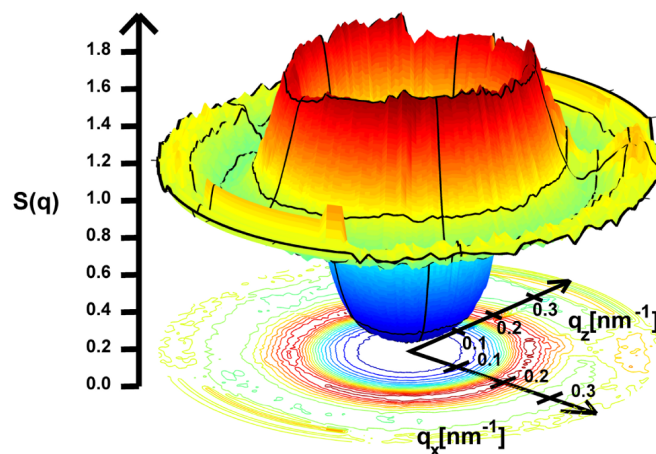
Figure 4.14: Structure factor measured at $jet_x = 47\,\mu m$ (middle), $jet_z = -3000\,\mu m$.
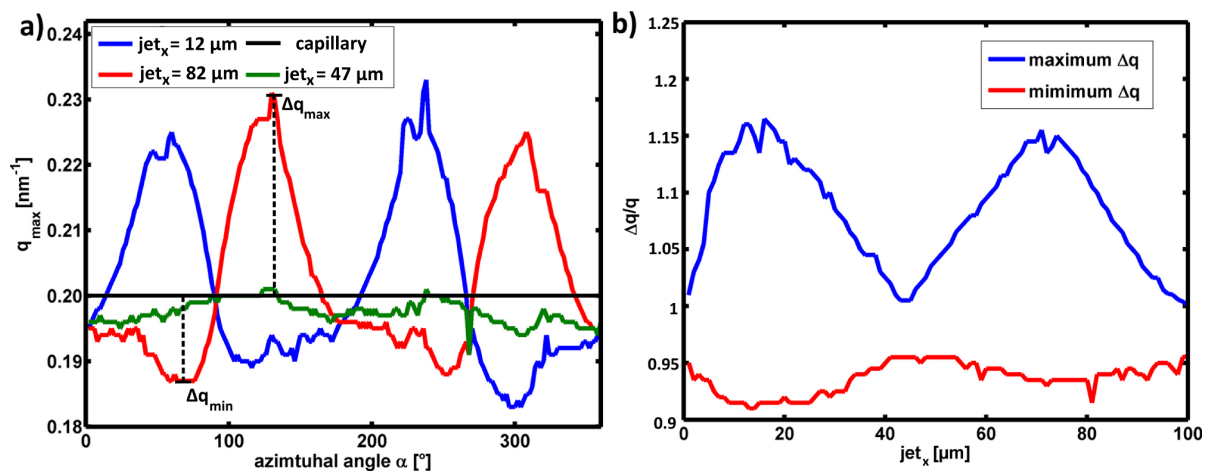
Figure 4.15: a) The position of the maximum of the structure factors $S(q_{max})$ as function of the azimuthal angle α at $jet_z = -100\,\mu m$ and three jet_x values. b) relative $\Delta q/q$ direction from the isotropic case as function of jet_x at $jet_z = -100\,\mu m$.
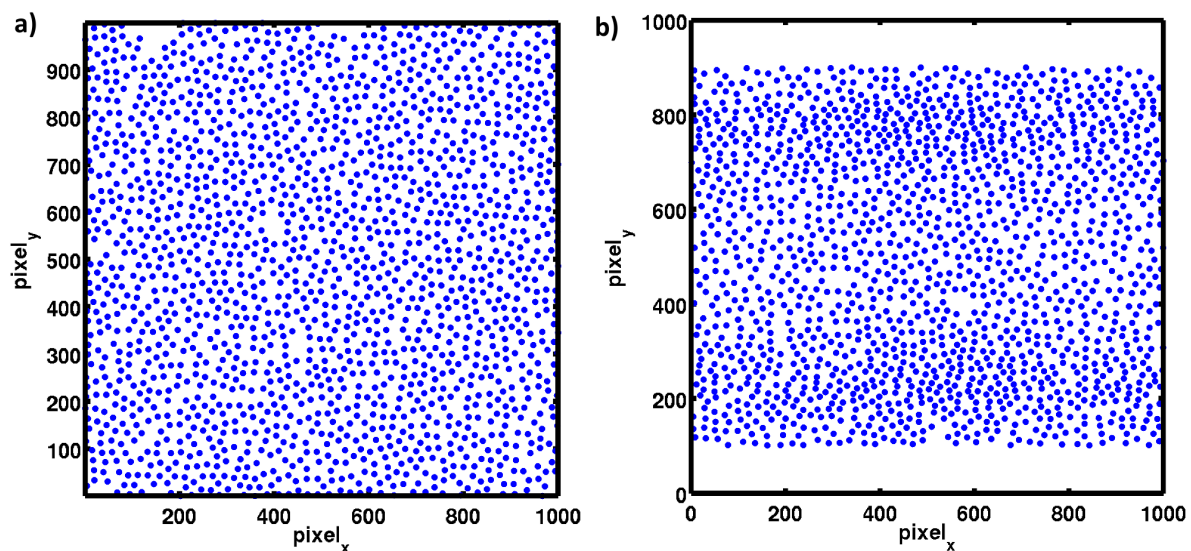
Figure 4.16: Computational model of samples in a box of 1000 × 1000 pixels. a) Homogenous distribution of particles (blue dots) with a minimal distance of 20 pixels to each other. b) Modified model sample. The sample is compressed parallel to pixel$_y$-axis and expanded parallel to pixel$_x$-axis.
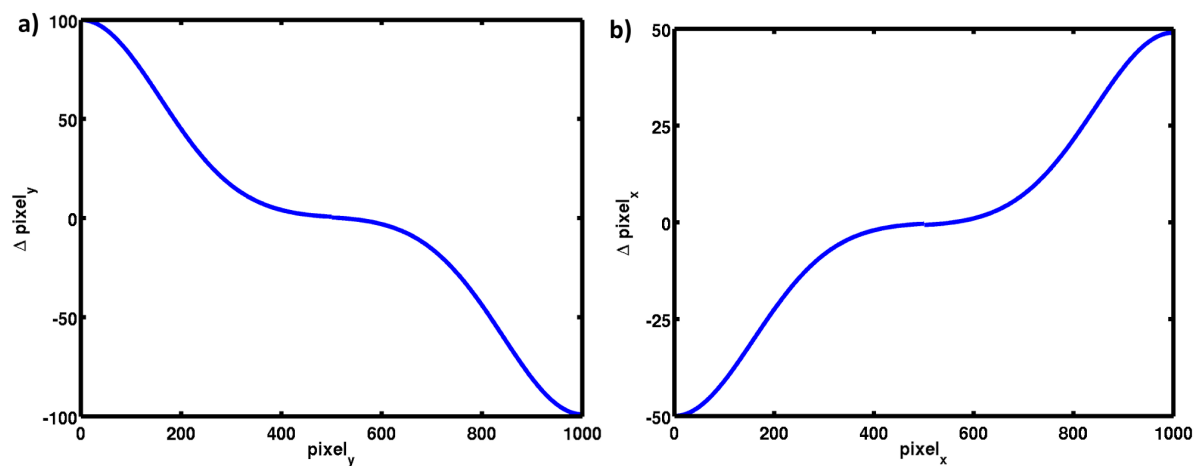
Figure 4.17: Illustration of the modification of the computational model. a) Compression of particle structure. b) Expansion of particle structure.
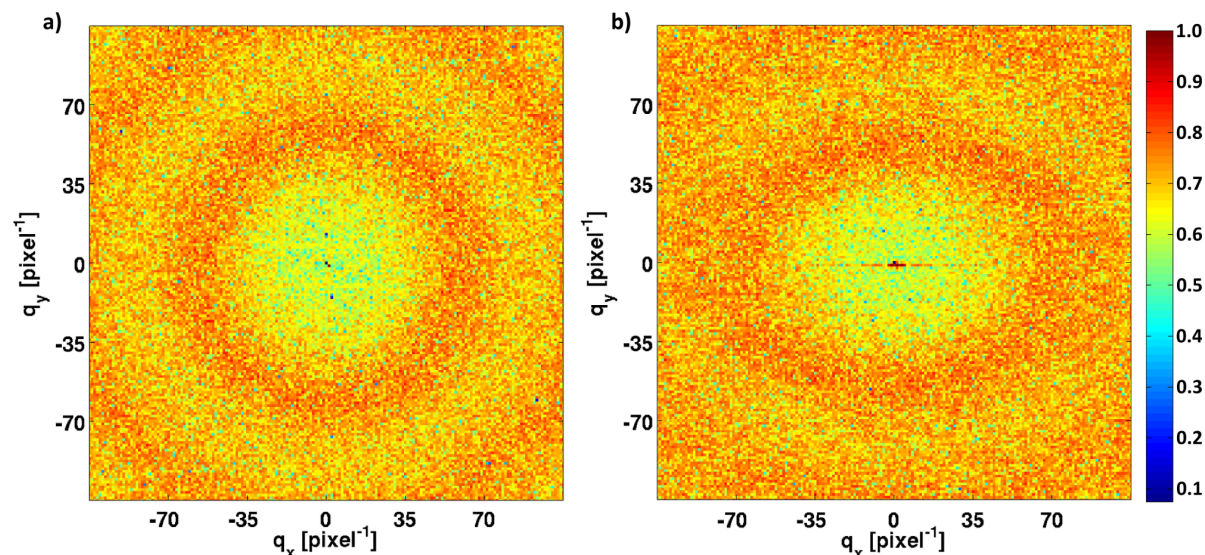
Figure 4.18: Fourier transform of computational model. a) Homogenous particle structure (figure 4.16 a)). b) Modified particle structure (figure 4.16 b)).

(figure 4.17 a))

$$\Delta\text{pixel}_y = \begin{cases} 100 \cdot \exp\left[-\frac{1}{50000} \cdot \text{pixel}_y^2\right], & \text{if pixel}_y \leq 500 \\ -100 \cdot \exp\left[-\frac{1}{50000} \cdot \left(\text{if pixel}_y - 1000\right)^2\right], & \text{if pixel}_y > 500 \end{cases} \quad (4.15)$$

In this way the pixels are shifted to the center of the computational box (pixel$_y = 500$). The opposite procedure was done with the pixel$_x$ component

$$\Delta\text{pixel}_x = \begin{cases} -50 \cdot \exp\left[-\frac{1}{50000} \cdot \text{pixel}_x^2\right], & \text{if pixel}_x \leq 500 \\ 50 \cdot \exp\left[-\frac{1}{50000} \cdot \left(\text{pixel}_x - 1000\right)^2\right], & \text{if pixel}_x > 500 \end{cases} \quad (4.16)$$

The particles are expanded away from the center (pixel$_x = 500$) of the computational box, see figure 4.17 b). The particles that are shifted outside of the computational box were ignored in the following calculation. With this method a sample compression parallel to the pixel$_y$-axis and an expansion parallel to the pixel$_x$-axis was simulated. To extract the structure factors of these model samples a Fourier transform was applied, see figure 4.18. The structure factor extracted from the homogenous particle distribution (figure 4.16 a)) is isotropic, while the structure factor obtained from modified model sample (figure 4.16 b)) is anisotropic. Thus, one might explain the measured anisotropic structure factors with a compression and an expansion of a particle structure. However, the fluctuations of the height of the structure factor (figure 4.13) are not described by this simple model.

4.2.4 Conclusion and discussion

SAXS experiments on silica colloids dispersed in water were performed to study the influence of the flow properties of a Rayleigh nozzle on the particle structure of a colloidal dispersion. The sample was characterized by fits of the form factor and the structure factor. It is assumed that only variations of the inter particle correlations in the dispersion can influence the scattering patterns measured on the liquid jet. The presented computational model illustrates the effect of compression and expansion of an isotropic particle arrangement. This model can explain the change of the position of the first peak of the structure factor in figure 4.13. However, it considers only a two dimensional particle arrangement and thus it can only be a limited description of the particle arrangement in the jet. Simulations of colloidal dispersion under shear predict compressions and expansions of a particle structure in shear flows, see figure 4.6. Recently, a combined rheology and SAXS study connected a structural transitions of silica colloidal dispersion with high shear rates.[33] The authors measured anisotropic structure factors for different shear strains and postulated a structural transition from a homogenous particle distribution to a anisotropic particle distribution under shear. The azimuthal variation of the height of the structure factor indicates an azimuthal variation of the particle correlations in the liquid jet, see figure 4.13. Whether or not this is indicative of a phase transition[35] or connected to the formation of flocculate systems or hydroclusters is presently unclear. At pronounced shear flows and high particle concentrations the presence of particle cluster are known, see figure 4.5.[34] One might speculate that the measured structure factors are indications of particle compounds formed due to a structural transition from a homogenous particle distribution to a anisotropic particle distribution under shear.

4.3 Spindle-shaped particles

In this section the SAXS experiment on a diluted dispersion of hematite particles in a water jet is presented. The experiment were performed at beamline P10 at PETRA III using a GDVN. The hematite particles were synthesized as explained in section 4.3.1. The production of GDVNs is explained in appendix A.1. For characterization of the particles SAXS patterns of a non-flowing dispersion were taken and transmission electron microscopy (TEM)[35] images were taken. In the following sections the experimental setup, the data treatment and the

---

[33]Denisov, D. et al. *Sci. Rep.* **3**, (2013), 1631.

[34]Brown, E. et al. *Nature Mat.* **9**, (2010), 220; Wagner, N.J. et al. *Physics Today* **62**, (2009), 27; Cheng, X. et al. *Science* **333**, (2011), 1276.

[35]Private communication: Annemarie Nack, Universität Rostock, Elektronenmikroskopiezentrum (EMZ).

results of this experiment are discussed.

4.3.1 Liquid jet setup and sample preparation

The SAXS experiment carried out at beamline P10 at PETRA III was performed with a sample-detector distance of $d = 5\,\text{m}$ using a Pilatus 300K detector. In this experiment spindle-shaped colloidal hematite particles dispersed in water were used. To characterize the dispersion and to record a reference signal of the particles, SAXS patterns were taken with the standard SAXS chamber of beamline P10. This chamber allows measurements of samples in a capillary located in a magnetic field.[36] Since the particles are sensitive to magnetic fields, they were aligned with the short semi-axis parallel to a magnetic field with $\left|\vec{B}\right| \approx 900\,\text{mT}$. This allows a fit of the form factor of spindle-shaped particles to the data for the characterization of the particles, see section 2.2.2.[37] The diameters of the liquid jet was between $d_{\text{jet}} = 12\,\mu\text{m}$ and $d_{\text{jet}} = 25\,\mu\text{m}$.[38] The x-ray beam was focused to $2\,\mu\text{m}$ x $3\,\mu\text{m}$ at an x-ray energy of $E_{\text{x-ray}} = 7\,\text{keV}$. SAXS patterns were taken along the jet at distances between $100\,\mu\text{m}$ and $3000\,\mu\text{m}$ from the nozzle tip. Across the jet SAXS patterns were recorded in steps of $1\,\mu\text{m}$. The exposure time was $t_e = 0.5\,\text{s}$. At every position on the jet 300 SAXS patterns were measured.

- **Liquid jet setup**

  For the liquid jet environment a vacuum chamber was designed. An overview of the liquid jet setup is shown in figure 4.19 a). The chamber was pumped by a roughing pump[39] and by a turbo pump[40]. The pressure reaches values without liquid jet down to $p_{\text{vac}} = 10^{-6}\,\text{mbar}$ and with the jet down to $p_{\text{vac}} = 10^{-3}\,\text{mbar}$. The nozzle was mounted at a nozzle holder that was moveable by a manipulator. The calibration of the liquid jet to the x-ray beam was carried out using an in-line microscope, see 4.19 b). This microscope allows a view on the optical axis of the x-ray beam via a mirror. The mirror has a hole of $2\,\text{mm}$ diameter that allows the x-ray beam to pass. For calibration of the liquid jet to the x-ray beam via the microscope a screen made of yttrium aluminium garnet (YAG) is mounted on the nozzle holder. It is used to visualize the x-beam for the microscope. After the determination of the x-ray beam location the jet is moved by the manipulator to this spot. In figure 4.20 a) an image of the liquid jet taken with this microscope is shown. To reduce background scattering originating from air scattering

[36]Conrad, Heiko. "Dynamics of colloids in molecular glass forming liquids studied via X-ray photon correlation spectroscopy." Dissertation. Universität Hamburg, 2014.

[37]Märkert, C. et al. *J. App. Cryst.* **44**, (2011), 441.

[38]The measurement of the jet diameter is explained in section 4.3.2.

[39]Edwards, XJR35i.

[40]Pfeiffer Gmbh, HighPace 300.
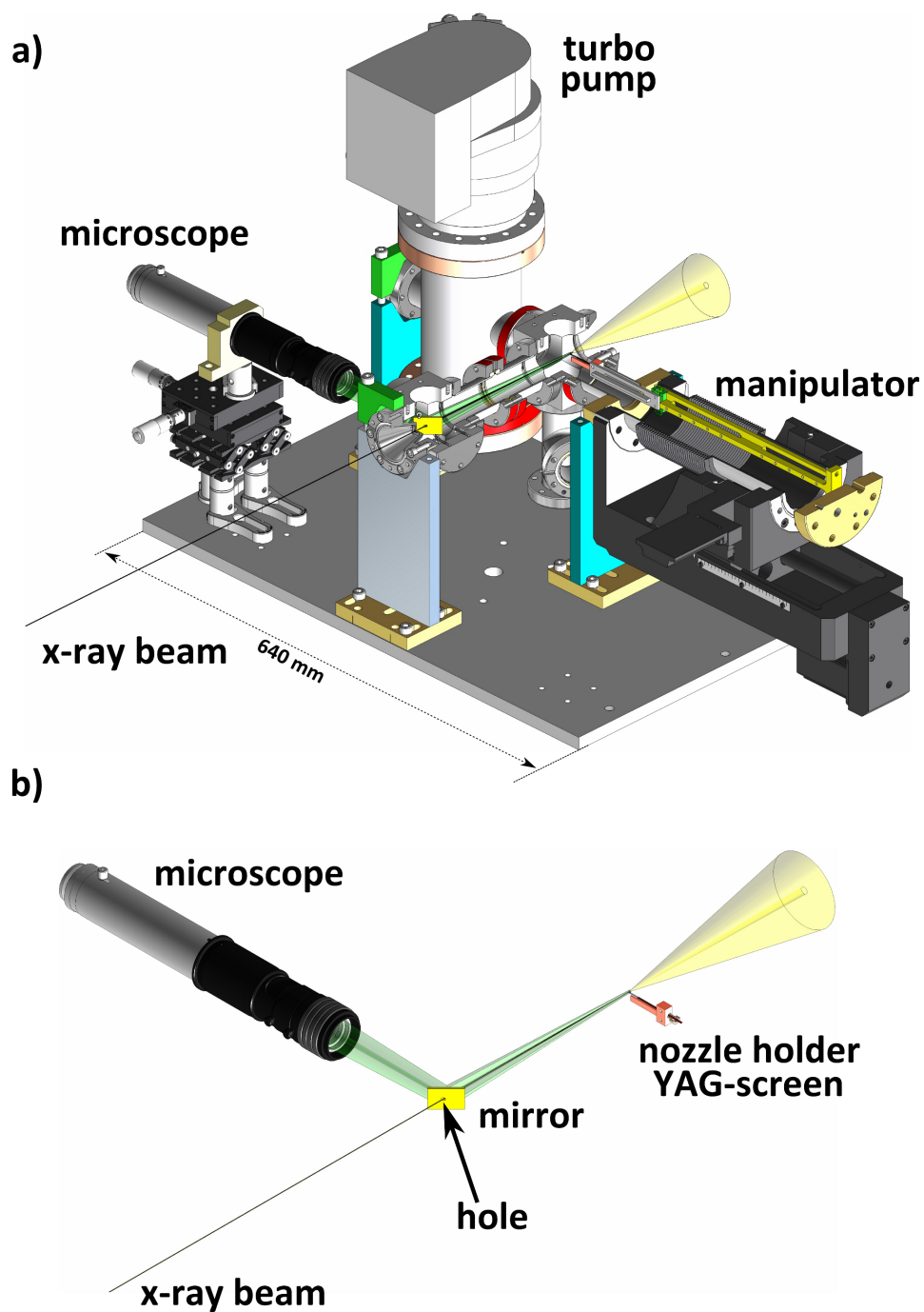
Figure 4.19: Two sketches of the liquid jet setup used in the experiment. a) Schematic overview of the liquid jet setup. Besides manipulator and vacuum pump mechanical components are shown. b) Schematic drawing of the geometry of the x-ray beam, the nozzle, and the in-line microscope.
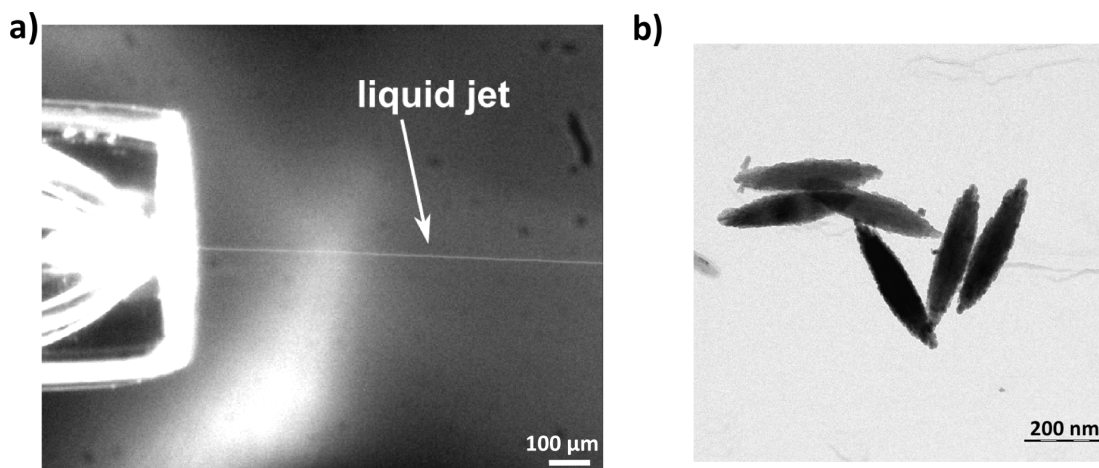
Figure 4.20: a) Microscope image taken with the in-line microscope. The Image show the liquid jet in the sample chamber. b) TEM image of the hematite particles used in the experiment.

the vacuum chamber was flanged to the flight paths of the beamline. The chamber was separated from the vacuum in the flight paths by silicon nitride windows of $5\,\mu m$ thickness.

- **Sample preparation**
  A synthese of hematite particles was suggested by Ozaki et al.[41] An aqueous solution of iron(III) chloride with a concentration of $(\alpha$ - $FeCl_3) = 0.02\,mol/l$, containing $4\,ml$ of a $3.5 \cdot 10^{-4}\,mol/l$ solution of sodium dihydrogen phosphate, was refluxed for $48\,h$. The dispersion was centrifuged several times and redispered in distilled water in order to remove remaining ions. In figure 4.20 b) a transmission electron microscopy image of the particles is shown. The particles exhibit a spindle-like shape. The volume fraction in the dispersion was $\phi = 0.1\,vol.\%$.

4.3.2 Sample characterization

For characterizing the hematite spindles were aligned by putting the suspension ($\phi = 0.1\,vol.\%$) in a magnetic field ($B \cong 900\,mT$). A total of 100 patterns with an exposure time of $t_e = 0.5\,s$ were recorded. These patterns were corrected for background scattering by subtracting a pattern without the sample. After this the patterns have been averaged, see figure 4.21 a). The $\vec{B}$-field was aligned in the $g_x - g_z$ plane with an angle of $\theta_g = -\frac{\pi}{4}$ at $\phi_g = 0$ as can be seen in figure 4.22 a). Since the minor axis of the spindle shaped particles is known[42] to align parallel to the field direction the major axis of the spindles (characterized by the orientation

---

[41]Ozaki, M. et al. *J. Colloid Interf. Sci.* **102**, (1984), 146.
[42]Märkert, C. et al. *J. App. Cryst.* **44**, (2011), 441.

vector $\vec{g}$) points perpendicular to the $\vec{B}$-field with an angle $\theta_g = \frac{\pi}{4}$ (for $\phi_g = 0$. This explains
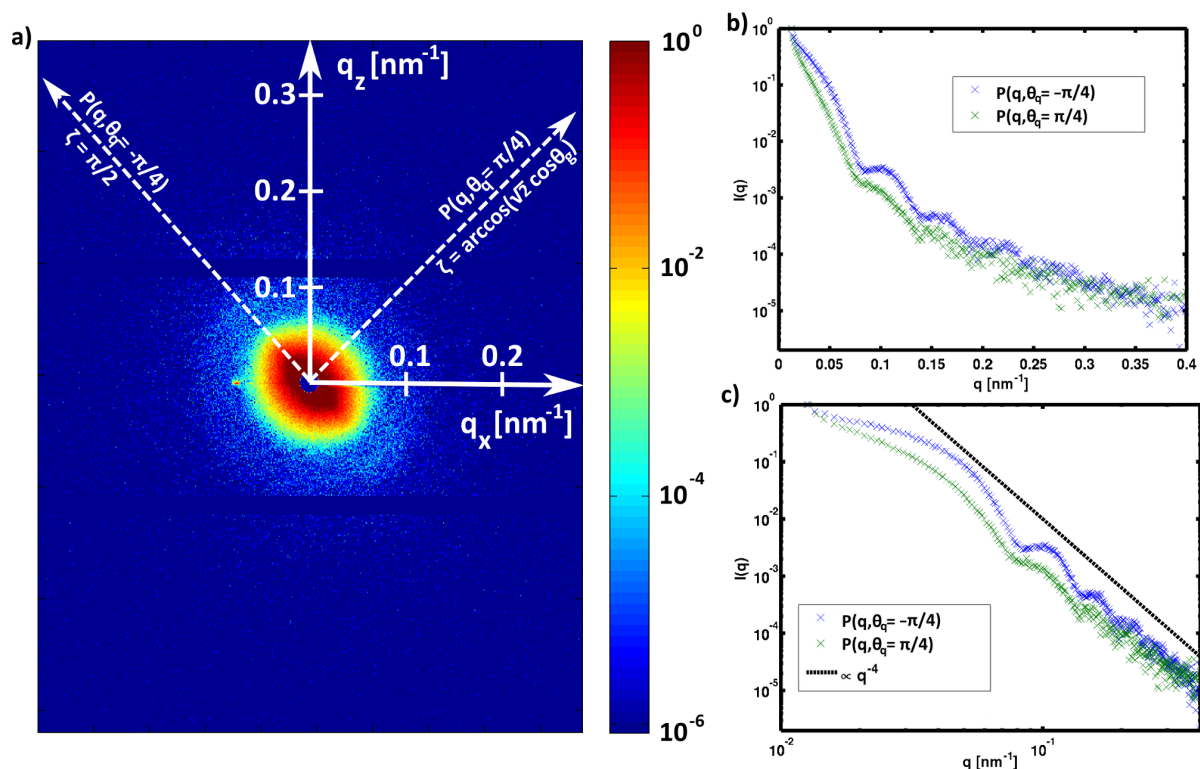
Figure 4.21: a) Averaged SAXS pattern of aligned spindle-shaped hematite particles. The intensity
scale is normalized to its maximum. Line profiles of the SAXS pattern are shown in b)
and c).

why the SAXS pattern in figure 4.21 a) is elongated along the $\vec{B}$ direction and narrows in
the orthogonal direction. Figure 4.21 b) and c) shows $\Delta\alpha = 20°$ azimuthal averages about
the $\theta_q = -\frac{\pi}{4}$ direction (blue symbols) and about the $\theta_q = \frac{\pi}{4}$ direction (green symbols),
representing the form factor along the minor and major axis of the spindles, respectively.
The data in Figure 4.21 b) and c) show that the formfactors in both directions have the same
periodicity and fall off with the same power law. The data along $\theta_q = \frac{\pi}{4}$ are however weaker
and less modulated which indicates a fundamental difference between the two directions.
This is in fact the result of the orientational averaging process as indicated in figure 4.22 b).
The alignment of the short spindle axis parallel to $\vec{B}$ allows for any orientation of $\vec{g}$ that is
perpendicular to $\vec{B}$ as shown in the figure. This implies that the intensity profile along $\theta_q = \frac{\pi}{4}$
is actually an average over the formfactors that correspond to the various spindle orientations.
The condition $\vec{B} \cdot \vec{g} = 0$ implies
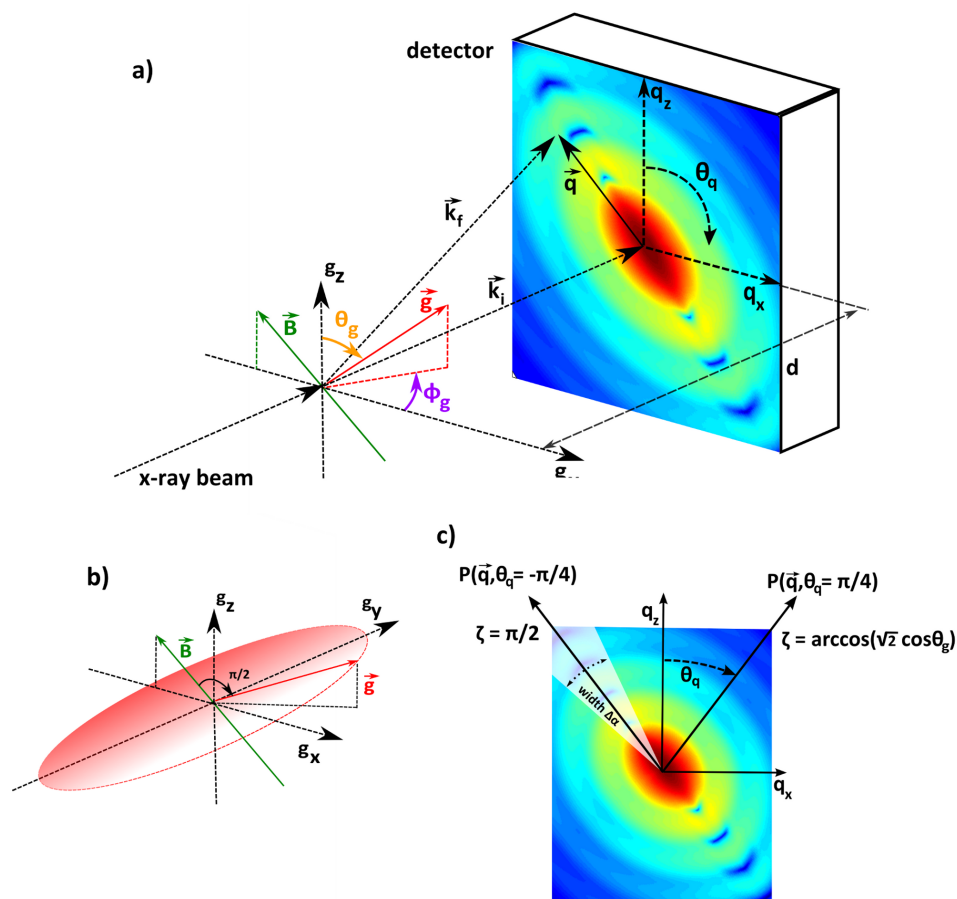
Figure 4.22: a) Sketch of the scattering experiment with aligned spindle shaped-particles. The coordinates $\vec{g}(\theta_g, \phi_g)$ and the coordinates $\vec{q}(q_x, q_z)$ are shown. b) Sketch of the particle vector $\vec{g}$ and the magnetic field $\vec{B}$. c) Sketch to illustrate the evaluation of the form factor out of the scattering pattern.

$$\vec{B} \cdot \vec{g} = \begin{pmatrix} \sin\left(-\frac{\pi}{4}\right) \\ 0 \\ \cos\left(-\frac{\pi}{4}\right) \end{pmatrix} \cdot \begin{pmatrix} \sin\theta_g \cos\phi_g \\ \sin\theta_g \sin\phi_g \\ \cos\theta_g \end{pmatrix} = 0 \qquad \Rightarrow \qquad \cos\phi_g = \frac{\cos\theta_g}{\sin\theta_g}. \qquad (4.17)$$

Inserting 4.17 into equation 2.20 the angle enclosed by the particle orientation vector $\vec{g}$ and the wavevector $\vec{q}$ reduces to

$$\cos\zeta = \cos\theta_q \cos\theta_g + \sin\theta_q \cos\theta_g. \qquad (4.18)$$

For $\theta_q = \frac{\pi}{4}$ equation 4.18 reduces to $\zeta = \arccos(\sqrt{2}\cos(\theta_g))$. The scattering pattern is thus given by the average over the (different) formfactors of individual spindles oriented randomly with their major axis in the plane perpendicular to $\vec{B}$ (as indicated in Figure 4.22 b) and c)). For $\theta_q = -\frac{\pi}{4}$ the angle ζ equals $\frac{\pi}{2}$ and the scattering pattern along $\theta_q = \frac{\pi}{4}$ is given by the average over the (identical) formfactors of individual spindles oriented randomly with their major axis in the plane perpendicular to $\vec{B}$. The geometrical alignment sketched in Figure 4.22 b) can be expressed by an ODF which can be written with the help of equation 4.17 as

$$f(\theta_g, \phi_g) = \delta\left(\cos\phi_g - \frac{\cos\theta_g}{\sin\theta_g}\right). \qquad (4.19)$$

With this ODF and equation 4.18 one can express equation 2.21 as

$$P_{\text{dist}}(q, \theta_q, R_1, R_2, Z, \nu) = \int_0^{2\pi} \int_0^{\pi} \delta\left(\cos\phi_g - \frac{\cos\theta_g}{\sin\theta_g}\right)$$
$$P_{\text{poly}}(q, \cos\theta_q \cos\theta_g + \sin\theta_q \cos\theta_g, R_1, R_2, Z, \nu)\sin\theta_g d\theta_g d\phi_g. \qquad (4.20)$$

Equation 4.20 was used to model any slice from the 2D formfactor of figure 4.21 a). For $\theta_q = -\frac{\pi}{4}$ and $\zeta = \frac{\pi}{2}$ this becomes particularly simple since one can use equation 2.16 instead of equation 4.20. Figure 4.23 a) and b) shows fits (red solid lines) of equation 2.16 to $\Delta\alpha = 20°$ azimuthal averages of the data about the $\theta_q = -\frac{\pi}{4}$ direction (blue symbols) and about the $\theta_q = \frac{\pi}{4}$ direction (green symbols). The fit range was $q = 0.06\,\text{nm}^{-1}$ to $q = 0.17\,\text{nm}^{-1}$. The results yield $R_1 = 54.32\,\text{nm} \pm 3.21\,\text{nm}$, an aspect ratio $\nu = 3.21 \pm 0.24$ and a polydispersity $p = 9.2\% \pm 2.3\%$ as listed in table 4.1. The scattering signal along $P(q, \theta_q = \frac{\pi}{4})$ (green symbols) is compared to the form factor model (red dashed line) using the fit results. The agreement of these curves shows the validity of the form factor model.

In order to verify whether or not the range of azimuthal averaging has an influence on the
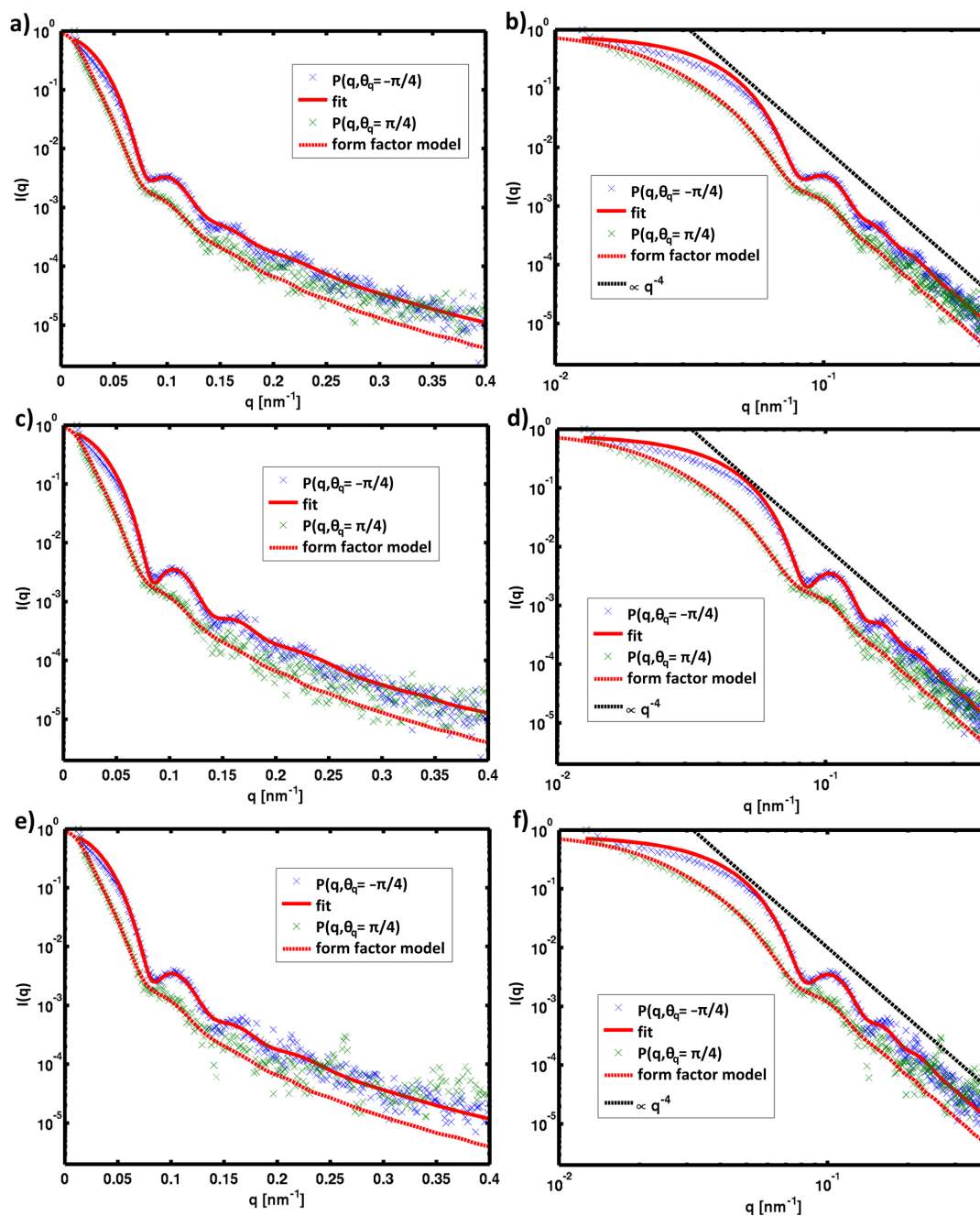
Figure 4.23: Intensity of spindle-shaped particles aligned in the magnetic field ($\theta_q = -\frac{\pi}{4}$, blue crosses and $\theta_q = \frac{\pi}{4}$, green crosses) as a function of the wave vector transfer q. The red line represents a fit with equation 2.16 and $\zeta = \frac{\pi}{2}$ to the intensity along $\theta_q = -\frac{\pi}{4}$ (blue crosses). The fit results were used to calculate the form factor along $\theta_q = \frac{\pi}{4}$ (dashed red line). The results are depicted in a semi-logarithmic plot (a), c), and e)) and in a double-logarithmic plot(b), c), and f)). In the double-logarithmic plots an power law $\propto q^{-4}$ is plotted. The plots a) and b) show the result of $\Delta\alpha = 20°$, c) and d) of $\Delta\alpha = 10°$, and e) and f) of $\Delta\alpha = 5°$.
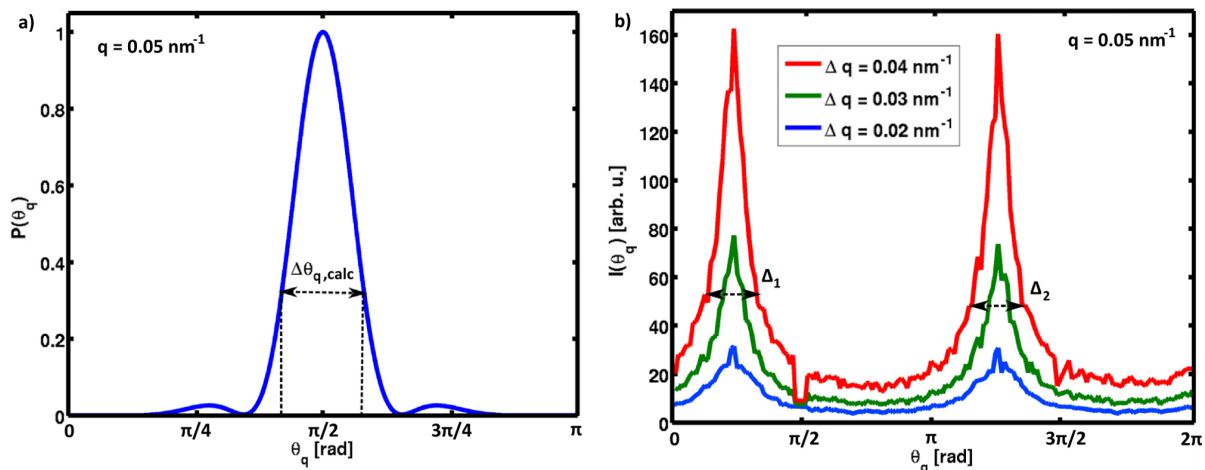
Figure 4.24: Azimuthal profiles at $q = 0.05\,\mathrm{nm}^{-1}$. a) Calculated form factor as function of θ_q with $R_1 = 54.32\,\mathrm{nm}$, $\nu = 3.33$, and $p = 0.092$. The full width at half maximum is $\Delta\theta_{q,\mathrm{calc}} = 0.59\,\mathrm{rad}$. b) Measured form factor as function of θ_q for different Δq. The azimuthal widths are listed in table 4.2 and 4.3.

results a similar modelling was also carried out for narrower ranges, namely $\Delta\alpha = 10°$ and $\Delta\alpha = 5°$. The results of these fits are shown in figure 4.23 b) and d) and figure 4.23 e) and f), respectively. The results are also listed in table 4.1 and show that the differences are negligible. Figures 4.23 b),d),f) also show that the intensity falls proportional to q^{-4} as expected for an orientational average of spindle-shaped particles. For further treatment the fit result with an azimuthal integration range of $\Delta\alpha = 5°$ was used.

$\Delta\alpha$	$R_1[\mathrm{nm}]$	ν	p
20°	56 ± 3	3.3 ± 0.2	0.10 ± 0.02
10°	54 ± 3	3.3 ± 0.2	0.09 ± 0.02
5°	54 ± 4	3.3 ± 0.3	0.09 ± 0.03

Table 4.1: Result of form factor fit shown in figure 4.23.

In order to determine the degree of alignment of the minor semi-axis parallel to the magnetic field the measured azimuthal width $\Delta\theta_q$ of the measured intensity data is compared to a calculated azimuthal width $\Delta\theta_{q,\mathrm{calc}}$ using equation 2.16. In case of a perfect alignment the measured azimuthal width $\Delta\theta_q$ is given by the model of a spindle-shaped particle showing a single orientation, see figures 2.8 and 2.15. A calculated azimuthal profile of the form factor at $q = 0.05\,\mathrm{nm}^{-1}$ is shown in figure 4.24 a). The calculation used $R_1 = 54.32\,\mathrm{nm}$, $\nu = 3.33$, and $p = 0.092$. In figure 4.24 b) azimuthal profiles of the SAXS pattern (figure 4.21 a)) at $q = 0.05\,\mathrm{nm}^{-1}$ are shown for three different Δq. To extract the azimuthal width the maxima

	$A[\text{arb. u.}]$	$\mu[\text{rad}]$	$\sigma_s[\text{rad}]$	$\Delta\theta_q[\text{rad}]$
$\Delta q = 0.04\,\text{nm}^{-1}$	155.7 ± 1.2	0.74 ± 0.01	0.26 ± 0.03	0.62 ± 0.07
$\Delta q = 0.03\,\text{nm}^{-1}$	71.7 ± 0.8	0.77 ± 0.01	0.26 ± 0.05	0.62 ± 0.14
$\Delta q = 0.02\,\text{nm}^{-1}$	23.3 ± 0.4	0.77 ± 0.01	0.27 ± 0.09	0.64 ± 0.22

Table 4.2: Fit results of fitted Gaussian function to maximum Δ_1 in figure 4.24 and azimuthal widths $\Delta\theta_q$.

	$A[\text{arb. u.}]$	$\mu[\text{rad}]$	$\sigma_s[\text{rad}]$	$\Delta\theta_q[\text{rad}]$
$\Delta q = 0.04\,\text{nm}^{-1}$	158.2 ± 1.8	3.89 ± 0.02	0.26 ± 0.03	0.61 ± 0.07
$\Delta q = 0.03\,\text{nm}^{-1}$	75.4 ± 0.9	3.92 ± 0.03	0.26 ± 0.06	0.62 ± 0.14
$\Delta q = 0.02\,\text{nm}^{-1}$	21.5 ± 0.3	3.92 ± 0.01	0.27 ± 0.08	0.65 ± 0.19

Table 4.3: Fit results of fitted Gaussian function to maximum Δ_2 in figure 4.24 and azimuthal widths $\Delta\theta_q$.

(Δ_1 and Δ_2) were fitted with an Gaussian function

$$f(\theta_q) = A \cdot \exp\left(\left[\theta_q - \mu\right]^2 / \sigma_s\right), \tag{4.21}$$

where A is the amplitude, μ the azimuthal location, and σ_s is the standard deviation. The azimuthal width $\Delta\theta_q$ equals the FWHM of the Gaussian function and is given by $\Delta\theta_q = 2 \cdot \sqrt{2 \cdot \ln(2)} \cdot \sigma_s$. The results of the fits to the maxima Δ_1 are shown in table 4.2 and to the maxima Δ_2 are shown in table 4.3. The obtained azimuthal widths $\Delta\theta_q$ from the two maxima are averaged $\Delta\theta_{q,\text{ave}}$. For $\Delta q = 0.04\,\text{nm}^{-1}$ the averaged azimuthal width is $\Delta\theta_{q,\text{ave}} = 0.62\,\text{rad} \pm 0.05\,\text{rad}$, which agrees within the error bar with the calculated azimuthal width $\Delta\theta_{q,\text{calc}} = 0.59\,\text{rad}$. This shows that the particles were perfect aligned.

4.3.3 Spindle-shaped particles in a liquid jet

The hematite spindle suspension was studied in the liquid jets system. The setup parameters were described in chapter 4.3.1. SAXS pattern were taken at distances between $100\,\mu\text{m}$ and $3000\,\mu\text{m}$ from the nozzle tip and at different spots within the jet. The single frame exposure time was $t_e = 0.5\,\text{s}$ and 300 frames were taken at each position. Since the hematite jet contaminated the windows of the setup background subtraction was absolutely crucial. The background pattern was substracted from each frame. Figure 4.25 a) shows such a background subtracted pattern taken $100\,\mu\text{m}$ from the nozzle. It has been generated using the raw data (figure 4.25 b)) and subtracting the background pattern (figure 4.25 c)). The anisotropic
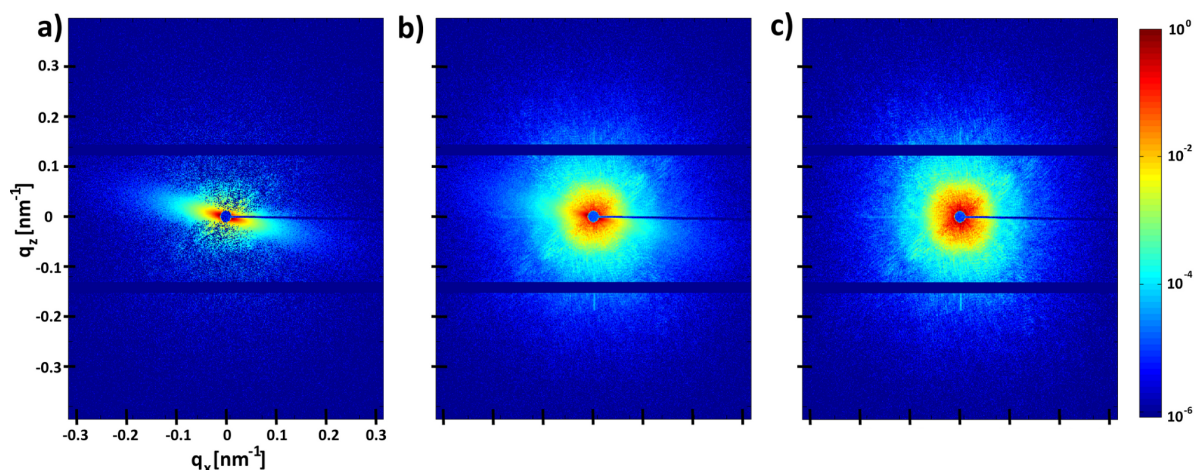
Figure 4.25: Three SAXS single patterns taken with an exposure time of $t_e = 0.5\,\text{s}$. a) Background corrected SAXS pattern. b) SAXS pattern without background correction. c) SAXS pattern taken without liquid jet (background). The intensity scale of each pattern is normalized to their maxima.

scattering pattern in figure 4.25 is characteristic for spindle-shaped particles. In the following the particle orientation and the azimuthal widths $\Delta\theta_q$ of the form factors measured in the jet are analyzed. The scattering patterns were recorded at different locations in the liquid jet. The coordinates of this experiment were introduced in figure 4.26. The flow direction of the liquid jet is parallel to the jet_x-axis while the gas flow of the GDVN presses coaxially on the liquid jet. The tip of the nozzle is located at $\text{jet}_x = 0\,\mu\text{m}$ and the jet center is located at $\text{jet}_z = 0\,\mu\text{m}$. SAXS patterns recorded at different positions in the liquid jet are shown in figure 4.27. Close to the nozzle tip the recorded SAXS pattern is anisotropic, see figure 4.27 a). Since the jet in this experiment was not exiting the nozzle horizontally but was rather down bent by about 20° (figure 4.27 a)) one observed a SAXS pattern that appears tilted by this bent angle. The fact that the SAXS pattern is elongated perpendicular to the flow direction jet_x indicates that the major axis of the spindles is aligned parallel to the flow direction jet_x. At larger distances from the nozzle ($\text{jet}_x > 100\,\mu\text{m}$) the SAXS patterns change dramatically.

As an example, the form factors measured across the liquid jet at $\text{jet}_x = 500\,\mu\text{m}$ are shown in figure 4.27 b), c), and d). At the jet center ($\text{jet}_z = 0\,\mu\text{m}$) the SAXS patterns indicate a particle alignment parallel to the jet_z-axis. Above and below the center ($\text{jet}_z = 8\,\mu\text{m}$, $\text{jet}_z = -8\,\mu\text{m}$) the SAXS patterns show an "X-shape" that implies particles with two different preferred particle alignments in the liquid jet.

The azimuthal widths of the scattering profiles were extracted at $q = 0.05\,\text{nm}^{-1}$, see figure 4.28. The plots in figure 4.28 a), b) are extracted from the SAXS pattern shown in figure 4.27 b), c), respectively. In figure 4.27 c) four maxima are present caused by the "X-shape" of
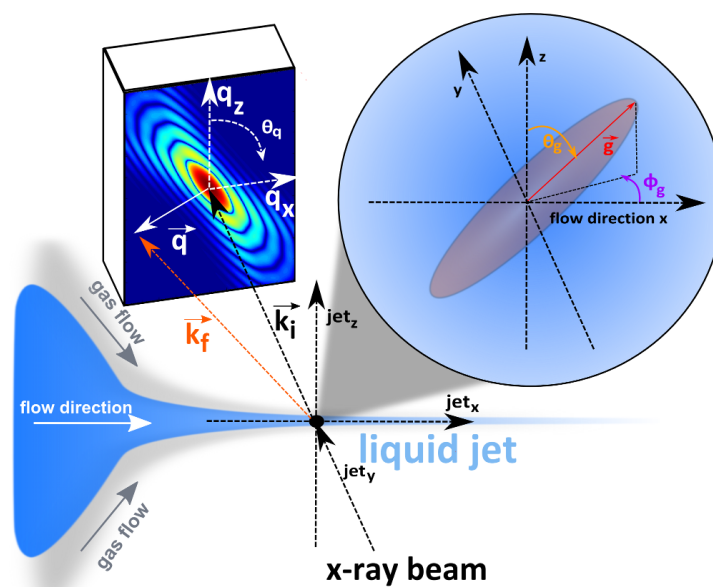
Figure 4.26: Sketch of a hematite particle in a liquid jet formed by a GDVN. The coordinates of the particle orientation and the wave vector transfer according to figure 2.4 and figure 2.9 are shown.
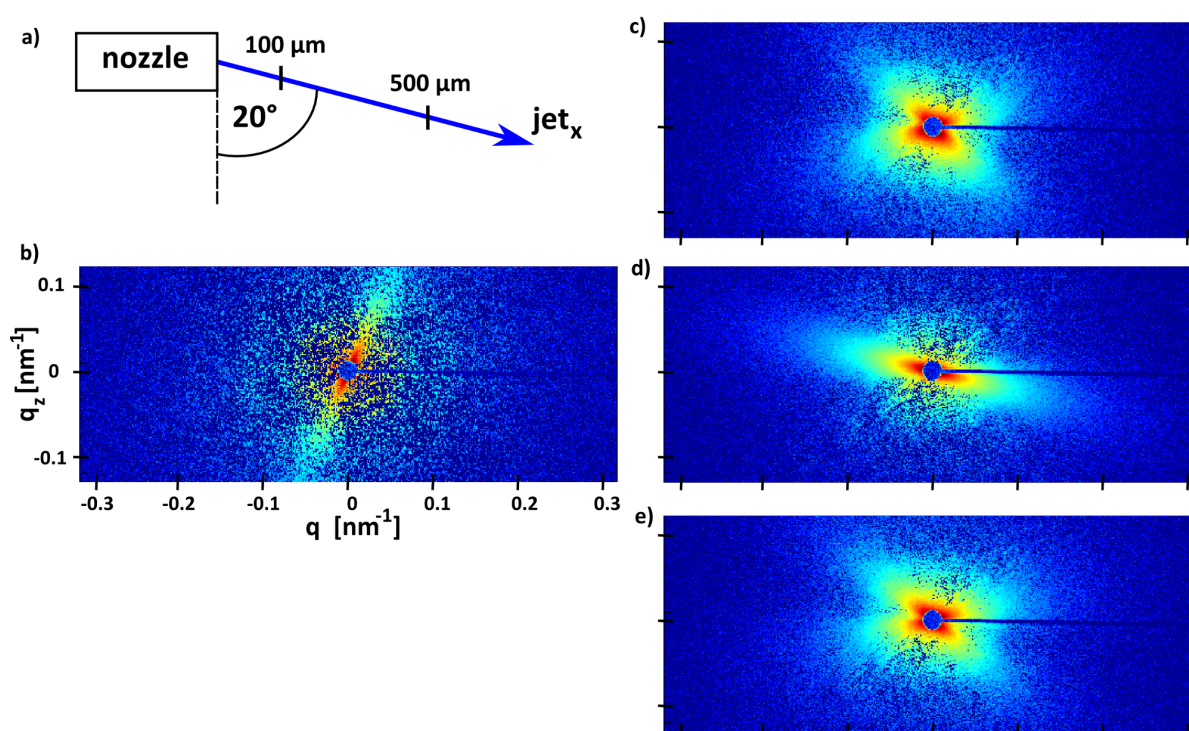
Figure 4.27: Four SAXS pattern measured at different locations on the liquid jet. a) Sketch of bended liquid jet. b) $jet_x = 100\,\mu m$, $jet_z = 0\,\mu m$. c) $jet_x = 500\,\mu m$, $jet_z = 0\,\mu m$. d) $jet_x = 500\,\mu m$, $jet_z = 8\,\mu m$. e) $jet_x = 500\,\mu m$, $jet_z = -8\,\mu m$.
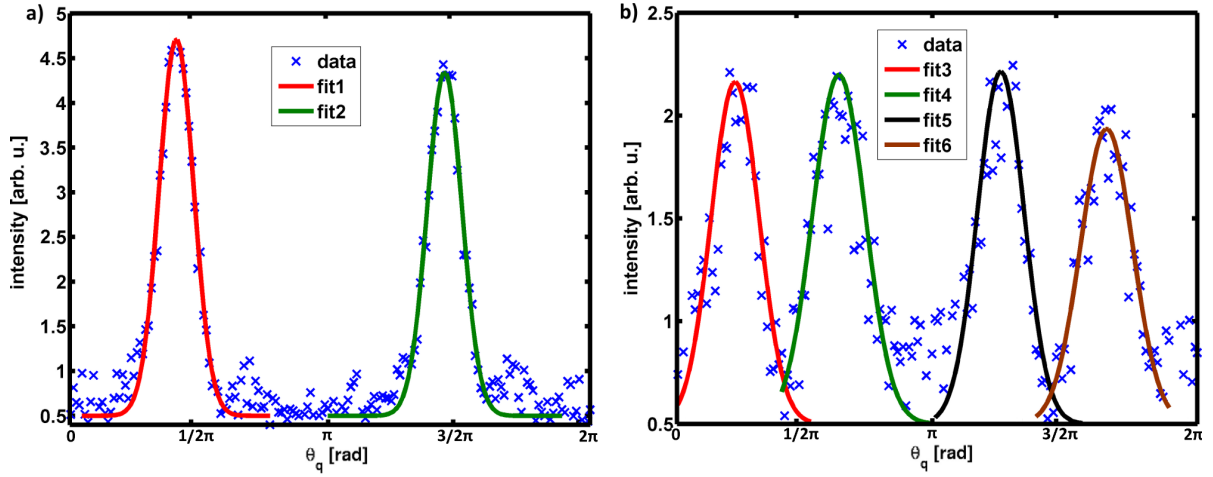
Figure 4.28: Azimuthally profiles of the form factors as function of θ_q at $q = 0.05\,\text{nm}^{-1}$. a) Result of SAXS pattern shown in 4.27 d) ($\text{jet}_x = 500\,\mu\text{m}$, $\text{jet}_z = 0\,\mu\text{m}$). b) Result of SAXS pattern shown in 4.27 c) ($\text{jet}_x = 500\,\mu\text{m}$, $\text{jet}_z = 8\,\mu\text{m}$).

the SAXS pattern. To locate the maxima and to extract the azimuthal width $\Delta\theta_q$ Gaussian functions (equation 4.21) were fitted to the data. The results of the fits shown in figure 4.28 are presented in table 4.4 together with the values for the azimuthal widths $\Delta\theta_q$. The azimuthal width extracted from figure 4.28 a) is $\Delta\theta_{q,\text{ave}} = 0.69\,\text{rad}$. This value is slightly above the calculated azimuthal width $\Delta\theta_{q,\text{calc}} = 0.59\,\text{rad}$, which indicates a narrow distribution of particle orientations about the jet center ($\text{jet}_x = 500\,\mu\text{m}$, $\text{jet}_z = 0\,\mu\text{m}$). The azimuthal widths $\Delta\theta_{q,\text{ave}}$ extracted from figure 4.28 b) are larger, indicating particles with a wider orientation distribution above the jet center ($\text{jet}_x = 500\,\mu\text{m}$, $\text{jet}_z = 8\,\mu\text{m}$).

As different particle orientations were measured in the jet (figure 4.27) the azimuthal location μ is analyzed for all measurements across the liquid jet at $\text{jet}_x = 500\,\mu\text{m}$, see figure 4.29 a). The scattering intensities on a ring of constant $q = 0.05\,\text{nm}^{-1}$ are plotted as function of θ_q and jet_z. The azimuthal locations μ of the maximum are shifting as function of jet_z. At the jet center ($\text{jet}_z = 0\,\mu\text{m}$) two pronounced maxima represent a single particle orientation. In the region from $\text{jet}_z = -8\,\mu\text{m}$ to $\text{jet}_z = -1\,\mu\text{m}$ and from $\text{jet}_z = 1\,\mu\text{m}$ to $\text{jet}_z = 8\,\mu\text{m}$ four maxima at different azimuthal locations μ and azimuthal widths $\Delta\theta_{q,\text{ave}}$ are shown. This reflects the SAXS pattern showing an "X-shape" such as figure 4.27 c) and d). At $\text{jet}_z = -9\,\mu\text{m}$ and $\text{jet}_z = 9\,\mu\text{m}$ the four maxima merged to two maximas with large $\Delta\theta_q$ values.

The intensity measured at $q = 0.05\,\text{nm}^{-1}$ as function of jet_z at $\text{jet}_x = 100\,\mu\text{m}$ are shown in figure 4.29 b). The azimuthal location μ is not changing as function of jet_z, which shows that the particle orientation is not changing across the liquid jet at $\text{jet}_x = 100\,\mu\text{m}$. Furthermore,
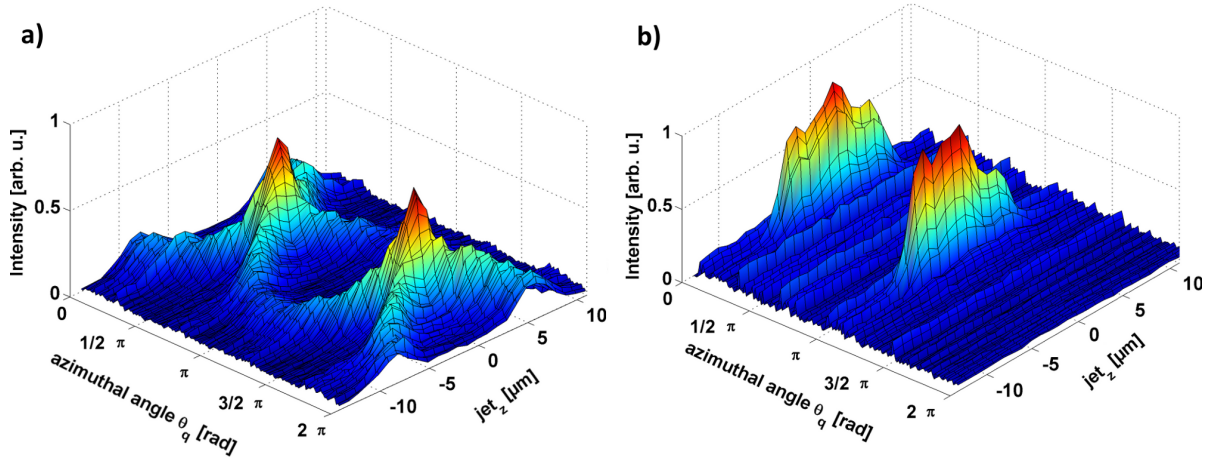
Figure 4.29: The scattered intensity on a ring of constant $q = 0.05\,\mathrm{nm}^{-1}$ as function of jet_z and θ_q. The different plots show the results of measurements taken at different jet_x values. a) $\mathrm{jet}_x = 500\,\mu\mathrm{m}$. b) $\mathrm{jet}_x = 100\,\mu\mathrm{m}$.

	$A[\mathrm{arb.\ u.}]$	$\mu[\mathrm{rad}]$	$\sigma_s[\mathrm{rad}]$	$\Delta\theta_q[\mathrm{rad}]$
fit1	4.5 ± 0.7	1.29 ± 0.04	0.29 ± 0.05	0.69 ± 0.11
fit2	4.2 ± 0.1	4.53 ± 0.01	0.29 ± 0.01	0.69 ± 0.03
fit3	2.2 ± 0.1	0.70 ± 0.03	0.41 ± 0.04	0.96 ± 0.10
fit4	2.2 ± 0.1	1.96 ± 0.02	0.45 ± 0.04	1.05 ± 0.09
fit5	2.2 ± 0.2	3.91 ± 0.26	0.39 ± 0.05	0.93 ± 0.11
fit6	1.9 ± 0.1	5.19 ± 0.03	0.44 ± 0.04	1.04 ± 0.10

Table 4.4: Results of fits of Gaussian function in figure 4.28.

the azimuthal width $\Delta\theta_q$ is not changing significantly.

The data allow a determination of the jet diameter d_{jet}. The total scattering intensity is studied as a function of jet_z at $\mathrm{jet}_x = 500\,\mu\mathrm{m}$, see figure 4.30 a). The resulting intensity profile across the jet shows two maxima at $\mathrm{jet}_z = -5\,\mu\mathrm{m}$ and at $\mathrm{jet}_z = 5\,\mu\mathrm{m}$. The location of the half height was used to determine the edges of the liquid jet. The error of this value was estimated by the step size $\Delta\mathrm{jet}_z = 1\,\mu\mathrm{m}$ of the measurements. The jet diameter d_{jet} as a function of jet_x is depicted in figure 4.30 b). The dashed red lines in figure 4.30 b) are guide to the eye. At $\mathrm{jet}_x = 500\,\mu\mathrm{m}$ the slope changes significantly, which indicates a change of the geometry of the liquid jet. One explanation would be that the liquid jet breaks up at this distance. Since no stroboscopic light was used to visualize the liquid jet the break-up process was not visible during this experiment. However, the measured jet diameter at $\mathrm{jet}_x = 400\,\mu\mathrm{m}$ is $d_{\mathrm{jet}} = 16\,\mu\mathrm{m}$ and at $\mathrm{jet}_x = 500\,\mu\mathrm{m}$ the diameter is $d_{\mathrm{jet}} = 18\,\mu\mathrm{m}$. The predicted droplet diameter from literature is $d_{\mathrm{droplet}} \cong 1.89 \cdot d_{\mathrm{jet}} \approx 30\,\mu\mathrm{m}$ (see equation 3.11), which is larger than the measured jet diameters. This is not understood but one might argue that the droplet diameter can
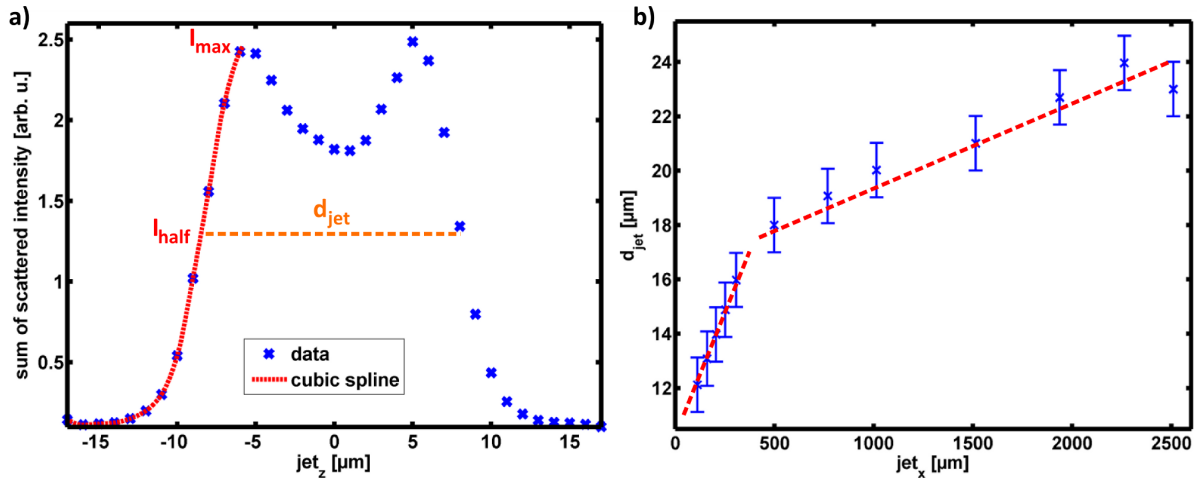
Figure 4.30: a) Sum of the total measured scattering intensity at different locations across the liquid jet at $jet_x = 500\,\mu m$. b) Jet diameter d_{jet} as function of the distance jet_x.

shrink at high shear rates and high velocities.[43] The scattering signal represents the scattering from the hematite particles in the liquid jet and not the scattering signal from the solvent (water).

In figure 4.31 the variation of the scattering signal shown in figure 4.30 a) is plotted as a function of jet_x and jet_z. It is visible, that the scattering intensity decreases as function of jet_x. This could be connected to a decrease of the particle density in the measured volume due to an expansion of the liquid jet or a break-up of the liquid jet (figure 4.30 b)). In this plot the two maxima indicate density variations are also visible above and below the jet center. The peaks vanish with increasing jet_x values. This indicates that the density variation across the liquid jet vanish with increasing jet_x values.

The azimuthal location μ and azimuthal width $\Delta\theta_{q,ave}$ were analyzed for all measurements at $jet_x \leq 1000\,\mu m$. The results are depicted in figure 4.32. In this plot the SAXS patterns recorded at different locations are represented by boxes. The coloring of the boxes indicate the particle alignment that is determined by the SAXS pattern. For a particle alignment parallel to the flow direction jet_x the boxes are colored in light blue, while for a particle alignment perpendicular to the flow direction the boxes are colored in red. The position in the liquid jet where an "X-shape" pattern (see figure 4.27 c) and d)) was measured are colored in green. For each SAXS pattern the azimuthal locations μ are shown as blue bars and the azimuthal widths $\Delta\theta_{q,ave}$ by red bars.

The plots in figure 4.29 are presented in figure 4.32 at $jet_x = 100\,\mu m$ and $jet_x = 500\,\mu m$. For $jet_x = 100\,\mu m$ no shift of the radial location μ as function of jet_z was measured and thus a

---

[43]Gordillo, J.M. et al. *J. Fluid. Mech.* **448**, (2001), 23.
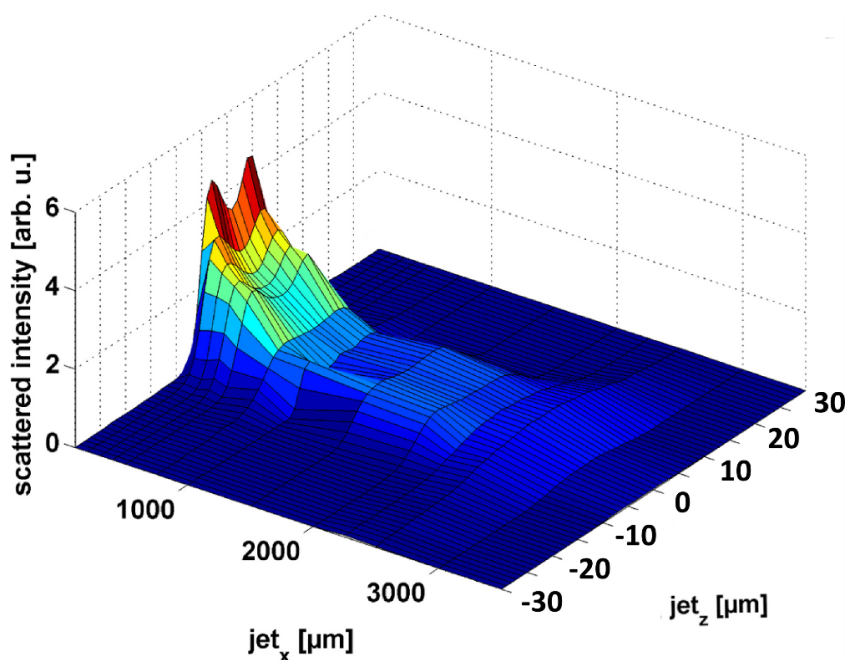
Figure 4.31: Sum of the total measured scattering intensity as function of jet_x and jet_z.

single particle alignment is visible. The azimuthal widths $\Delta\theta_{q,ave}$ at $jet_x = 100\,\mu m$ do not change significantly as function of jet_z. This indicates that all particles show a similar ODF. For $jet_x = 500\,\mu m$ the alignment and the degree of alignment changes as function of jet_z. This is represented by different colors in figure 4.32. Above and below the jet center ($jet_z < -4\,\mu m$ and $jet_z > 7\,\mu m$) the particles were aligned with their major semi-axis parallel to the flow direction, while at the jet center ($jet_z = 0\,\mu m$) the particles were aligned perpendicular to the flow direction. In between these regions two different particle alignments were measured (see figure 4.27 c) and d)). At these locations, the difference of the radial locations μ changes as function of jet_z, which implies that the two particle orientations changes relative to each other. The SAXS patterns recorded at $jet_x > 100\,\mu m$ show similar particle alignments across the liquid jet. However, the azimuthal widths measured at $jet_x = 1000\,\mu m$ are large compared to the measurements at $jet_x = 100\,\mu m$. This indicates a low degree of particle alignment at $jet_x = 1000\,\mu m$.

4.3.4 Conclusion and discussion

The measured SAXS patterns show a pronounced particle alignment in flow direction close to the nozzle and an alignment perpendicular to it at $jet_x > 100\,\mu m$. The transition of these two states is characterized by mixture of two different particle alignments, see figure 4.32.
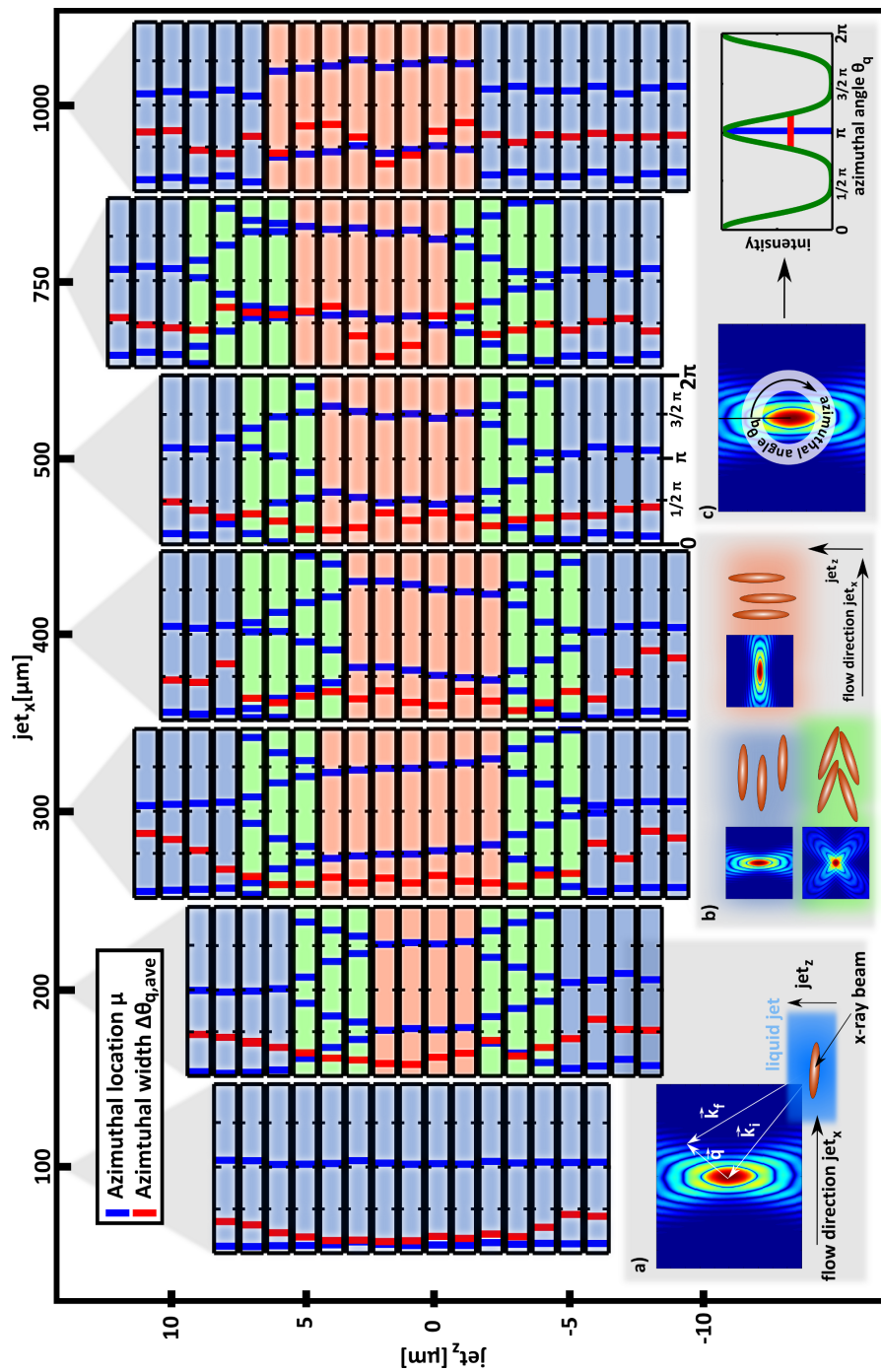
Figure 4.32: Overview of the radial widths $\Delta\theta_{q,ave}$ and radial locations μ for different jet locations (jet$_x$ and jet$_z$). Furthermore, the particle alignment is illustrated at each jet location with a color code. The general scattering geometry is introduced in inset a). The color code of the graphic is introduced in inset b). The inset c) sketches the extraction of the radial width $\Delta\theta_{q,ave}$ and the radial location μ as explained in figure 4.28.

Wether or not the reorientation happens within the jet or is due to droplet formation is not completly clear since the diagnostics for droplet formation were not installed at the moment the experiment was carried out. It is however likly that the data were taken in the jetting regime since typically jet lengths are about a few hundred μm. Thus, one can assume that the particle reorientation from $jet_x = 100$ μm to $jet_x = 200$ μm were measured in the liquid jet. The particle reorientation is related to the shear flow of the liquid jet, see section 4.1. For an estimation of the shear rate the rotational motion can be analyzed. Between one location close to the nozzle tip ($jet_x = 100$ μm, $jet_z = 0$ μm) and a location further away ($jet_x = 200$ μm, $jet_z = 0$ μm) the particle alignment changes by approximately $\Delta\theta_g = 90°$. The distance between these locations is 100 μm and with the typical flow velocity of the jet ($Q = 12\,\frac{\mu l}{min}$) the elapsed time of the shear flow can be estimated to $t = 10^{-4}$ s. With these values and the aspect ratio $\nu = 3.33$ the shear rate can be estimated to $\dot{\gamma} \geq 5.4 \cdot 10^4$ Hz, see equation 4.11. This calculation takes many approximations into account such as a homogenous flow velocity, negligible Brownian motion, and a highly elongated particle shape. Furthermore, equation 4.11 is derived for ellipsoidal particles and not for spindle-shaped particles. However, this calculation leads to an estimation of the shear rate $\dot{\gamma}$ present in a liquid jet produced by a GDVN. The magnitude of the shear rate is larger than in conventional rheological experiments with rheometers ($\dot{\gamma} = 10^2$ Hz $- 10^3$ Hz).[44] Therefore, measurements of diluted dispersions in a liquid jet are promising for studies on complex liquids under high shear rates. The increase of the jet diameter as function of jet_x, indicates a biaxial extensional flow parallel to the jet_z-jet_y-plane , see figure 4.26. It is known that elongated particles in biaxial extensional flows align parallel of the extensional flow, figure 4.4 a). Therefore, spindle-shaped particles would align perpendicular to the jet_x-axis and in this way perpendicular to the flow direction of the liquid jet. A biaxial compressional flow parallel to the jet_z-jet_y-plane is present at the formation of the liquid jet, see figure 3.8. The helium gas compresses the jet parallel to the jet_z-jet_y-plane. Such a compressional flow leads to a particle alignment along the jet_x-axis, see figure 4.4 b). Thus, one might interpret the different alignments of the spindle-shaped particles within the jet as result of expansional and compressional flows, see figure 4.33. However, one has to consider, that the SAXS patterns were taken in transmission geometry. Thus, the particles were probed through the liquid jet. In this way a two dimensional (jet_x, jet_z) reconstruction of the particle alignment in the jet was done without considering the alignment in the third dimension (jet_y). Furthermore, the break-up process of the liquid jet was not determined, thus it is not clear if the particle reorientation was measured in the jet or in the droplets.

---

[44]Macosko, C.W. *Rheology Principles, Measurements, and Applications*. Toronto, Canada: Wiley-VCH, 1994.
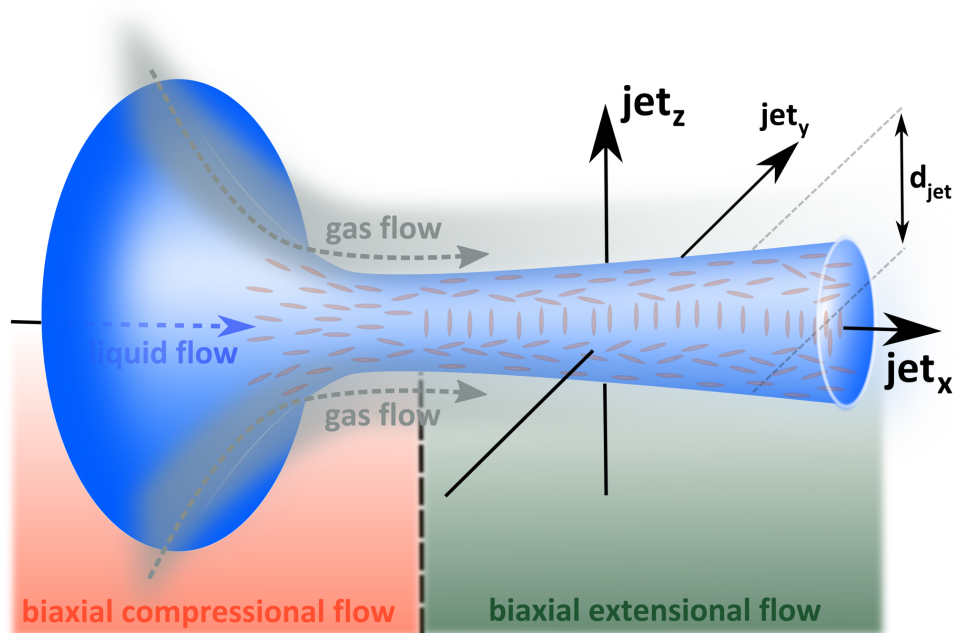
Figure 4.33: Sketch of a liquid jet formed with the flow focusing technique to illustrate the particle orientation in the jet. Proposed alignments of the hematite particles are shown at different liquid jet locations.

The density variations across the jet indicate a variation of the volume fraction of the hematite particles across the jet. This suggests that the volume fraction of hematite particles increases above and below the jet center (jet$_z$ = 0 μm) due to an inertia particle migration known from spherical particles, see figure 4.2.[45] Inertia migration is induced by wall interactions, see section 4.1. As an estimate whether or not particle migration can occur the spindle-shaped particle were approximated by a sphere with radius $R = \frac{L+R_1}{2}$ and the capillary radius could be estimated with the jet diameter $r_c = \frac{d_{jet}}{2}$. Typical flow rates of GDVNs are around $Q = 10 \frac{\mu l}{min}$. With a jet diameter of $d_{jet} = 15$ μm the flow velocity is $v_{jet} \approx 1 \frac{m}{s}$. The density of hematite is $\rho_p = 5.2 \frac{g}{cm^3}$. With these values the criterion for particle migration in shear flows is fulfilled as $K \approx 10^{-5} < 0.01$, see equation 4.6. This result supports the assumption of a particle migration in the liquid jet.

---

[45]Carlo, D.D. *Lab Chip* **9**, (2009), 3038; Ho, B.P. et al. *J. Fluid Mech.* **65**, (1973), 365; Segre, G. et al. *Nature* **189**, (1961), 209.

5 X-ray scattering from water

Water is in the focus of science for more than one century.[1] In comparison to other liquids water shows several anomalies such as the density anomaly. The water molecule is bent and it has partial charges. Thus it forms hydrogen bonds with each other. It is believed that the local structure of liquid water is the reason of the anomalies. Up to now the local structure of water in the liquid phase is controversially discussed. X-ray cross correlation analysis (XCCA) of speckle patterns originating from coherent scattering is a promising tool to study the structural symmetries of liquid samples.[2] In the framework of this thesis a feasibility study was performed to test if speckle patterns from liquid water can be recorded at FEL sources with sufficient statistical quality and sufficient speckle contrast to perform XCCA.
Section 5.1 chapter starts with an introduction to water anomalies and structure models. It is followed by section 5.2 presenting the x-ray scattering experiment on liquid water unsin the liquid jet setup. The data treatment is described followed by a discussion of the quality of the recorded diffraction patterns.

5.1 Liquid water

The local structure of water in the liquid phase is up to now an unsolved problem and controversially discussed.[3] The water molecule is bent and consists of two hydrogen atoms that have a positive partial charge and one oxygen atom that has a negative partial charge, see figure 5.1.[4] Thus, water molecules form hydrogen bonds between each other. This is the origin for different descriptions of the local structure of water.[5] It is assumed that this structure influences the macroscopic thermodynamic properties including several anomalies,

---

[1] Grohmann, N. *Wasser: Chemie, Mikrobiologie und nachhaltige Nutzung.* Oxford, University Press, 2011; Ball, P. *Chem. Rev.* **108**, (2008), 74; Röntgen, W.C. *Ann. Phys. Chem.* **45**, (1892), 91.

[2] Wochner, P. et al. *PNAS* **106**, (2009), 11511; Russo, J. et al. *Nat. Com.* **5**, (2014), 3556.

[3] Nilsson, A. et al. *Chem. Phys.* **389**, (2011), 1; Ludwig, R. *Angew. Chem. Int. Ed.* **40**, (2001), 1808; Wernet, Ph. et al. *Science* **304**, (2004), 995; Clark, G.N.I. et al. *Mol. Phys.* **11**, (2010), 1415; Leetmaa, M. et al. *J. Chem. Phys.* **129**, (2012), 084502.

[4] Grohmann, N. *Wasser: Chemie, Mikrobiologie und nachhaltige Nutzung.* Oxford, University Press, 2011.

[5] Clark, G.N.I. et al. *PNAS* **107**, (2010), 14003; Huang, C. et al. *PNAS* **106**, (2009), 15214.
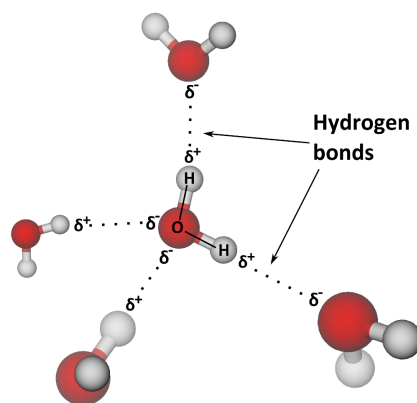
Figure 5.1: Schematic sketch of water molecules. The oxygen atoms are colored in red and the hydrogen
         atoms are colored in white. Furthermore, the partial charge of the atoms and the hydrogen
         bonds are shown.

see figure 5.2.[6] In this figure the heat capacity c_p, the thermal expansion α_p, and the isothermal
compressibility K_T of water are compared to a simple liquid, such as a Lenard Jones liquid.[7,8]
The thermodynamically properties of water show a different behavior compared to a typical
liquid.[9] The anomalies occur above the melting temperature of water T_m. However, below T_m
the anomalies are more pronounced. Therefore, a study of the local structure of water in this
temperature region is in the focus of research for understanding the water anomalies. Various
models for the local structure of water are proposed for this regime predicting mixtures of
high and low density structures or a network of hydrogen bonded water molecules.[10] Basically,
two different types of water models are known: On the one hand the continuum models
predicts a network of tetrahedrally bonded water molecules, on the other hand the mixture
models predicts two different compounds of water molecules with different densities. These
models are shortly introduced in the following section.

---

[6]Errington, J.R. et al. *Nature* **409**, (2001), 318; Stanley, H.E. et al. *Physica A* **106**, (1981), 260.

[7]It is described by van der Waals interactions at intermolecular distances.

[8]Lennard-Jones, J.E. *Prog. Phys. Soc.* **43**, (1931), 461.

[9]Speedy, R.J. et al. *J. Chem. Phys.* **65**, (1976), 851; Angell, C.A. et al. *Physica A* **106**, (1982), 260; Rasmussen,
   D.H. et al. *J. Chem. Phys.* **59**, (1973), 5003.

[10]Soper, A.K. et al. *Phys. Rev. Lett.* **84**, (2000), 2881; Smith, R.S. et al. *Nature* **398**, (1999), 788; Errington, J.R.
   et al. *Nature* **409**, (2001), 318.
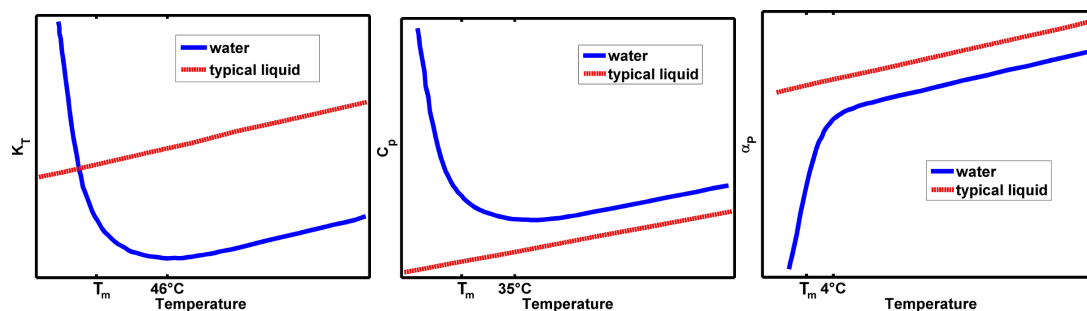
Figure 5.2: Schematic temperature dependency of the isothermal compressibility K_T, the specific heat capacity c_p, and the thermal expansion coefficient α_p. The behavior of water is shown by the blue solid line. The behavior of a Lenard-Jones liquid is represented by the red line. T_m denotes the melting temperature. The images are adapted from: Debendetti, P.G. et al. *Phys. Today* **56**, (2003), 40.

5.1.1 Mixture models

The mixture models predict a mixture of different water compounds to describe the water anomalies.[11] Different modifications of this model are known.[12] Currently, the most accepted one is the liquid-liquid critical point (LLCP) model.[13] In this model the local structure of water is described with a mixture of two phases called low density liquid (LDL) and high density liquid (HDL). The LDL phase shows more tetrahedrally coordinated water molecules compared to the HDL phase. Thus, the LDL phase is less dense compared to the HDL phase.[14] Indications for this hypothesis are based on various experimental and theoretical work.[15]

Hence, a schematic phase diagram can be proposed including different regimes of water phases, see figure 5.3.[16] The HDL and the LDL phases are separated in the temperature-pressure plane by a coexistence line. At this line the phases should be mixed. The origin of this line is at a critical point (T_c, p_c) in the supercooled regime with a continuation to lower temperatures.[17] The coexistence line separates the phases below T_c. At low temperatures the LDL phase is present, while at high temperatures the HDL phase is present. Above the critical point

[11]Pople, J.A. *Proc. R. Soc. A* **205**, (1951), 163.

[12]Angell, C.A. *Science* **319**, (2008), 582; Speedy, R.J. *J. Phys. Chem.* **86**, (1982), 982; Sastry, S. et al. *Phys. Rev. E* **53**, (1996), 6144.

[13]Poole, P.H. et al. *Nature* **360**, (1992), 324.

[14]Brovchenko, I. et al. *J. Chem. Phys.* **124**, (2006), 164505; Soper, A.K. et al. *Phys. Rev. Lett.* **84**, (2000), 2881.

[15]Fanetti, S. et al. *J. Phys. Chem. Lett.* **5**, (2014), 235; Xu, L. et al. *PNAS* **102**, (2005), 16558; Paschek, D. et al. *Chem. Phys. Chem.* **9**, (2008), 2737; Brovchenko, I. et al. *Chem. Phys. Chem.* **9**, (2008), 2660; Corradini, D. et al. *J. Chem. Phys.* **132**, (2010), 134508; Mishima, O. et al. *Nature* **392**, (1998), 164; Mishima, O. *J. Chem. Phys.* **133**, (2010), 144503.

[16]Nilsson, A. et al. *Chem. Phys.* **389**, (2011), 1.

[17]Poole, P.H. et al. *Nature* **360**, (1992), 324.
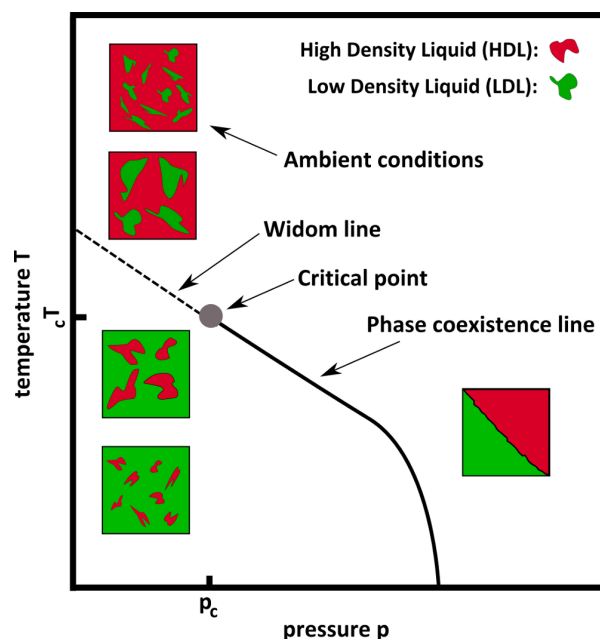
Figure 5.3: Schematic picture of a hypothetical phase diagram of liquid water consistent with the LLCP model. Only the phase coexistence line, the LLCP and the Widom line are shown for simplicity. Image adapted from: Nilsson, A. et al. *Chem. Phys.* **389**, (2011), 1.

$(T > T_c)$ the two phases are not separated anymore. At pressures below p_c and above T_c the coexistence line is continued by the so-called Widom line, which does not define a sharp transition between the two phases.[18] The mixing ratio of these phases below p_c and apart from the Widom line depend on the separation to it. In this model, the origin of the anomalous properties of water is explained by the increase of density fluctuations as water is cooled down. Then different patches of HDL and LDL should induce the density fluctuations of water.

5.1.2 Continuous models

The continuous models predict a tetrahedral network of water molecules. The local structure of liquid water is characterized by the degree of distorted or broken hydrogen bonds. The liquid phase is described by one substance. This picture of the local structure of water arises from molecular dynamics simulations and density functional theory that do not support the mixture model. Moreover, simulations of near-tetrahedral structures of water molecules show agreement with spectroscopy studies. Spectroscopy experiments on liquid water do not describe the existence of two distinguishable water compounds.[19] Various interpretations of

---

[18]Franzese, G. et al. *J. Phys.: Condense Matter* **19**, (2007), 205126; Kumar, P. et al. *PNAS* **104**, (2007), 9575.
[19]Pylkkänen, T. et al. *J. Phys. Chem. B* **115**, (2011), 14544.

the spectra of liquid water are known predicting broken and distorted hydrogen bonds[20] or vibration of the oxygen and hydrogen bond.[21] The common ground of the mixture models and the continuous models is the prediction of an increase of tetrahedral coordination of the water molecules by decreasing temperature.

5.2 X-ray scattering from water

Up to now direct measurements of the different liquid phases of water do not exist as experimental challenges are difficult to overcome. To perform an x-ray scattering experiment on liquid water in the supercooled state several experimental parameters have to be considered. Even more requirements have to be fulfilled to measure speckle patterns, see section 2.4. The strictest constraints are listed below.

- **X-ray energy and pulse length**
  The characteristic length scale of the local structure of water is between $2\,\text{Å}$ and $3\,\text{Å}$.[22] Therefore, x-rays in the hard x-ray regime have to be used to probe the local structure of water. Moreover, the lifetime of structural domains in water is expected to be a few hundred fs.[23] Thus, a coherent scattering experiment on liquid water has to be performed at a free-electron laser (FEL) that emits x-ray pulses sub 100 fs length. Such an XFEL is the Linac Coherent Light Source (LCLS)[24]. The LCLS emits x-ray pulses with a length $< 100\,\text{fs}$ at a repetition rate of 120 Hz.[25]

- **Detector size and resolution**
  The location of the first peak of the liquid water structure factor is at $q \approx 2\,\text{Å}^{-1}$.[26] According to equation 2.2 and an x-ray energy of 8 keV the scattering angle of the first peak of the structure factor can be observed at $\theta \approx 28°$. Thus, a wide angle x-ray scattering experiment (WAXS) has to be performed for probing the local structure of liquid water, see figure 5.4. The maximum scattering angle θ_{max} is connected via $\tan(\theta_{\text{max}}) = \frac{g}{d}$ to the sample-detector distance d and the size of the sensitive area of the detector g. Therefore, a detector with a large sensitive area is needed to record

---

[20]Wernet, Ph. et al. *Science* **304**, (2004), 995; Smith, J.D. et al. *Science* **306**, (2004), 851.

[21]Huang, C. et al. *PNAS* **106**, (2009), 15214.

[22]Head-Gordon, T. et al. *Chem. Rev.* **102**, (2002), 2651.

[23]Garrett-Roe, S. et al. *J. Phys. Chem. B* **115**, (2011), 6976.

[24]Stanford Linear Accelerator Center, Menlo Park, California, USA

[25]Emma, P. et al. *Nat. Photonics* **4**, (2010), 641.

[26]Clark, G.N.I. et al. *PNAS* **107**, (2010), 14003; Wikfeldt, K.T. et al. *J. Phys. Chem. B* **113**, (2009), 6246; Head-Gordon, T. et al. *PNAS* **103**, (2006), 7973; Hura, G. et al. *Phys. Chem. Chem. Phys.* **5**, (2003), 1981.
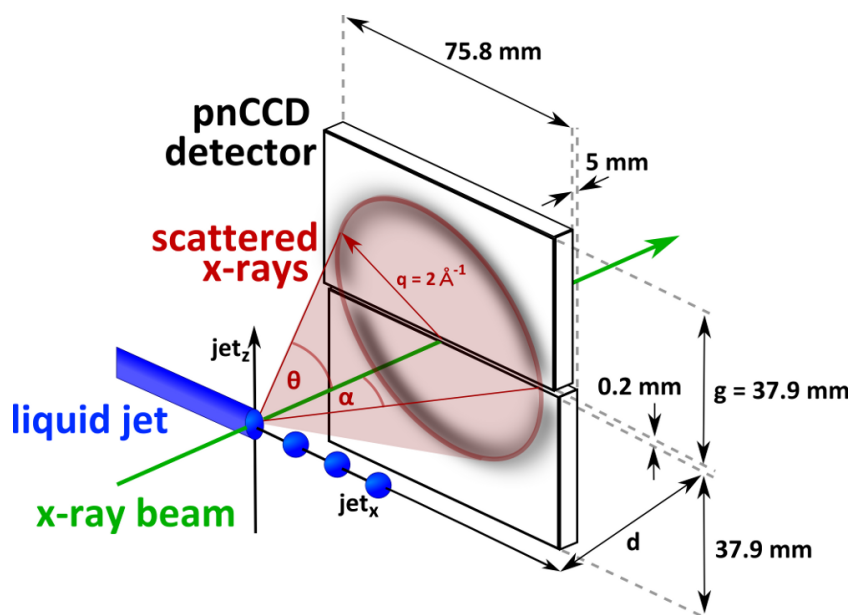
Figure 5.4: Sketch of the scattering geometry with the pnCCD detector and a liquid jet. The CCDs, the x-ray beam direction, flow direction, and scattering angle θ are shown.

the whole scattering ring originating from the structure factor of liquid water. One possible detector device that can be triggered to 120 Hz readout frequency is the pnCCD detector.[27] It consists of two charge couple devices (CCD) to record photons from the soft to the hard x-ray regime and is therefore frequently used for scattering experiments at FELs.[28] The dimension of the sensitive area is 75.8 mm x 75.8 mm.[29] Each CCDs has 1024 x 512 pixels. The pixel size of this detector is 75 µm x 75 µm.[30] The CCDs of the detector unit are horizontally separated by 200 µm and vertically by 5 mm, see figure 5.4. This arrangement allows the direct x-ray beam to pass.

- **Speckle contrast**

  For the analysis of speckle patterns the speckles need to be detected with a high as possible contrast β. The speckle contrast in wide angle experiments depends strongly on the thickness of the sample and the longitudinal coherence length ξ_l, see section 2.4. The thickness of the liquid sample system can be minimized to several µm by using a GDVN. As the longitudinal coherence length at a beamline using monochromatic

---

[27]The pnCCD was developed in the 1990s for the XMM-Newton mission of the European space agency. Strüder, L. et al. *Astron. Astrophys.* **365**, (2001), L18.

[28]Meidinger, N. et al. *Nuc. Inst. Meth. Phys. Res. A* **565**, (2006), 251.

[29]Meidinger, N. et al. *Nuc. Inst. Meth. Phys. Res. A* **565**, (2006), 251.

[30]Meidinger, N. et al. *Nuc. Inst. Meth. Phys. Res. A* **565**, (2006), 251; Send, S. et al. *Nuc. Inst. Meth. Phys. Res. A* **711**, (2013), 132.

x-rays at LCLS is around $\xi_l = 1.4\,\mu m$ the sample thickness should be about the same size.[31]

- **Supercooled water**

  To study anomalies of liquid water, the experiment has to be performed in the super-cooled regime, see figure 5.2. It is difficult to reach temperatures below the melting temperature T_m of water because water has be cooled faster than it freezes. Recently an x-ray diffraction experiment from supercooled water down to $T = 227\,K$ was published.[32] Measurements of liquid water at temperatures below $T = 227\,K$ were not realized up to now. This temperature regime is known as "no-man's land". At $T = 150\,K$ a phase transition from a liquid to a glassy phase is predicted.[33] For studying the local structure of water and in this way the water anomalies it is necessary to cool water down into the supercooled regime.[34] The droplets resulting from the break-up of the liquid jet offers the possibility to cool water droplets to the supercooled regime, see section 3.2.3. Therefore droplets can serve as sample target in such scattering experiments.[35]

To achieve these requirements a liquid jet setup with a GDVN has been developed in the framework of this thesis. This setup was used with a pnCCD detector at the x-ray free-electron laser LCLS. In the following sections the setup and the experiment is described in detail.

5.2.1 Setup

The WAXS experiment was performed at the XCS instrument at the free-electron laser LCLS at SLAC[36]. The instrument is dedicated to coherent X-ray Scattering in general and to X-ray Photon Correlation Spectroscopy in particular.[37] X-ray pulse lengths of around 100 fs with a repetition rate of 120 Hz were used. The instrument uses a double crystal monochromator with Si(111) crystals to offer monochromatic beams in the hard x-ray regime. In this experiment the x-ray energy was set to $E_{\text{x-ray}} = 8.4\,keV$. The LCLS was used in self-

---

[31]Robert, A. *Website, Beamline XCS*. 2014. URL: https://portal.slac.stanford.edu/sites/lcls_public/instruments/xcs/Pages/Components.aspx; Gutt, C. et al. *Phys. Rev. Lett.* **108**, (2012), 024801.

[32]Sellberg, J. A. "X-ray scattering and spectroscopy of supercooled water and ice." Dissertation. Stockholm University, 2014.

[33]Smith, R.S. et al. *Nature* **398**, (1999), 788; Li, T. et al. *Nature Com.* **4**, (2013), 1887; MAnka, A. et al. *Phys. Chem. Chem. Phys.* **14**, (2012), 4505.

[34]Nilsson, A. et al. *Chem. Phys.* **389**, (2011), 1.

[35]Sellberg, J. A. et al. *Nature* **510**, (2014), 381.

[36]Stanford Linear Accelerator Center, Menlo Park, California, USA

[37]Robert, A. et al. *J. Phys.: Conf. Ser.* **425**, (2013), 212009; Bakel, N.A. et al. *J. Phys.: Conf. Ser.* **425**, (2013), 062011.

seeded mode to increase the photon flux.[38]

 An overview of the experimental environment of the liquid jet is shown in figure 5.5. The setup is a modification of the setup discussed in section 4.3.1. The chamber was flanged directly to the flightpath of the XCS instrument to suppress scattering originating from air. The nozzle and a YAG-screen are mounted on a nozzle holder, which is moveable by a manipulator. For calibration and extraction of the diameter of the jet three different microscopes were used. A more detailed overview of the configuration of the microscopes is given in figure 5.6 a). The first microscope is used in an in-line geometry with a mirror. The mirror has a hole of 2 mm diameter. This hole allows the x-ray beam to pass. The mirror was moveable by a manipulator, see figure 5.5. The second microscope offers a view from the side (under 45°) on the liquid jet. In this way the jet could be monitored and one would control the stability of the jet. The third microscope is mounted on top of the setup, see figure 5.5. It offers a magnification factor up to 240 with a focal length of 20 mm. The magnification allows to study the jet diameter d_{jet}. For this purpose it can be calibrated via a reference scale, which is mounted on the nozzle holder, see figure 5.6 b). Using stroboscopic light the exposure time of the microscope was set to $t_e = 200$ ns. This time resolution allows to record static images of the break-up process and to analyze the droplets. Images taken with the described microscopes are shown in figure 5.7.

 In figure 5.6 b) a close-up of the nozzle holder is shown. In between the nozzle holder and the CCD a differential pumping stage was placed to compensate the pressure difference between the detector chamber and the nozzle setup. The differential pumping stage has a hole of 40 μm that allows the x-ray beam to pass. Around this hole a kapton foil was glued on the differential pumping stage. In the detector unit a pressure of 10^{-6} mbar was reached while the GDVN formed a liquid jet in the jet chamber with a pressure of 10^{-3} mbar. The liquid jet setup was pumped with a turbo pump[39], a booster pump[40], and a scroll pump[41]. To calibrate the setup in front of the differential pumping stage the nozzle holder was equipped with an x-ray diode, see figure 5.6 b). A YAG-screen was mounted on the nozzle holder to visualize the x-ray beam for the first microscope. This is necessary to find the position of the x-ray beam in the chamber. In this way the liquid jet could be moved to the x-ray beam. The reference scale on the nozzle holder was used to calibrate the third microscope. Furthermore, a knife edge was mounted to enable measurements of the beam size of the x-ray beam.

 The flow rate was measured by a micro flow meter[42] to $Q \approx 12 \frac{\mu l}{\mathrm{min}}$. In the experiment the

---

[38] Amann, J. et al. *Nature photonics* **6**, (2012), 693.

[39] Pfeiffer, HighPace 300

[40] Edwards, XJR35i

[41] Edwards, XJR100f
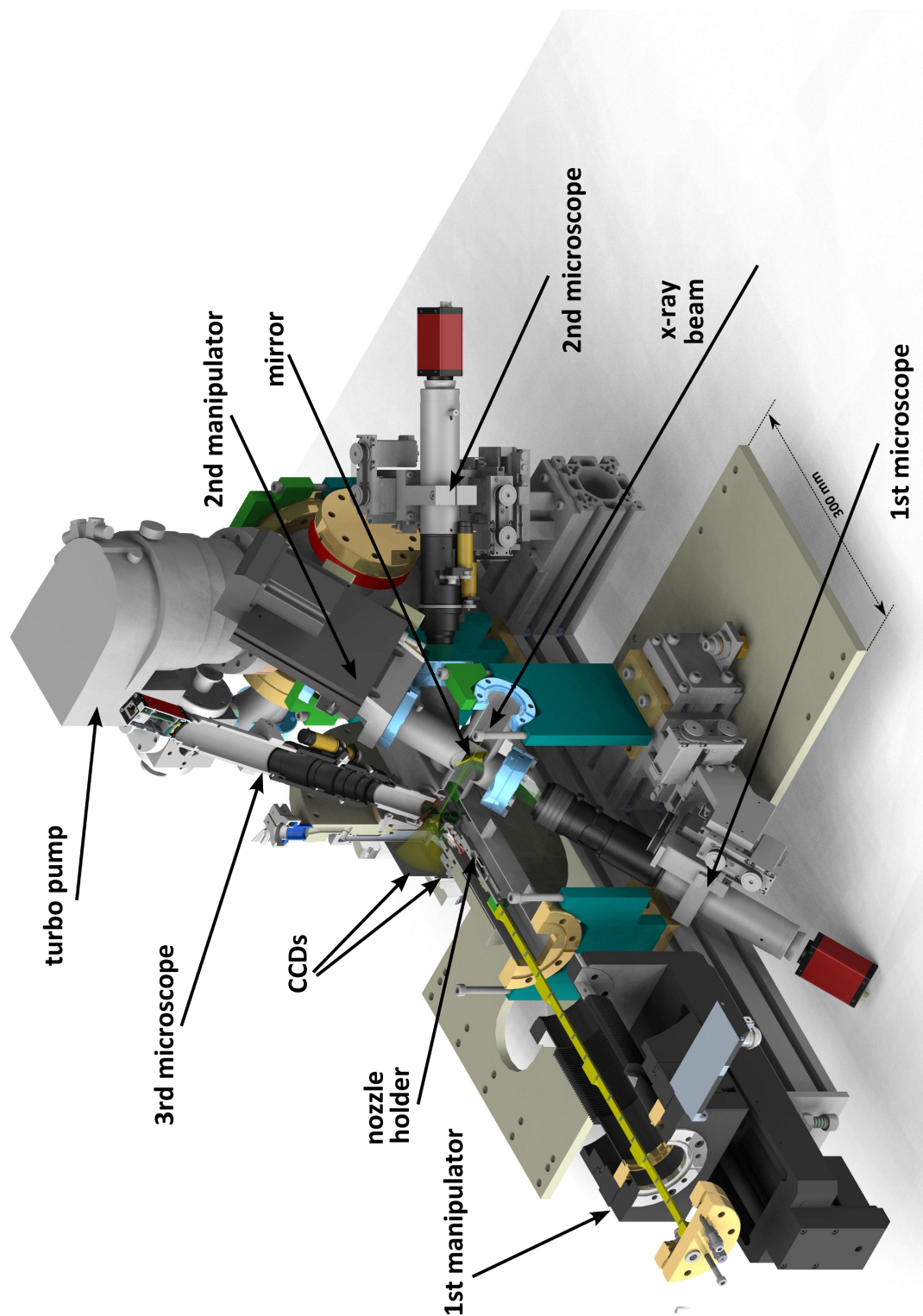
Figure 5.5: Overview about the liquid jet setup showing the x-ray beam direction, diagnostics, the nozzle holder, and the CCDs.
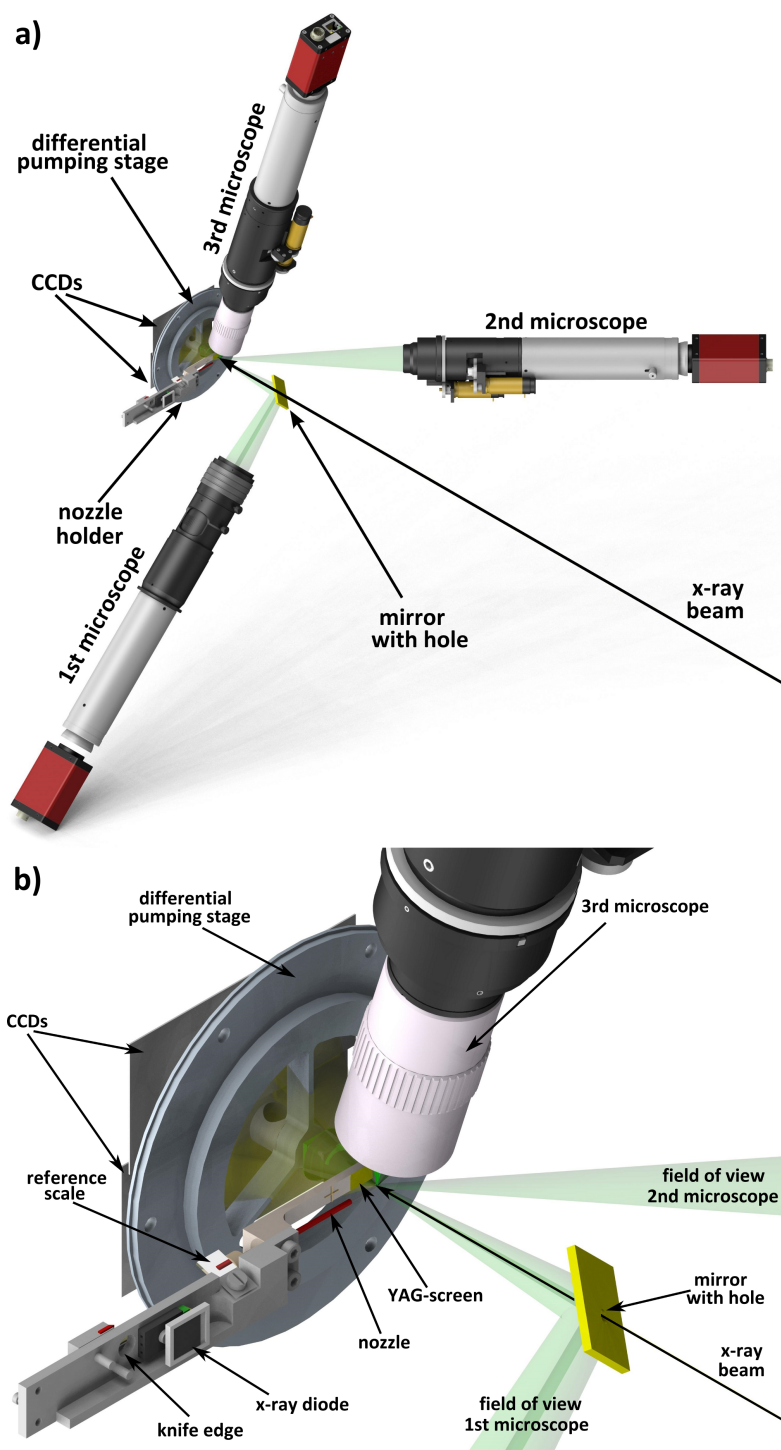
Figure 5.6: Two images of the liquid jet setup. a) The arrangement of the microscopes, mirror, differential pumping stage, and CCDs. For clear view vacuum components are not shown. b) Close up of the nozzle holder with the differential pumping stage. Different tools mounted on the nozzle holder are shown.

Figure 5.7: Three microscope images. a) 1st microscope in in-line geometry. b) 2nd microscope under 45°. c) 3rd microscope employing stroboscopic light and high magnification.

jet diameter was $d_{jet} = 3.6\,\mu m$ resulting in the flow velocity $v_{jet} = 17.3\,\frac{m}{s}$. Using the density $\rho_l = 1\,\frac{g}{cm^3}$, and the viscosity $\eta = 0.001\,Pa\cdot s$ of water at $T = 20\,°C$ the Reynolds number for the flowing system can be estimated to $Re = 52.4$.[43] With the surface tension of water $\sigma = 72.75\cdot 10^{-3}\,\frac{N}{m}$ the Weber number can be calculated to $We = 4.9$. With these values it is safe to assume that the liquid jet was formed in the steady jetting regime, see figure 3.9. The liquid jet was stable over the whole experimental time. Furthermore, the pressure drop of the GDVN can be approximated to $\Delta p = 204\,mbar$ (equation 3.20). The length of the jet was determined to $L \approx 230\,\mu m$, which is in good agreement with the predicted jet length using equation 3.16 of $L = 197\,\mu m$. The deviation is reasonable because equation 3.16 is derived for jets formed by a Rayleigh nozzle and not by a GDVN. The gas stream stabilizes the liquid jet and increases the jet length.

The measurements were taken in the liquid jet and at 7 mm distance to the break-up point. The coordinates are introduced in figure 5.4. The break-up point of the liquid jet represents the origin of the coordinate system. At $jet_x \leq 0\,\mu m$ the liquid jet is stable, while at $jet_x > 0\,\mu m$ droplets were present. Using equation 3.21 and 3.22 the expected temperature of a water droplet with droplet diameter of $5\,\mu m$ would have a temperature of $T = 251\,K$ at a flow velocity of $v_{jet} = 17.3\,\frac{m}{s}$ at $jet_x = 7\,mm$.

The jet-detector distance d was measured using a dispersion of hematite particles in the liquid jet. The crystalline atomic structure in the particle leads to Bragg reflections at high wave vector transfers that were used as reference signal to determine the sample-detector distance.

5.2.2 Spatial resolution of the pnCCD detector

The principle of semiconductor photon detectors is the measurement of the excited electrons in the semiconductor material that are generated by photon absorption. If a photon is detected

---

[42]Sensiron AG, SLG1430
[43]Grohmann, N. *Wasser: Chemie, Mikrobiologie und nachhaltige Nutzung.* Oxford, University Press, 2011.
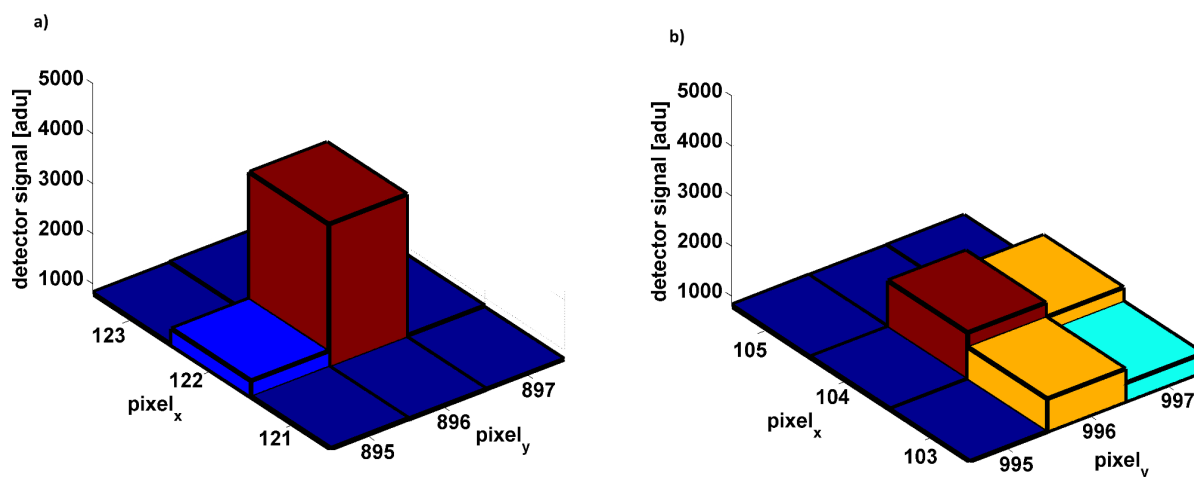
Figure 5.8: Two examples of pixel topologies. a) Two pixels show considerable detector signal above the noise level. The coordinates of the center pixel is ($pixel_x = 122$, $pixel_y = 896$). The center of mass of the signals is at ($pixel_x = 121.998$, $pixel_y = 895.900$) b) Four pixels with detector signals above the noise level. The center pixel has the coordinates ($pixel_x = 104$, $pixel_y = 996$) and the center of mass is at ($pixel_x = 104.380$, $pixel_y = 996.382$).

a charge cloud with electrons proportional to the photon energy is developed in a pixel. The shape of the charge cloud can be described by a sphere and the electron density is described by a Gaussian distribution. The radius of the spherical charge cloud within the pixel increases due to diffusion, drift, and electrostatic repulsion of the electrons. When a charge cloud is large compared to the pixel size it can split into neighboring pixels. The pixels that contain enough electrons due to this split produce a detector signal.

In order to use the pnCCD detector for the recording of diffraction patterns from water and to resolve speckles the spatial resolution of the detector has to be tuned. Due to the geometry of the WAXS setup (section 5.2.1) the expected size of a speckle is in the order of $S_p = 1\,\mu m$, see equation 2.50. Thus, the spatial resolution for the detection of the x-ray photons on the CCD has to be in the same order.

 To increase the spatial resolution of the detector, the pnCCD detector was used in a Low-Back-Voltage-Mode. By applying a low voltage to the pixel the drift time of the charge cloud was maximized and the size of the charge cloud is increased. In this way the measured signal in neighbor pixels is increased. To evaluate the signal in neighboring pixels a droplet-algorithm has been applied to analyze patterns that considers the detector signal in pixel-clusters. This algorithm defines the hit location of the x-ray photon by analyzing the detector signal in neighbor pixels. To increase the spatial resolution of the detector, the droplet algorithm can only be applied to patterns showing weak intensities corresponding to the detection of
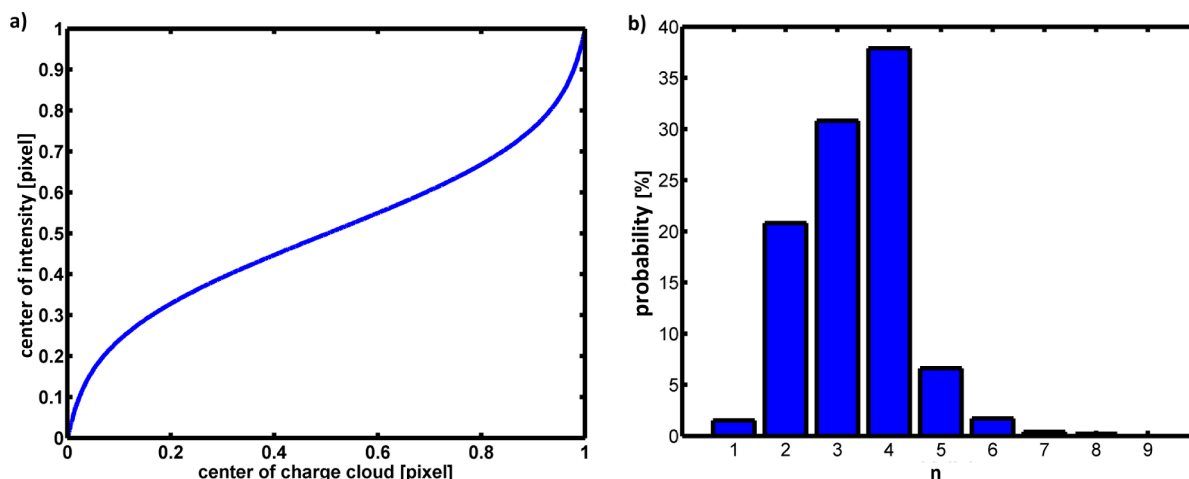
Figure 5.9: a) Dependency of the center of mass of the intensities and the center of the charge cloud. b) Probability distribution [%] for finding n pixels with a detector signal in a 3×3 pixel cluster. The detector was used in a Low-Back-Voltage-Mode to maximize the size of the charge cloud. The statistics were extracted from 20000 single shot diffraction patterns recorded in this experiment.

basically single photons. If two or more photons hit one pixel the charge cloud cannot be used to determine the photon hit locations within the pixel. Therefore, only frames containing single photons has been analyzed.

In the droplet-algorithm the topology of pixel clusters of 3×3 pixels of the diffraction patterns were considered. For example in figure 5.8 two different topologies are shown. To extract the hit location of a photon within a pixel the center of mass of the intensities of the 3×3 pixel cluster were extracted and compared to simulations of the charge cloud. For example, in figure 5.8 b) a so-called quadruple-event is depicted. This means that the charge cloud leads to a detector signal in four pixels. The center pixel has the coordinate $pixel_x = 104$, $pixel_y = 996$, while the center of mass of all nine pixels is at $pixel_x = 104.380$, $pixel_y = 996.382$. Since the charge density in the cloud is not homogeneously distributed the center of mass of the pixel cluster does not represent the center of the charge cloud. The drift, diffusion, and repulsion of the electrons in the charge cloud were simulated to compare the simulated center to the center of mass extracted from the measurements and thus to determine the position of a photon hit, see figure 5.9 a).[44] For the described example the center location of the charge cloud would be at $pixel_x = 104.279$, $pixel_y = 996.283$ in the pixel cluster.

Since the detector was used in a Low-Back-Voltage-Mode the size of the charge cloud is maximized and thus the occurrence of single-events in the 3×3 pixel cluster is minimized. In figure 5.9 b) a histogram of the probability to find n pixels with a detector signal in a 3×3 pixel

---

[44]Private communication, Dr. Martin Huth, PNSENSOR GMBH.

cluster is shown. As can be seen, most of the detected photons leaded to quadruple-events. With this droplet-algorithm the spatial resolution varies between 1 μm and 8 μm depending on the topology of the pixel cluster. The more pixel contribute to the pixel cluster the higher the spatial resolution of the photon detection.[45]

5.2.3 Data treatment

The calibration of the q-scale was performed by using the Bragg reflections of the crystalline hematite particles in a liquid water jet. The volume fraction of the particles in the dispersion was $\phi = 0.01$ vol.%. An average of 2000 single shot diffraction patterns taken on the liquid jet ($\text{jet}_x = -30$ μm) was analyzed for the extraction of the Bragg reflections, see figure 5.10 a). The shadow of the scattering signal comes from the differential pumping stage in front of the detector, see figure 5.6 b). The intense Bragg reflections from the hematite crystal structure where used to calibrate the sample-detector distance d. As the spindle-shaped
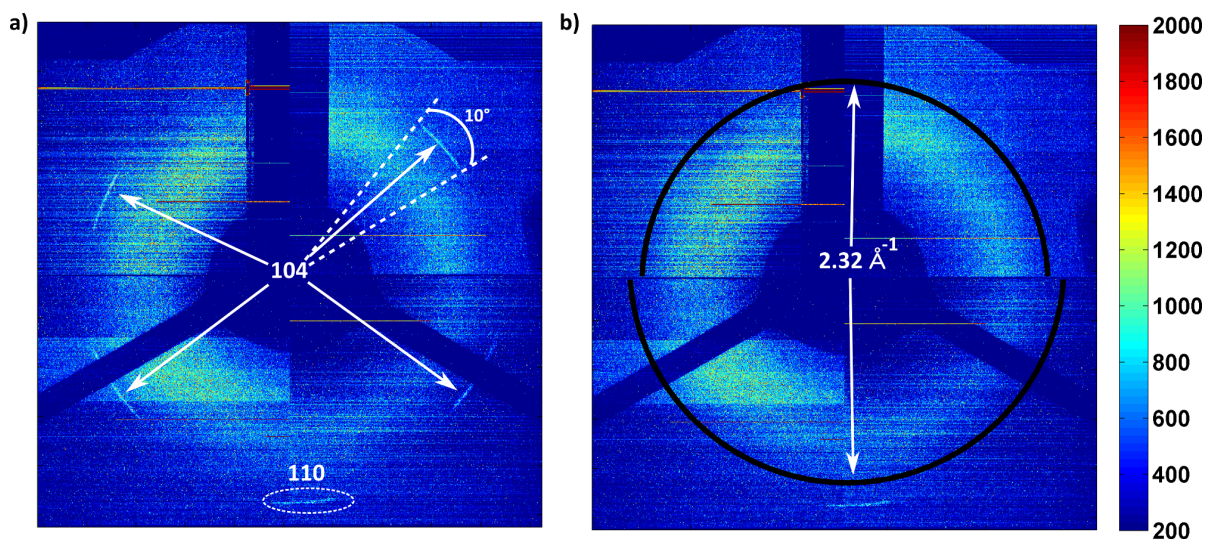
Figure 5.10: Average of 2000 scattering patterns of the hematite dispersion in the liquid jet. a) Bragg reflections of the hematite structure. Segments of the Debye-Scherrer rings are allocated to Miller indices.

particles align with an orientation distribution in the liquid jet a complete Debye-Scherrer ring was not measured, see section 4.3. This indicates that the crystalline structure within the particle is aligned in the liquid jet. The particle alignment leads to four Bragg reflections at $q = 2.32$ Å^{-1} (104) and to two Bragg reflection at $q = 2.54$ Å^{-1} (110), see section 2.3.2. One of these reflections is covered by the differential pumping stage. Within the particle the trigonal

---

[45]Kimmel, N. "Analysis of the charge collection process in solid state X-ray detectors." Dissertation. Universität Siegen, 2008.
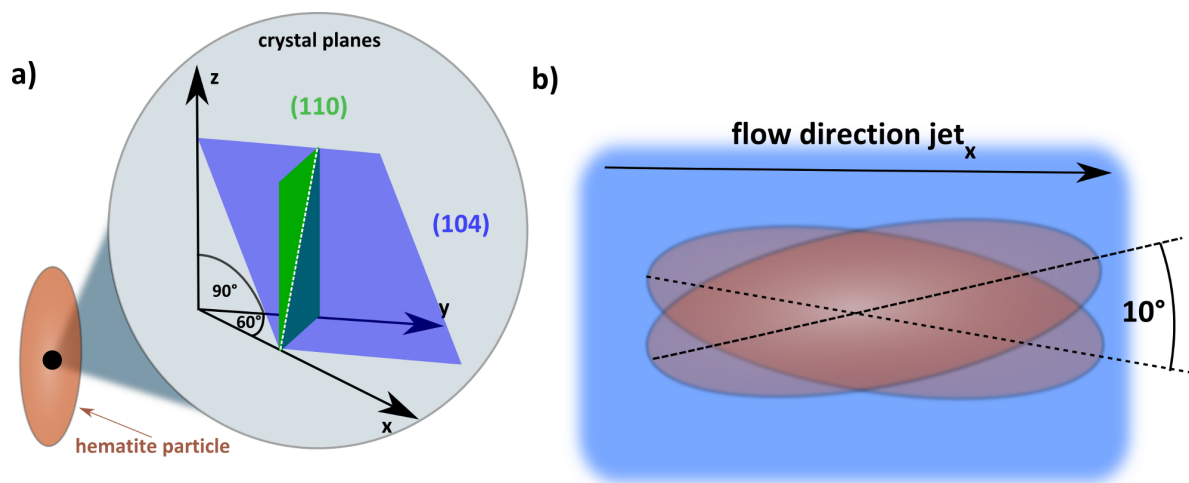
Figure 5.11: Two sketches of hematite particles. a) Crystal planes (110) (green) and (104) (blue) of the hematite structure are shown. The intersection line of this planes is marked by the white dashed line. b) Hematite particles with different orientations.

plane of the rhombohedral lattice cell of the hematite is parallel to the minor axis of the spindle-shaped particle, see figure 5.11 a).[46] Therefore, the azimuthal location of the Bragg reflections on the detector indicate an alignment of the major particle axis parallel to the flow direction of the jet, see figure 5.11 b).[47] The azimuthally width of the Bragg reflections indicate an orientation distribution function of the particle, compare figure 5.10 a) and 5.11 b). The (110) reflection was measured only on the lower CCD, because its signal was covered by the differential pumping stage on the upper CCD. For the calibration of the q-axis on the detector and measurements of the jet-detector distance d the Bragg reflections with the Miller indices (104) were fitted with semi circles, see figure 5.10 b). As the CCDs were separated with different sample detector distances the radius of the semi-circle on the upper panel is larger than the radius of the semi-circle on the lower panel. With the Bragg reflections the distance of the jet to the detector chips was found to be $d_{lo} = 53.3$ mm for the lower CCD and $d_{up} = 48.3$ mm for the upper CCD.

Two typical corrected single shot diffraction patterns from the water jet are shown in figure 5.12. The droplet-algorithm was applied and single photons are depicted by the blue dots. The scattering ring represents the maximum of the first structure factor peak of water at $q = 2\,\text{Å}^{-1}$. The diffraction pattern in figure 5.12 a) shows 2989 detected photons. In the region from $q = 1.99\,\text{Å}^{-1}$ to $q = 2.01\,\text{Å}^{-1}$ 43 photons were measured over 8569 pixels yielding

---

[46]Sugimoto, T. et al. *Colloids Surf. A* **134**, (1998), 265; Blake, R.L. et al. *Am. Mineral* **51**, (1966), 123; Pauling, L. et al. *J. Am. Chem. Soc.* **47**, (1925), 781.

[47]Since the jet properties (flow velocity, jet diameter) differs from the properties of the jet presented in section 4.3.3, the particle alignments in these two jet cannot be compared.
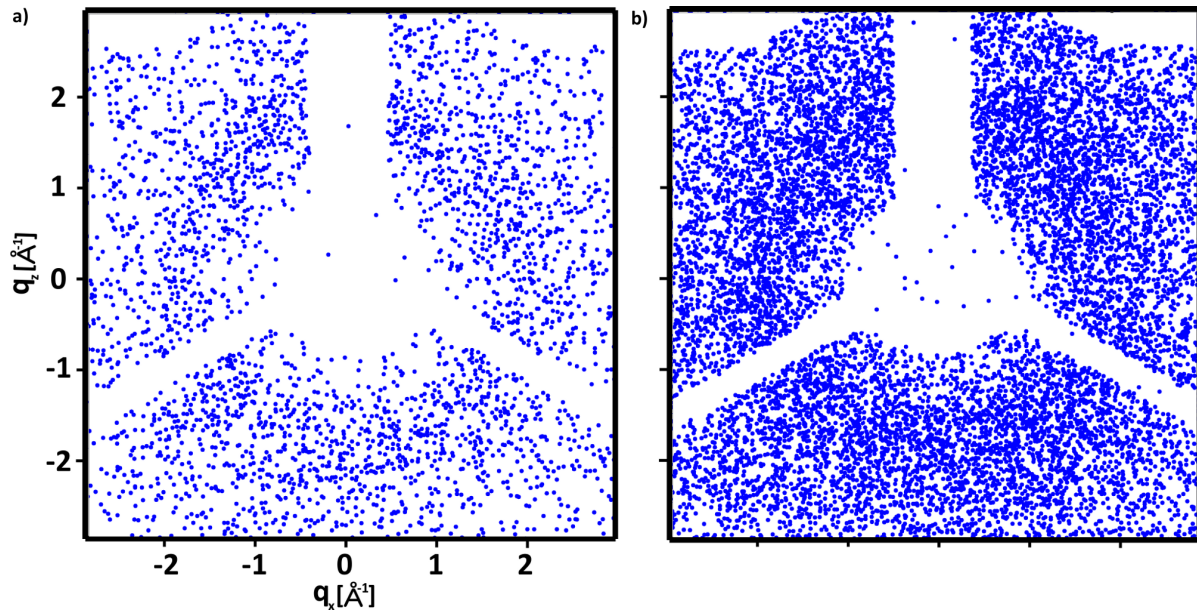
Figure 5.12: Typical scattering patterns taken on the liquid jet ($jet_x = -30\,\mu m$). The blue dots denote the detected photons. The shadows arise from the coverage of the differential pumping stage in front of the CCD chips.

an averaged intensity of $0.0050\,\frac{photons}{pixel}$. The pattern in figure 5.12 b) shows 9913 detected photons. From $q = 1.99\,\mathring{A}^{-1}$ to $q = 2.01\,\mathring{A}^{-1}$ 143 photons were measured. Thus, the average intensity at this region is $0.0167\,\frac{photons}{pixel}$. A statistical analysis based on 1301405 single-shot scattering patterns taken on the liquid jet ($jet_x = -30\,\mu m$) is shown in figure 5.13 a). Due to the intensity fluctuation of the x-ray pulses emitted by the LCLS the amount of detected photons per shot varies.[48] Over 60% of the diffraction patterns measured on the jet show less than 500 detected photons. They show an averaged scattering intensity of $0.00667\,\frac{photons}{pixel}$ from $q = 1.99\,\mathring{A}^{-1}$ to $q = 2.01\,\mathring{A}^{-1}$. At $jet_x = 7\,mm$ 896835 patterns were measured. From these patterns the statistics of the detected photons were extracted, see figure 5.13 b). Over 90% of the single-shot diffraction patterns show less than 500 detected photons. Beside the shot to shot intensity fluctuation of the LCLS

One possible reason for the difference of the two statistics is the hit rate of the x-ray pulses on the water droplets. It is assumable that only a fraction of the x-ray pulses hit the water droplets, while the most of the x-ray pulses hit the continuous flowing liquid jet.

An azimuthal integration of the single shot diffraction patterns measured on the jet is shown in figure 5.14. For the integration only patterns with more than 500 detected photons were considered. The integrated signal is corrected by the horizontal polarization of the x-ray

---

[48] Amann, J. et al. *Nature photonics* **6**, (2012), 693.
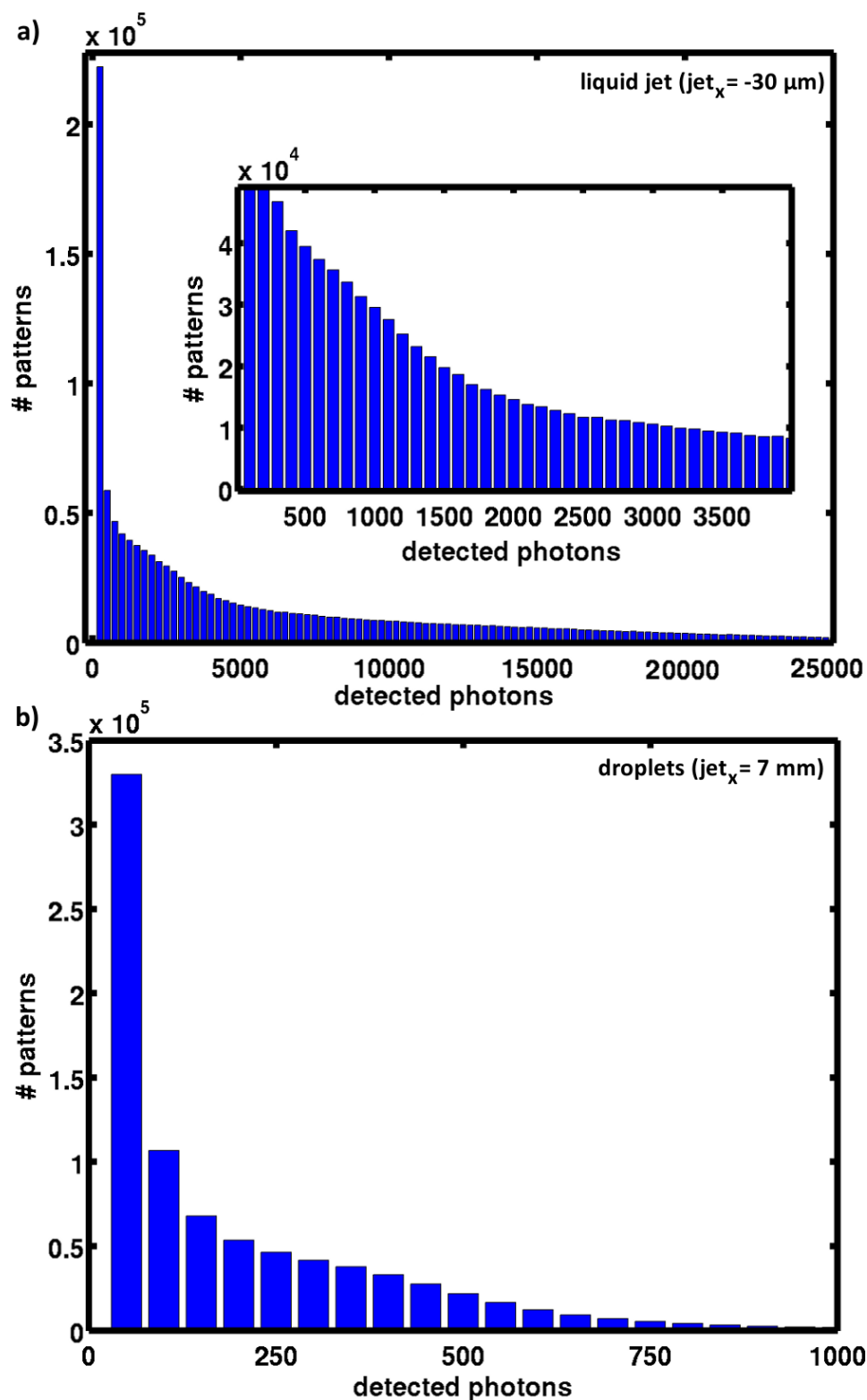
Figure 5.13: Two histograms of patterns as a function of the number of measured photons. a) Measurement on the liquid jet at $jet_x = -30\,\mu m$. b) Measurement on the water droplets at $jet_x = 7\,mm$.
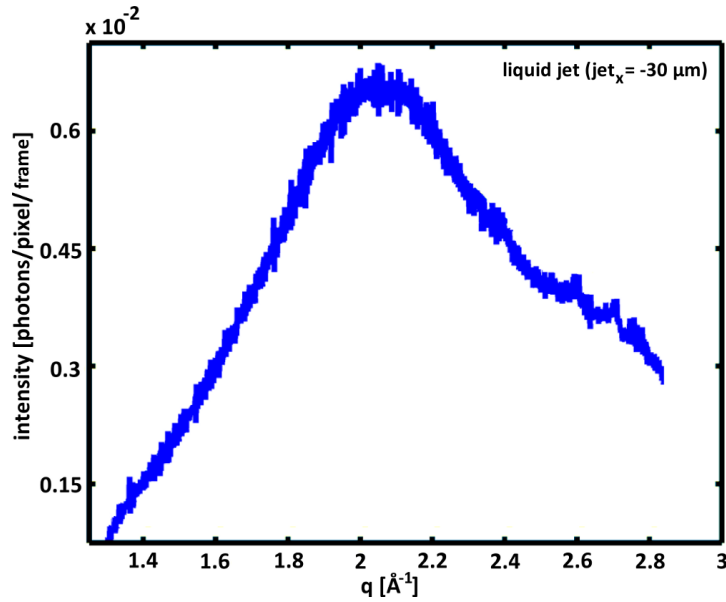
Figure 5.14: Azimuthal integration of the scattering signal of liquid water measured on the liquid jet ($\text{jet}_x = -30\,\mu\text{m}$).

beam, see section 2.1. The first maximum of the structure factor of liquid water leads to a maximum of the scattering signal at $q = 2\,\text{Å}^{-1}$.[49] Furthermore, the characteristic shoulder of the diffraction signal of water at $q > 2\,\text{Å}^{-1}$ is visible.

5.2.4 Discussion

The developed liquid jet setup was tested in this experiment and the experimental parameters were tuned to favor measurements of speckle patterns originating from liquid water. The quality of the single shot diffraction patterns taken on a liquid jet and on water droplets were studied. A droplet algorithm has been applied to increase the spatial resolution of the detector by considering single photon detections, see section 5.2.2. The single shot diffraction patterns show a pronounced fluctuation of the scattered intensity, which could be connected to the shot to shot intensity fluctuation of the LCLS. The average of the measured intensity at $q = 2\,\text{Å}^{-1}$ is $0.00667\,\frac{\text{photons}}{\text{pixel}}$. Since only single photon events were analyzed by the droplet algorithm no intensity contrast β of the measurements could be extracted.[50] The expected contrast β can be calculated using equations 2.52 and 2.53 using the longitudinal coherence length of $\xi_l = 1.14\,\mu\text{m}$[51] and a transverse coherence length of $\xi_t = 17\,\mu\text{m}$ yielding

---

[49]Head-Gordon, T. et al. *Chem. Rev.* **102**, (2002), 2651.
[50]Hruszkewycz, S. O. et al. *Phys. Rev. Lett.* **109**, (2012), 185502; Gutt, C. et al. *Phys. Rev. Lett.* **108**, (2012), 024801; Lehmkühler, F. et al. *App. Cryst.* **47**, (2014), 1315.
[51]Value is valid for $E = 8\,\text{keV}$.

$\beta = 5.1\%$ at $q = 2\,\text{Å}^{-1}$.[52] The expected speckle size can be estimated for the x-ray energy of $E_{\text{x-ray}} = 8.4\,\text{keV}$, the beam size b, the jet-detector distance $d_{\text{lo}} = 53.3\,\text{mm}$ or $d_{\text{up}} = 48.3\,\text{mm}$ and equation 2.50. The beam size is approximated by the average of the horizontal and vertical size to $b = \frac{5\,\mu\text{m} + 3\,\mu\text{m}}{2} = 4\,\mu\text{m}$. On the upper CCD the expected speckle size is $S_p = 1.74\,\mu\text{m}$ and on the lower CCD the expected speckle size is $S_p = 1.85\,\mu\text{m}$. These values are comparable to the spatial resolution obtained with the pnCCD.[53,54]

[52]Robert, A. et al. *J. Phys.: Conf. Ser.* **425**, (2013), 212009; Robert, A. *Website, Beamline XCS.* 2014. URL: `https://portal.slac.stanford.edu/sites/lcls_public/instruments/xcs/Pages/Components.aspx`.

[53]Private communication Dr. Martin Huth.

[54]Kimmel, N. "Analysis of the charge collection process in solid state X-ray detectors." Dissertation. Universität Siegen, 2008.

6 Summary and Outlook

In the framework of this thesis a liquid jet system based on a gas dynamic virtual nozzle (GVDN) has been developed and characterized. The liquid jet system has been used to study complex fluids (dispersion of interacting spherical and non-interacting spindle-shaped colloidal particles) and a molecular fluid (water) via small-angle (SAXS) and wide angle (WAXS) x-ray scattering with coherent x-rays from storage ring (PETRA III) and Free Electron Laser (LCLS) sources.

The liquid jet system comprises a gas dynamic virtual nozzle - GVDN (originally developed by de Ponte et al.[1]), a complex vacuum system and three optical microscopes for jet diagnostics. In the two component borosilicate glass nozzle (GDVN) a liquid is ejected into vacuum and focused by a surrounding gas stream. Depending on the operating conditions a stable $(1\,\mu m - 20\,\mu m$ diameter) jet is produced that breaks up into droplets after typically $50\,\mu m - 250\,\mu m$ from the nozzle tip. This is visualized quantitatively and time resolved by high resolution optical microscopy under continuous or stroboscopic illumination. The gas focused liquid is subject to considerable shear forces and shear rates in excess of $\dot{\gamma} = 10^4\,Hz$ that can be made visible and calibrated by adding colloidal particles to the liquid. This allows the jet also to be used as a rheometer. Once the jet breaks up into droplets these expand into vacuum and cool down allowing to study liquids containerless even in the supercooled regime. The developed vacuum system ensures operation of the liquid jet system at typically $p_{vac} = 10^{-3}\,mbar$ and vacuum compatibility with the involved photon source and detector systems such as the pnCCD.

In a first feasibility experiment the flow properties of a simple Rayleigh jet (without gas stream) was studied in a by Small Angle X-ray (SAXS) scattering on colloidal suspensions at the BW4 beamline at DORIS III and P10 beamline at PETRA III. A concentrated suspension (34 wt%) of charge stabilized silica (Ludox Sigma-Aldrich) in water was investigated in the center and close to the sides of a 100 μm diameter jet and compared to a suspension measured in a capillary. The results show a nearly unperturbed SAXS pattern in the center while the dispersion is strongly sheared close to the sides of the jet. The SAXS patterns indicate an

---

[1]Deponte, D.P. et al. *J. Phys. D: Appl. Phys.* **41**, (2008), 195505.

about 15 % shear induced compression of the dispersion in one direction and an expansion in the orthogonal direction. The patterns appear to be symmetric about the center thus indicating that the shear flow is also symmetric about the center axis of the jet. This result clearly shows the feasibility of nano-rheology experiments with jet systems.

This result also motivated a detailed study of the rheological properties of a jet formed by a GDVN with a dilute $\phi = 0.1$ vol% colloidal model dispersion consisting of spindle-shaped hematite particles in water. This dispersion was characterized by SAXS in a magnetic field and the analysis yielded particles with a long axis of 54 nm, an aspect ratio of 3.3 and a poly-dispersity of 9 %. The analysis was carried out with a program package that was developed in the framework of this thesis. This dispersion was studied in a 15 μm diameter jet formed by a GDVN at distances between 100 μm to 1000 μm form the nozzle with perpendicular steps of 1 μm. A total of $10 \, x25$ spots in the jet were analyzed yielding a two dimensional orientation map of the spindle-shaped particles. Very close (100 μm) to the nozzle the spindle shaped particles are aligned with the long axis parallel to the flow direction of the jet. This alignment is preserved along the sides of the jet. On axis there is a change of the particle orientation. Already 200 μm downstream from the nozzle a 90° rotation of the spindles is observed. The long axis is pointing perpendicular to the jet. This orientation is maintained on axis for all distances measured. Using known or estimated parameters for the jet parameters it is possible to estimate a shear rate of $\dot{\gamma} = 5 \cdot 10^4$ Hz. This value supersedes shear-rates known from conventional rheometers by $1-2$ orders of magnitude. The data show also a region surrounding the center portion of the jet in which at least two different orientations of the spindles can be observed.

The data show that the liquid jet system can give access to microstructures under high shear forces and large deformation rates that are absent in the equilibrium system. Prior to a systematic use the performance and reproducibility of the nozzles has to be improved. A recently published manufacturing process of gas dynamic nozzles on a microfluidic chip is a promising route to produce nozzles with the necessary performance specifications.[2]

In a second experimental campaign a wide angle x-ray scattering experiment on liquid and supercooled water was carried out at the free electron laser LCLS at SLAC. The experimental configuration involved the GDVN system producing a water jet of about 3.6 μm diameter. Data in the supercooled regime were taken by measuring the scattering from water droplets at distances between 7 mm and 25 mm from the nozzle tip. The detector system was a 120 Hz compatible pnCCD with two modules of 1024×512 pixels of 75 μm $\times$ 75 μm size. In order

---

[2]Trebbin, M. et al. *Lab on a Chip* **14**, (2014), 1733.

to subtend the first structure factor peak of water ($q = 2\,\text{Å}^{-1}$) the detector needed to be placed 53 mm away from the jet. A specially designed differentially pumped seal was developed[3] to separate the pressure in the jet chamber ($p_{vac} = 10^{-3}$ mbar) from the pressure in the chamber housing of the detector ($p_{vac} = 10^{-6}$ mbar). In order to verify weather or not a coherent scattering experiment on water could be carried out the detector had to be configured in a high resolution, speckle resolving configuration. By running the detector in the special Low-Back-Voltage-Mode configuration a spatial resolution $< 8\,\mu$m was achieved. Over one million coherent diffraction patterns were taken on the jet at 170 μm distance from the nozzle tip. The average intensity at the first structure factor peak of about $0.0067\,\frac{\text{photons}}{\text{pixel}}$. Furthermore, coherent diffraction patterns were taken on the water droplets at different distance (7 mm, 10 mm, 15 mm, 20 mm, 25 mm) from the nozzle tip. Since the single shot data taken on droplets arise from a distribution of droplet sizes and thus temperatures a complex deconvolution algorithm is necessary for a sorting of the data. First results show that this is possible.

The experience shows also that the liquid jet systems needs control of droplet size and thus temperature as well as hit control. This mandates the implementation of a drop-on-command technology probably by a piezo controlled droplet injection system.[4] These developments were beyond the scope of the thesis work but have been initiated and will be implemented for the use of the device at the European XFEL.

---

[3]The differentially pumped seal was developed by the MAX Plank Institute Intelligente Systeme, Stuttgart.
[4]Weierstall, U. et al. *Exp. Fluids* **44**, (2008), 675; Deponte, D.P. et al. *J. Phys. D: Appl. Phys.* **41**, (2008), 195505.

Appendix

A.1 Nozzle production

In this appendix the production of a gas dynamic virtual nozzle (GDVN) is explained. The description follows the work of Deponte et al.[1] A gas dynamic virtual nozzle consists of five parts:

1. A glass capillary made of brosilicate glass with inner diameter $d_i = 0.75\,\text{mm}$ and outer diameter $d_o = 1\,\text{mm}$.[2] Out of this capillary the nozzle tip will be formed.

2. A capillary micro tube with inner diameter $d_i = 25\,\mu\text{m}$ and outer diameter $d_o = 150\,\mu\text{m}$.[3] The length of the tube can vary between $l = 20\,\text{cm}$ and $l = 40\,\text{cm}$. As it is used to guide the liquid flow to the nozzle, it is advisable to reduce the flow resistance by using a short tube.

3. A second capillary micro tube with inner diameter $d_i = 100\,\mu\text{m}$ and outer diameter $d_o = 375\,\mu\text{m}$.[4] This tube is used to guide the gas to the nozzle tip. The length should be $l > 10\,\text{cm}$. Since the flow resistance of gas is much smaller than the flow resistance of fluids the length can be $l = 1\,\text{m}$.

4. A metal tube with inner diameter $d_i = 1.15\,\text{mm}$ and outer diameter $d_o = 1.59\,\text{mm}$. The length of the tube is $l = 5\,\text{cm}$.[5] It is used to stabilize the nozzle.

5. A micro fitting.[6] This part is needed to connect the nozzle to an holder in a chamber. Thus, the type of the screw thread depends on the connection at the nozzle holder. It needs to be attachable to the metal tube.

---

[1]Deponte, D.P. et al. *J. Phys. D: Appl. Phys.* **41**, (2008), 195505.
[2]Sutter Scientific Instruments, B100-75-10.
[3]Polymicro Technologies, TSP025150.
[4]Polymicro Technologies, TSP100375.
[5]Upchurch Scientific, U-145.
[6]Upchurch Scientific, F-120x.
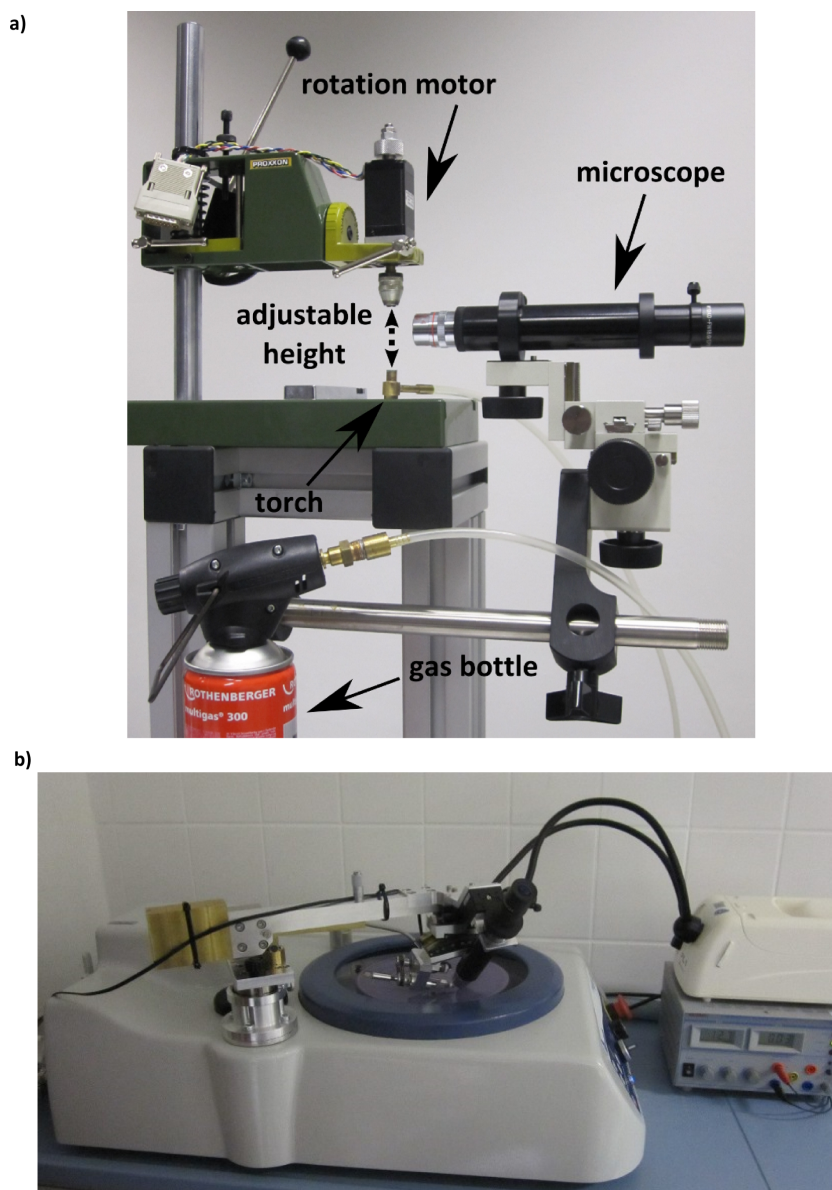
Figure A.1: a) Photography of a melting table consisting of an adjustable rotation stage located above a torch. b) Photography of grinding machine equipped with a grinding arm to hold micro tubes.
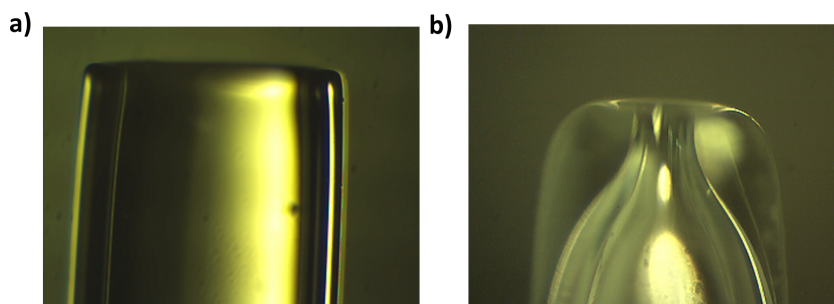
Figure A.2: Photographs of the glass plenum before (a) and after (b) the melting procedure.

Three different workplaces are necessary for the production of a GDVN. The first workplace is a standard microscope[7]. It is needed to check the status of the GDVN after each work step. The second workplace is a melting table consisting of a rotation stage mounted over a torch, see figure A.1 a). As gaseous fuel a mixture of Butan (60%) and Propan (40%)[8] is needed. The third place is a grinding machine[9] equipped with two different abrasive wheels, see figure A.1 b). One is coated with silica particles[10] of diameters of 30 µm and the other one is a polish paper[11]. The grinding machine is needed to grind micro tubes and glass capillaries. For these purpose a custom-made grinding arm was developed to grind tubes at different angles relative to the abrasive wheel. The grinding arm provides a motorized rotation of the tube around it axis. This ensures a uniform grinding result around the tube axis. All tubes and glasses need to be cut by a diamond file[12]. With these three workplaces the work flow can be divided in four different steps:

1. **Preparation of the glass plenum**
   The plenum is made from the glass tube. The length of the glass plenum can vary from $l = 1\,cm$ to $l = 3\,cm$. The glass plenum is prepared by melting it at the melting table. To form the wanted shape of the glass plenum the glass tube has to rotate over a flame with rounds per minute between 1800 and 2700.[13] Microscope images of the glass tube before and after this work procdure are shown in figure A.2. After the melting process the exit hole of the glass is shrunk to a micro channel. The diameter of the micro channel should be smaller than the outer diameter of the micro tube, that is used for the liquid supply ($d_o = 150\,µm$).

---

[7]Edmund Optics, E-Zoom6
[8]Rothenberger Multigas 300
[9]Bühler Gmbh, MetaServ 250
[10]Bühler Gmbh, Diamond Grinding Disc 41-6408D 8in
[11]Bühler Gmbh, Multiflok 8in, 41-3476
[12]Heson Diamantfeilen Gmbh, S 2252 D64
[13]Schitzer, G.L. *Rev. Sci. Inst.* **62**, (1991), 2765.
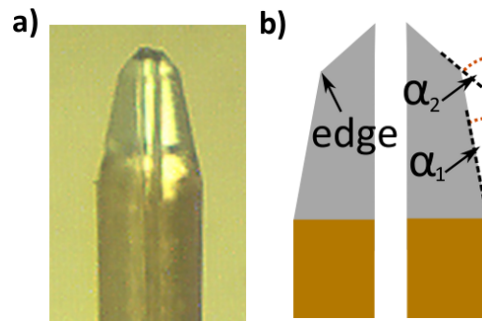
Figure A.3: a) Microscope image of a grinded micro tube. b) Sketch of the grind micro tube.

2. **Preparation of the micro tube**

   In this step the micro tube, that is used for the liquid supply, is grinded using the grinding machine. It has to be equipped with the polish paper and the grinding arm is needed, see figure A.1 b). As polishing fluid distilled water is sufficient to reach good grinding results. The tip has to be sharped with two different angles, α_1 and α_2. The micro tubes in this work were grinded with angles $\alpha_1 = 14°$ and $\alpha_2 = 43°$. One example of a grind micro tube is shown in figure A.3. The grinding procedure leads to an edge at the tube tip. At this edge the micro tube has to contact the entrance of the micro channel inside of the plenum.

3. **Adaption**

   The third work procedure is to check if the micro tube fits into the glass plenum. This is shown in figure A.4 a). If the tube fits correctly into the glass plenum the micro tube contacts the glass plenum at its edges and the sharped tip sticks into the entrance of the micro channel. In this way a small gap between the sharped tube tip and the micro channel is formed, see figure A.4 b). If this position of the micro tube is reached the glass plenum has to be cut off at its tip. This has to be done with the grinding machine and the silicon coated abrasive wheel. After this step the tip of the glass plenum should be flat, see figure A.4 b).

4. **Assembling**

   As final step all parts have to be glued to the metal tube. During the glue process the grinded micro tube has to stick at the entrance of the micro channel, while the micro tube for the gas supply has to end in the metal tube. Both tubes are glued to one end of the metal tube. The glass plenum has to be glued at the other end of the metal tube. After the glue procedure the micro tight fitting has to be attached to the metal tube. The final result is shown in figure A.5.
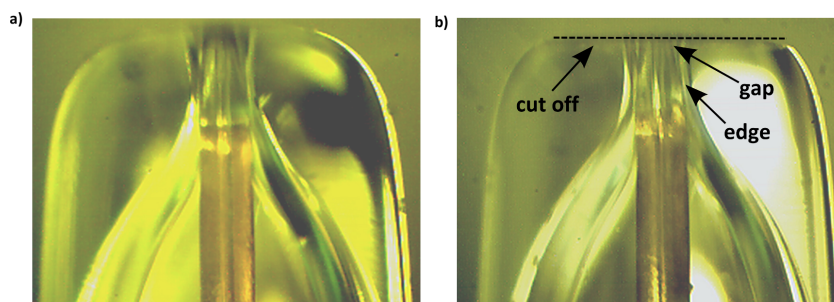
Figure A.4: Two microscope photographs of the glass plenum with the micro tube inside. a) Photo of the glass plenum with micro tube before the cut off of the plenum. b) Photo of the micro tube with a cutted glass plenum.
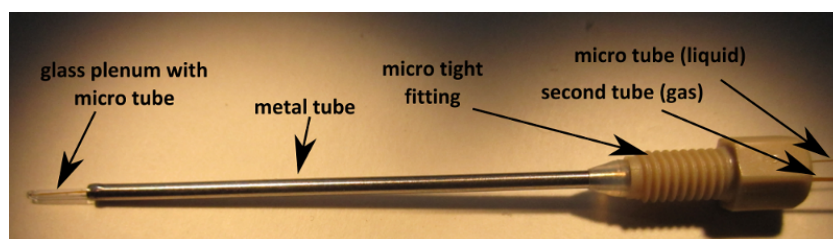
Figure A.5: Photography of the nozzle after the glue process.

In the framework of this thesis every produced nozzle was tested and characterized with distilled water. For this purpose a test station were constructed, see figure A.6. The work principle of the test station is shown in figure A.7. Two types of gases (He, N_2) are needed. For a better control of the gas pressures two pressure regulators[14] were used. These regulators are capable to work with pressures up to $p = 70$ bar. They are needed to ensure a constant gas pressure at the nozzle. Water is located in a reservoir and becomes pressurized by the nitrogen gas. Helium is used as focusing gas and is guided directly to the nozzle tip. The tubes for the water and the helium are connected to the micro tubes at the nozzle, see figure A.5 b). The nozzle tip is located in vacuum present in the test chamber, while the other end of the nozzle is in atmosphere. A scroll pump[15] evacuate this chamber down to a pressure of $p_{\mathrm{vac}} = 0.05$ mbar without liquid jet and with $p_{\mathrm{vac}} = 0.5$ mbar.

To monitor the liquid jet a microscope is mounted at the chamber. This is not visible in the figures. It offers a view on the nozzle tip through a window at the chamber. To monitor the liquid jet, it is illuminated from behind of the chamber, see figure A.6.

---

[14]Therhorst B.V., proportional Air electronic regulators: 17.60GP10G1000EE
[15]Edwards Gmbh, XC35I
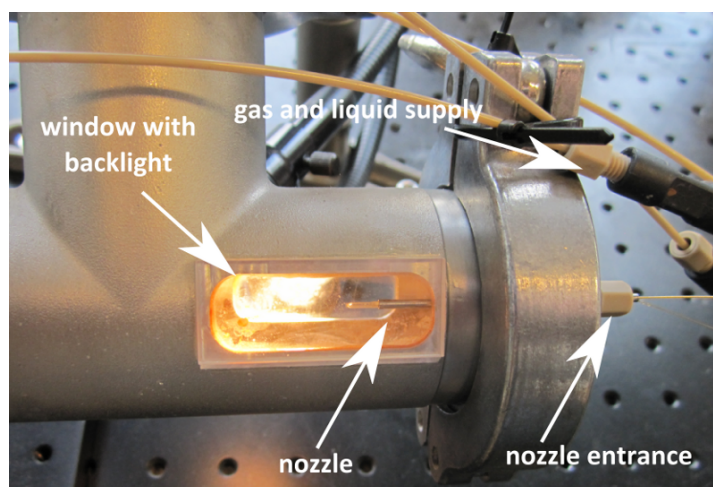
Figure A.6: Close up of the vacuum chamber with a GDVN inside.
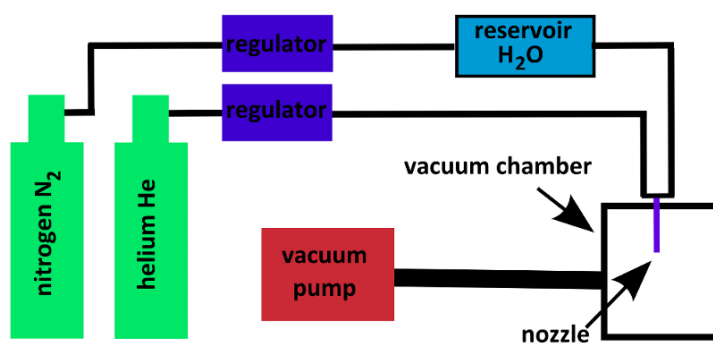
Figure A.7: Up: Sketch of the test station setup. Bottom: Picture of the test station. The important parts are pointed out.
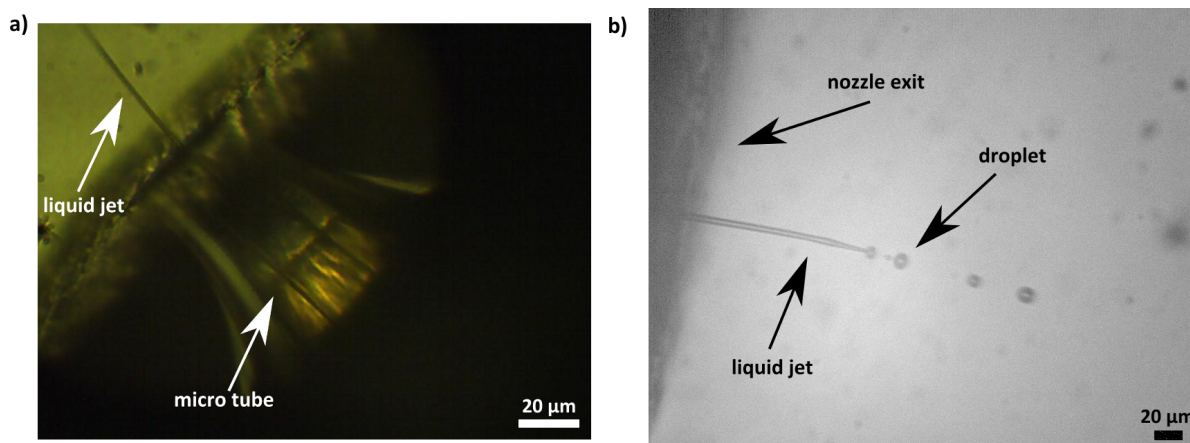
Figure A.8: Two microscope photographs showing a liquid jet. The photos were taken with different exposure times t_e and different cameras. a) $t_e = 10\,\mathrm{ms}$ b) $t_e = 300\,\mathrm{ns}$.

For testing the nozzles and characterization of the produced liquid jets microscope images with different exposure times were taken. In figure A.8 a) the microscope image was recorded with an exposure time of $t_e = 10\,\mathrm{ms}$. It shows a liquid jet at the nozzle tip. The break up process and the droplets are not visible because the exposure time t_e was to long compared to the motion of the liquid jet. The diameter of the shown jet can be quantified to $d_{\mathrm{jet}} = 3\,\mu\mathrm{m}$. For a static view on a liquid jet exposure times t_e of a few hundred ns are necessary. In figure A.8 b) a microscope image recorded with an exposure time of $t_e = 200\,\mathrm{ns}$ is shown. The liquid jet and the droplets are visible and the liquid jet is not smeared out. The break up point of the liquid jet is visible and the break up length can be quantified to $L = 150\,\mu\mathrm{m}$. The diameter of the liquid jet was determined to $d_{\mathrm{jet}} = 7\,\mu\mathrm{m}$.

Recently, a modification of the described nozzle design were published.[16] In this work the authors discussed a new shape of the grinded micro tube. This modification is promising to form jets of diameter below $d_{\mathrm{jet}} < 1\,\mu\mathrm{m}$. More recently a new production method for GDVNs was published.[17] With this method the shape of the nozzle should be standardized and the reproducibility of nozzles should be ensured.

---

[16]Acero, A.J. et al. *J. Micromech. Microeng.* **23**, (2013), 065009.
[17]Trebbin, M. et al. *Lab on a Chip* **14**, (2014), 1733.

A.2 Numerical calculation of the form factor of spindle-shaped particles

The processing time for the form factor of spindle shaped particles with an orientation distribution function (ODF) is typically with an standard office computer about one day. The reason is the complexity of the mathematical formula, see equations 2.22 and 2.21, respectively. To decrease the calculation time a lookup table was used. This is an saved array that replaces run time calculations in a program. Using the saved lookup table instead of run time calculations saves processing time. In this appendix the preparation of the lookup table and the numerical calculation of the form factor is schematically described.

The equation to calculate is the form factor of spindle-shaped particles with an ODF is given by[18]

$$P_{\text{dist}}(q,\zeta,R_1,R_2,Z,\nu) = \int_0^{2\pi} \int_0^{\pi} f(\theta_g,\phi_g) P_{\text{poly}}(q,\zeta,R_1,R_2,Z,\nu) \sin\theta_g d\theta_g d\phi_g. \quad (A.1)$$

For numerical calculations $P_{\text{poly}}(q,\zeta,R_1,R_2,Z,\nu)$ is used for the lookup table. Thus, P_{poly} has to be calculated for a set of q and ζ values (equation 2.13). The example, which is shown in this appendix, was calculated using $R_1 = 40\,\text{nm}$, $R_2 = 170\,\text{nm}$, $\nu = 4$, and $Z = 9999$. Since the angle $\zeta \in \left\{0 \ldots \frac{\pi}{2}\right\}$, ninety equidistant values between 0 and $\frac{\pi}{2}$ were used for the lookup table. For each ζ value the function P_{poly} was calculated from $q = 0.001\,\text{nm}^{-1}$ to $q = 0.7\,\text{nm}^{-1}$ in steps of $\Delta q = 0.001\,\text{nm}^{-1}$. The results were saved in an array and the form factor of particles with an ODF can be calculated.

To calculate the form factor the ODF $f(\theta_g,\phi_g)$ has to be set. This was done with an two dimensional Gaussian distribution

$$f(\theta_g,\phi_g) = \exp\left(-1 \cdot \left(\frac{\left[\theta_g - \theta_{g,c}\right]^2}{\sigma_{\theta,s}} + \frac{\left[\phi_g - \phi_{g,c}\right]^2}{\sigma_{\phi,s}}\right)\right), \quad (A.2)$$

The shown example was calculated using the standard deviations $\sigma_{\theta,s} = 1000\,\text{rad}$ and $\sigma_{\phi,s} = 0.149\,\text{rad}$. The center locations to $\theta_{g,c} = 0$ and $\phi_{g,c} = \frac{\pi}{2}$. With these values the ODF is plotted in figure A.9. The resolution of the calculation is defined by the size of an array. In this example its size is 1000×1000 pixels. For each pixel the wave vector transfer q and the angle θ_q were calculated, see figure A.10. For this purpose it was assumed that $q = 0\,\text{nm}^{-1}$ is at

---

[18]The mathematical formula is derived in section 2.2.2.
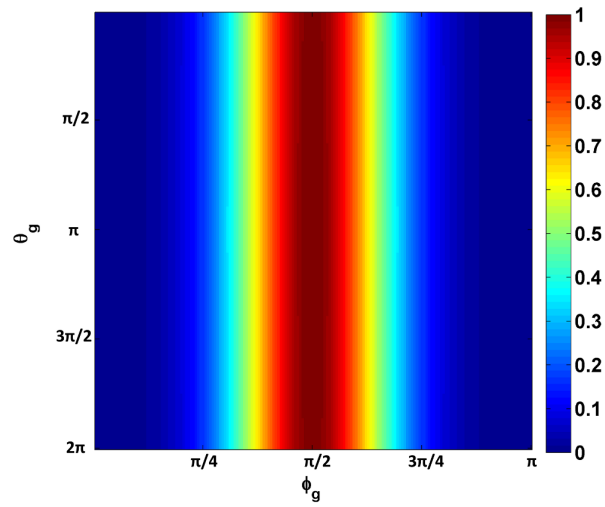
Figure A.9: Orientation distribution functions (ODF) with $\sigma_{\theta,s} = 1000\,\mathrm{rad}$ and $\sigma_{\phi,s} = 0.149\,\mathrm{rad}$ (equation A.2).
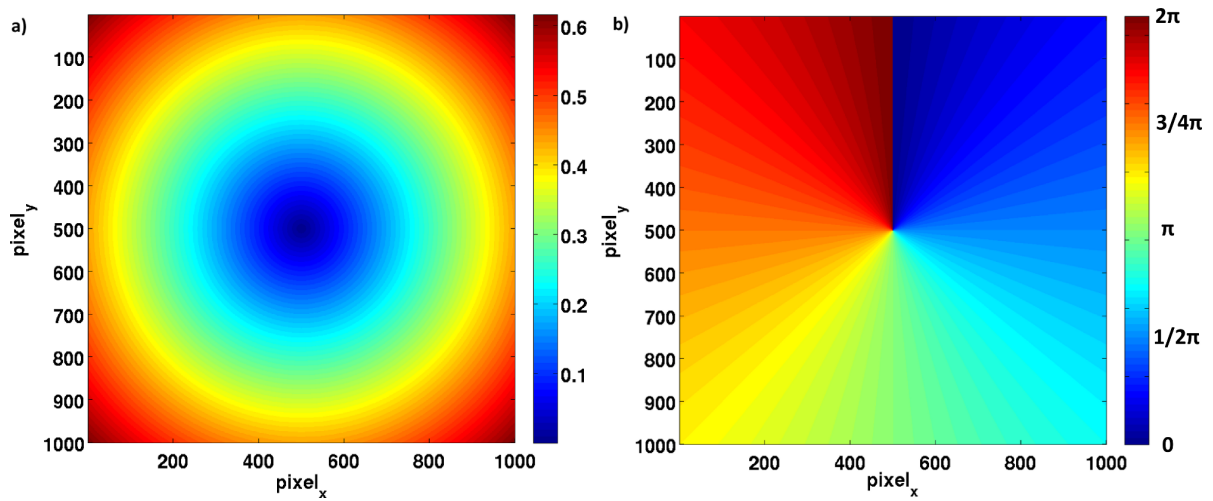
Figure A.10: Two arrays with 1000×1000 pixels. The center location is at $\mathrm{pixel}_x = 500\,\mu\mathrm{m}$ and $\mathrm{pixel}_y = 500\,\mu\mathrm{m}$ a) Array with wave vector transfer q. The unit of the scale is nm^{-1}. b) Array with angle θ_q. The unit of the scale is radiant.
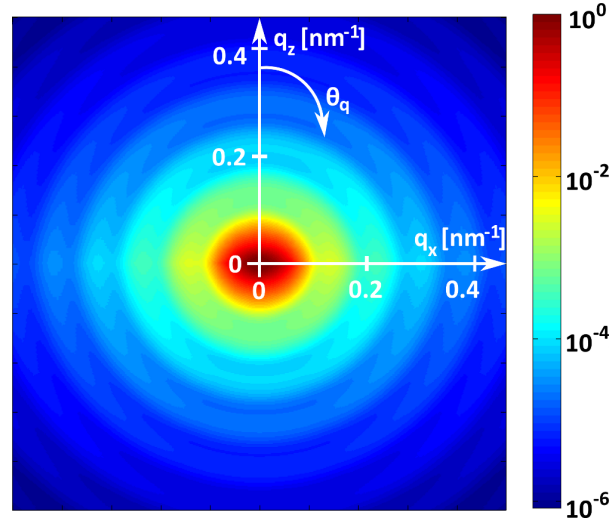
Figure A.11: Form factor of spindle-shaped particles with an ODF (FWHM= 0.35 rad). The scattering strength is normalized to its maximum at $q_x = 0\,\text{nm}^{-1}$ and $q_z = 0\,\text{nm}^{-1}$

$pixel_x = 500$, $pixel_y = 500$. The calculation was done for each pixel corresponding to q and θ_q values. The integrals in equation A.1 are solved with a loop over the number of pixels shown in figure A.9. The ζ value for P_{poly} was calculated by using

$$\cos(\zeta) = \cos\theta_q \cos\theta_g + \sin\theta_q \sin\theta_g \cos\phi_g. \tag{A.3}$$

With the resulting ζ value P_{poly} was taken from the lookup table. In case if P_{poly} does not exist for the certain ζ and q values, P_{poly} was interpolated. This was done by averaging P_{poly} for a higher and a lower ζ or q value in the lookup table. The resulting form factor is shown in figure A.11.

Bibliography

Acero, A.J., Ferrera, C., Montanero, J.M., and A.M.Gañán-Calvo. *J. Micromech. Microeng.* **22**, (2012), 065011.

Acero, A.J., Rebollo-Muñoz, N., Montanero, J.M., and Gañán-Calvo, A.M. *J. Micromech. Microeng.* **23**, (2013), 065009.

Als-Nielsen, J. *Elements of Modern X-Ray Physics*. Wiley and Sons, Ltd, 2001.

Amann, J., Berg, W., Decker, F.J., Ding, Y., Emma, P., Feng, Y., Frisch, J., Fritz, D., Hastings, J., Huang, Z., Krzywinski, J., Lindberg, R., Loos, H., Lutman, A., Nuhn, H.D., Ratner, D., Rzepiela, J., Shu, D., and Zhu, D. *Nature photonics* **6**, (2012), 693.

A.M.Gañán-Calvo, Herrada, M.A., and Montanero, J.M. *Phys. Fluids* **26**, (2014), 061701.

Angell, C.A. *Science* **319**, (2008), 582.

Angell, C.A., Oguni, M., and Sichina, W.J. *Physica A* **106**, (1982), 260.

Aniskin, V., Mironov, S., and Maslov, A. *Microfluid Nanofluid* **14**, (2013), 605.

Aniskin, V.M., Maslov, A.A., and Mironov, S.G. *Tech. Phys. Lett.* **37**, (2011), 1046.

Aquila, A. and al., et. *Opt. Exp.* **20**, (2012), 2706.

Avila, M., Willis, A., and Hof, B. *J. Fluid Mech.* **646**, (2010), 127.

Bakel, N.A., Robert, A., Sirkorski, M., Ford, C., Beveren, V., Heijden, B., and Beuzekom, M. *J. Phys.: Conf. Ser.* **425**, (2013), 062011.

Ball, P. *Chem. Rev.* **108**, (2008), 74.

Batchelor, G.K. *An Introduction to Fluid Dynamics*. Cambridge University Press, 1967.

– . *J. Fluid Mech.* **83**, (1977), 97.

Beizaie, M. and Gharib, M. *Exp. Fluid* **23**, (1997), 130.

Bihannic, I., Baravian, C., Duval, J.F.L., Paineau, E., Meneau, F., Levitz, P., Silva, J.P., Davidson, P., and Michot, L.J. *J. Phys. Chem. B.* **114**, (2010), 16347.

Blake, R.L., Hessevick, R.E., Zoltai, T., and Finger, L.W. *Am. Mineral* **51**, (1966), 123.

Bogan, M.J., Starodub, D., Hampton, C.Y., and Sierra, R.G. *J. Phys. B: Mol. Opt. Phys.* **43**, (2010), 194013.

Boutet, S. and al., et. *Science* **337**, (2012), 362.

Brader, J.M. *J. Phys.: Condense Matter* **22**, (2010), 363101.

Brenner, H. *Int. J. Multiphaseflow* **1**, (1974), 195.

Brenner, M.P., Eggers, J., Joseph, K., Nagel, S.R., and Shi, X.D. *Phys. Fluids* **9**, (1997), 1573.

Bronstein, I.N., Semendjajew, K.A., Musiol, G., and Mühlig, H. *Taschenbuch der Mathematik*. Frankfurt am Main: Harri Deutsch GmbH, 2005.

Brovchenko, I. and Oleinikova, A. *J. Chem. Phys.* **124**, (2006), 164505.

– . *Chem. Phys. Chem.* **9**, (2008), 2660.

Brown, E., Forman, N.A., Orellana, C.S., Zhang, H., Maynor, B.W., Betts, D.E., DeSimone, J.M., and Jaeger, H.M. *Nature Mat.* **9**, (2010), 220.

Brown, E. and Jaeger, H.M. *Science* **333**, (2011), 1230.

Carlo, D.D. *Lab Chip* **9**, (2009), 3038.

Chapman, H.N. and al., et. *Nature* **470**, (2011), 73.

Cheng, X., McCoy, J.H., Israelachvili, J.N., and Cohen, I. *Science* **333**, (2011), 1276.

Clark, G.N.I., Cappa, C.D., Smith, J.D., Saykally, R.J., and Head-Gordon, T. *Mol. Phys.* **11**, (2010), 1415.

Clark, G.N.I., Hura, G.L., Teixeira, J., Soper, A.K., and Head-Gordon, T. *PNAS* **107**, (2010), 14003.

Clarke, N.S. *Mathematika* **12**, (1966), 51.

Conrad, Heiko. "Dynamics of colloids in molecular glass forming liquids studied via X-ray photon correlation spectroscopy." Dissertation. Universität Hamburg, 2014.

Corradini, D., Rovere, M., and Gallo, P. *J. Chem. Phys.* **132**, (2010), 134508.

Couder, Y., Chomaz, J.M., and Rabaud, M. *Physica D* **37**, (1989), 384.

D., Starodub et al. *Nature Com.* **3**, (2012), 1276.

Debendetti, P.G. and Stanley, H.E. *Phys. Today* **56**, (2003), 40.

Denisov, D., Dang, M.T., Struth, B., Wegdam, G., and Schall, P. *Sci. Rep.* **3**, (2013), 1631.

Deponte, D.P., Doak, R.B., Hunter, M., Liu, Z., Weierstall, U., and Spence, J.C.H. *Micron* **40**, (2009), 507.

Deponte, D.P., Hunter, M., Doak, R.B., McKeown, J.T., Weierstall, U., and Spence, J.C.H. *Microsc. Microanal.* **14**, (2009), suppl 2.

Deponte, D.P., Weierstall, U., Schmidt, K., Warner, J., Starodub, D., Spence, J.C.H., and Doak, R.B. *J. Phys. D: Appl. Phys.* **41**, (2008), 195505.

Eggers, J. *Phys. Rev. Lett.* **71**, (1993), 3458.

– . *Rev. Mod. Phys.* **69**, (1997), 865.

– . *Phys. Fluids* **7**, (1994), 941.

Eggers, J. and Villermaux, E. *Rep. Prog. Phys.* **71**, (2008), 036601.

Einstein, A. *A. Ann. Phy.* **19**, (1906), 289.

– . *A. Ann. Phy.* **34**, (1911), 591.

Emma, P. et al. *Nat. Photonics* **4**, (2010), 641.

Eroglu, H. and Chigier, N. *Phys. Fluids A* **3**, (1991), 303.

Errington, J.R. and Debenedetti, P.G. *Nature* **409**, (2001), 318.

Fanetti, S., Lapini, A., Pagliai, M., Citroni, M., Donato, M. Di, Scandolo, S., Righini, R., and Bini, R. *J. Phys. Chem. Lett.* **5**, (2014), 235.

Faubel, M., Schlemmer, S., and Toennies, P.J. Z. *Phys. D* **10**, (1988), 269.

– . *J. Electron Spectrosc. Relat. Phenom.* **95**, (1998), 159.

Faubel, M., Steiner, B., and Toennies, J.P. *J. Chem. Phys.* **106**, (1997), 9013.

Foss, D.R. and Brady, J.F. *J. Fluid Mech.* **407**, (2000), 167.

Franzese, G. and Stanley, H.E. *J. Phys.: Condense Matter* **19**, (2007), 205126.

French, J.B., Etkin, B., and Jong, R. *Anal. Chem.* **66**, (1994), 685.

Fridrikh, S.V., Yu, J.H., Brenner, M.P., and Rutledge, G.C. *Phys. Rev. Lett.* **90**, (2003), 144502.

Gañán-Calvo, A.M. *Phys. Rev. Lett.* **80**, (1998), 285.

Gañán-Calvo, A.M., Deponte, D.P., Herrada, M.A., Spence, J.C.H., Weierstall, U., and Doak, R.B. *Small* **6**, (2010), 822.

Gañán-Calvo, A.M., Ferrera, C., and Montanero, J.M. *J. Fluid Mech.* **670**, (2011), 427.

Gañán-Calvo, A.M., Ferrera, C., Torregrosa, M., Herrada, M.A., and M.Marchand. *Microfluid Nanofluid* **11**, (2011), 65.

Gañán-Calvo, A.M., Montanero, J.M., Martin-Banderas, L., and Flores-Mosquera, M. *Adv. Drug. Del. Rev.* **65**, (2013), 1447.

Gañán-Calvo, A.M., Rebollo-Munoz, N., and Montanero, J.M. *New J. Phys.* **15**, (2013), 033035.

Garrett-Roe, S., Perakis, F., Rao, F., and Hamm, P. *J. Phys. Chem. B* **115**, (2011), 6976.

Gharib, M. and Beizaie, M. *Bull. Am. Phys. Soc.* **36**, (1991), 2718.

Glatter, O. and Kratky, O. *Small Angle X-ray Scattering*. Academic Press INC., New York, 1982.

Goldin, M., Yerushalmi, J., Pfeffer, R., and Shinnar, R. *J. Fluid Mech.* **38**, (1969), 689.

Goodman, J.W. *J. Opt. Soc. Am.* **66**, (1976), 1145.

– *Speckle Phenomena in Optics*. Greenwood Village, USA: Roberts and Company Publishers, 2007.

– *Statistical Optics*. New York, USA: John Wiley and Sons. Inc., 2000.

Gordillo, J.M., Pérez-Saborid, M., and Gañán-Calvo, A.M. *J. Fluid. Mech.* **448**, (2001), 23.

Grisenti, R.E., Fraga, R.A. Costa, Petridis, N., Doerner, R., and Deppe, J. *Europhys. Lett.* **73**, (2006), 540.

Grohmann, N. *Wasser: Chemie, Mikrobiologie und nachhaltige Nutzung.* Oxford, University Press, 2011.

Grübel, G., Madsen, A., and Robert, A. *Soft-Matter Characterization.* New York, USA: Springer Science+Buisness Media, LLC, 2008. Chap. X-Ray Photon Correlation Spectroscopy (XPCS).

Grübel, G., Stephenson, G.B., Gutt, C., Sinn, H., and Tschentscher, Th. *Nuc. Instr. Meth. Phys. Res. B* **262**, (2007), 357.

Grübel, G. and Zontone, F. *J. Alloys Comp.* **362**, (2004), 3.

Guinier, A. and Fournet, G. *Small-Angle Scattering of X-Rays.* New York, USA: Wiley and Sons, Ltd, 1955.

Gunes, D.Z., Scirocco, R., Mewis, J., and Vermant, J. *J. Non-Newtonian Fluid Mech.* **155**, (2008), 39.

Gutt, C., Wochner, P., Fischer, B., Conrad, H., Castro-Colin, M., Lee, S., Lehmkühler, F., Steinke, I., Sprung, M., Roseker, W., Zhu, D., Lehmke, H., Bogle, S., Fuoss, P.H., Stephenson, G.B., Cammarata, M., Fritz, S.M., Robert, A., and Grübel, G. *Phys. Rev. Lett.* **108**, (2012), 024801.

Hansen, J.P. and Hayter, J.B. *Mol. Phys.* **46**, (1982), 651.

Head-Gordon, T. and Hura, G. *Chem. Rev.* **102**, (2002), 2651.

Head-Gordon, T. and Johnson, M.E. *PNAS* **103**, (2006), 7973.

Helmholz, H. *Monat. Königl. Preuss. Akad. Wiss. Berlin* **23**, (1886), 215.

Hinch, E.J. and Leal, L.G. *J. Fluid Mech.* **52**, (1972), 683.

Ho, B.P. and Leal, L.G. *J. Fluid Mech.* **65**, (1973), 365.

Hof, B., Westerweel, J, Schneider, T.M., and Eckhardt, B. *Nature* **443**, (2006), 59.

Hruszkewycz, S. O., Sutton, M., Fuoss, P.H., Adams, B., Rosenkranz, S., Jr, K.F. Ludwig, Roseker, W., Fritz, D., Cammarata, M., Zhu, D., Lee, S., Lemke, H., Gutt, C., Robert, A., Grübel, G., and Stephenson, G.B. *Phys. Rev. Lett.* **109**, (2012), 185502.

Huang, C., Wikfeldt, K.T., Tokushima, T., Nordlund, D., Harada, Y., Bergmann, U., Niebuhr, M., Weiss, T.M., Horikawa, Y., Leetmaa, M., Ljungberg, M.P., Takahashi, O., Lenz, A., Ojamäe, L., Lyubartsev, A.P., Shin, S., Petterson, L.G.M., and Nilsson, A. *PNAS* **106**, (2009), 15214.

Hura, G., Russo, D., Glaeser, R.M., Head-Gordon, T., Krack, M., and Parinello, M. *Phys. Chem. Chem. Phys.* **5**, (2003), 1981.

James, R.W. *The optical principles of the diffraction of X-rays.* Bell and sons, London, UK, 1948.

Jeffery, G.B. *Proc. R. Soc.* **A 102**, (1922), 161.

Jia, X., Li, Z., Sun, Z., and Lu, Z. *J. Phys. Chem. B* **115**, (2011), 13441.

Johansson, L.C. and al., et. *Nature Methods* **9**, (2012), 263.

Joung, C:G. *Rheol. Acta* **46**, (2006), 143.

Junaid, S., Qazi, S., Rennie, A.R., Wright, J.P., and Cockcroft, J.K. *Langmuir* **26**, (2010), 18701.

Kalman, D.P. and Wagner, N.J. *Rheol. Acta* **48**, (2009), 897.

Keller, J.B., Rubinow, S.I., and Tu, Y.O. *Phys. Fluids* **16**, (1973), 2052.

Kelvin, L. *Phil. Mag.* **42**, (1871), 362.

Kimmel, N. "Analysis of the charge collection process in solid state X-ray detectors." Dissertation. Universität Siegen, 2008.

Koopmann, R. et al. *Nature Methods* **9**, (2012), 259.

Kumar, P., Buldyrev, S.V., Becker, S.R., Poole, P.H., Starr, F.W., and Stanley, H.E. *PNAS* **104**, (2007), 9575.

Larson, R.G. *Soft Matter Physics: An Introduction*. New York: Springer-Verlag, New York, Inc., 2003.

– *The Structure and Rheology of Complex Fluids*. New York: Oxford University Press, 1999.

Lebowitz, J.L. and Percus, J.K. *Phys. Rev.* **144**, (1966), 251.

Leetmaa, M., Wikfeldt, K.T., Ljungberg, M.P., Odelius, M., Swenson, J., Nilsson, A., and Petterson, L.G.M. *J. Chem. Phys.* **129**, (2012), 084502.

Lehmkühler, F., Grübel, G., and Gutt, C. *App. Cryst.* **47**, (2014), 1315.

Leib, S.J. and Goldstein, M.E. *Phys. Fluids* **29**, (1986), 952.

Lengeler, B. *Naturwissenschaften* **88**, (2001), 249.

Lennard-Jones, J.E. *Prog. Phys. Soc.* **43**, (1931), 461.

Li, T., Donadio, D., and Galli, G. *Nature Com.* **4**, (2013), 1887.

Lin, S.P. *Breakup of Liquid Sheets and Jets, Chapter 7: Inviscid Jets*. Cambridge University Press, 2003.

Lin, S.P. and Reitz, R.D. *Annu. Rev. Fluid. Mech.* **30**, (1998), 85.

Lindner, P. and Zemb, T. *Modelling of small-angle scattering: Data from colloids and polymer systems*. New York, USA: Elsevier Science, 2002. Chap. X-Ray and Light: Scattering Methods Applied to Soft Condensed Matter.

Liu, Z. and Reitz, R.D. *Int. J. Multiphase Flow* **23**, (1996), 631.

Lomb, L. and al., et. *Phys. Rev. B* **84**, (2011), 214111.

Ludwig, R. *Angew. Chem. Int. Ed.* **40**, (2001), 1808.

Macosko, C.W. *Rheology Principles, Measurements, and Applications*. Toronto, Canada: Wiley-VCH, 1994.

MAnka, A., Pathak, H., Tanimura, S., Wölk, J., Stey, R., and Wyslouzil, B.E. *Phys. Chem. Chem. Phys.* **14**, (2012), 4505.

Maranzano, B.J. and Wagner, N.J. *J. Chem. Phys.* **117**, (2002), 10291.

Märkert, C., Fischer, B., and Wagner, J. *J. App. Cryst.* **44**, (2011), 441.

Marmiroli, B., Cacho-Nerin, F., Satori, B., Pérez, J., and Amenitsch, H. *J. Synch. Rad.* **21**, (2013), 1.

Martys, N.S., Khalil, M., George, W.L., Lootens, D., and Hebraud, P. *Eur. Phys. J. E* **35**, (2012), 20.

Meidinger, N., Andritschke, R., Hartmann, R., Herrmann, S., Holl, P., Lutz, G., and Strüder, L. *Nuc. Inst. Meth. Phys. Res. A* **565**, (2006), 251.

Melrose, J.R. and Ball, R.C. *J. Rheol.* **48**, (2004), 961.

Mishima, O. *J. Chem. Phys.* **133**, (2010), 144503.

Mishima, O. and Stanley, H.E. *Nature* **392**, (1998), 164.

Mittelbach, P. *Acta Physica Austriaca* **19**, (1964), 54.

Montanero, J.M., Gañán-Calvo, A.M., Acero, A.J., and Vega, E.J. *J. Micromech. Microeng.* **20**, (2010), 075035.

Montanero, J.M., Herrada, M.A., Ferrera, C., Vega, E.J., and Gañán-Calvo, A.M. *Phys. Fluids* **23**, (2011), 122103.

Murphy, W.K. and Sears, G.W. *J. Appl. Phys.* **35**, (1964), 1986.

Nilsson, A. and Petterson, L.G.M. *Chem. Phys.* **389**, (2011), 1.

Nugent, K.A. *Adv. Phys.* **59**, (2010), 1.

Ornstein, L.S. and Zernike, F. *KNAW Proceedings* **17**, (1914), 793.

Ozaki, M., Kratohvil, S., and Matijevic, E. *J. Colloid Interf. Sci.* **102**, (1984), 146.

Paschek, D., Rüppert, A., and Geiger, A. *Chem. Phys. Chem.* **9**, (2008), 2737.

Pasquino, R., Snijkers, F., Grizzuti, N., and Vermant, J. *Rheol Acta* **49**, (2010), 993.

Pauling, L. and Hendricks, S.B. *J. Am. Chem. Soc.* **47**, (1925), 781.

Pedrini, B., Menzel, A., Guizar-Sicairos, M., Guzenko, V.A., Gorelick, S., David, C., Patterson, B.D., and Abela, R. *Nature Com.* **4**, (2013), 1647.

Percus, J. K. and Yevick, G. *Phys. Rev.* **136**, (1964), 290.

Perlich, J., Rubeck, J., Botta, S., Gehrke, R., Roth, S.V., Ruderer, M.A., Prams, S.M., Rawolle, M., Zhong, Q., Körstgens, V., and Müller-Buschbaum, P. *Rev. Sci. Inst.* **81**, (2010), 105105.

Phalnikar, K.A., Kumar, R., and Alvi, F.S. *Exp. Fluids* **44**, (2008), 819.

Philippe, A.M., Baravian, C., Bezuglyy, V., Angilella, J.R., Meneau, F., Bihannic, I., and Michot, L.J. *Langmuir* **29**, (2013), 5315.

Poole, P.H., Sciortino, F., Essmann, U., and Stanley, H.E. *Nature* **360**, (1992), 324.

Pople, J.A. *Proc. R. Soc. A* **205**, (1951), 163.

Pylkkänen, T., Sakko, A., Hakala, M., Hämäläinen, Keeijo, Monaco, G., and Huotari, S. *J. Phys. Chem. B* **115**, (2011), 14544.

Rasmussen, D.H. and MacKenzie, A.P. *J. Chem. Phys.* **59**, (1973), 5003.

Rayleigh, L. *Proc. R. Soc. Lond.* **29**, (1879), 71.

– . *Proc. Lond. Math. Soc.* **S1-10**, (1878), 4–13.

Reitz, R.D. and Bracco, F.V. *The Encyclopedia of Fluid Mechanics, Chapter 10: Mechanisms of Breakup of Round Liquid Jets*. Gulf, Housten, 1986.

Reynolds, O. *Phil. Trans. R. Soc. Lond.* **174**, (1883), 935.

Robert, A. *Website, Beamline XCS*. 2014. URL: `https://portal.slac.stanford.edu/sites/lcls_public/instruments/xcs/Pages/Components.aspx`.

Robert, A., Curtis, R., Flath, D., Gray, A., Sirkorski, M., Song, S., Srinivasan, V., and Stefanescu, D. *J. Phys.: Conf. Ser.* **425**, (2013), 212009.

Röntgen, W.C. *Ann. Phys. Chem.* **45**, (1892), 91.

Roth, S.V., Döhrmann, R., Dommach, M., Kuhlmann, M., Kröger, I., Gerhke, R., Walter, H., Schroer, C., Lengeler, B., and Müller-Buschbaum, P. *Rev. Sci. Inst.* **77**, (2006), 085106.

Ruiz-Estrada, H. *Physica A* **168**, (1990), 919.

Russo, J. and Tanaka, H. *Nat. Com.* **5**, (2014), 3556.

Saldin, D.K., Poon, H.C., Bogan, M. J., Marchesini, S., Shapiro, D.A., Kirian, R.A., Weierstall, U., and Spence, J.C.H. *Phys. Rev. Lett.* **106**, (2011), 115501.

Saldin, D.K., Poon, H.C., Schwander, P., Uddin, M., and Schmidt, M. *Optics Express* **19**, (2011), 17318.

Saldin, D.K., Poon, H.C., Shneerson, V.L., Howells, M.R., Chapman, H.N., Kirian, R.A., Schmidt, K.E., and Spence, J.C.H. *New Journal of Physics* **12**, (2010), 035014.

Saldin, D.K., Shneerson, V.L., Howells, M.R., Marchesini, S., Chapman, H.N., Bogan, M., Shapiro, D., Kirian, R.A., Weierstall, U., Schmidt, K.E., and Spence, J.C.H. *New Journal of Physics* **12**, (2010), 035014.

Saldin, D.K., Shneerson, V.L., Starodub, D., and Spence, J.C.H. *Acta Cryst.* **A66**, (2010), 32.

Santos, I.S., Otter, W.K., and Briels, W.J. *J. Chem. Phys.* **137**, (2012), 204908.

Sastry, S., Debenedetti, PG., Sciortino, F., and Stanley, H.E. *Phys. Rev. E* **53**, (1996), 6144.

Schitzer, G.L. *Rev. Sci. Inst.* **62**, (1991), 2765.

Schulz, G. *Z. Phys. Chem.* **46**, (1949), 155.

Scirocco, R., Vermant, J., and Mewis, J. *J. Non-Newtonian Fluid Mech.* **117**, (2003), 183.

Scroggs, S.D. and Settles, G.S. *Exp. Fluids* **21**, (1996), 401.

Segre, G. and Selberberg, A. *Nature* **189**, (1961), 209.

Sellberg, J. A. "X-ray scattering and spectroscopy of supercooled water and ice." Dissertation. Stockholm University, 2014.

Sellberg, J. A. et al. *Nature* **510**, (2014), 381.

Send, S., Abboud, A., Hartmann, R., Huth, M., Leitenberger, W., Pashniak, N., Schmidt, J., Strüder, L., and Pietsch, U. *Nuc. Inst. Meth. Phys. Res. A* **711**, (2013), 132.

Si, T., Li, F., Yin, X., and Yin, X. *J. Fluid Mech.* **629**, (2009), 1.

Sierra, R.G. et al. *Acta Cryst. D* **68**, (2012), 1584.

Sinha, S.K., Tolan, M., and Gibaud, A. *Phys. Rev. B* **57**, (1998), 2740.

Smith, J.D., Cappa, C.D., Wilson, K.R., Messer, B.M., Cohen, R.C., and Saykally, R.J. *Science* **306**, (2004), 851.

Smith, R.S. and Kay, B.D. *Nature* **398**, (1999), 788.

Soper, A.K. and Ricci, M.A. *Phys. Rev. Lett.* **84**, (2000), 2881.

Speedy, R.J. *J. Phys. Chem.* **86**, (1982), 982.

Speedy, R.J. and Angell, C.A. *J. Chem. Phys.* **65**, (1976), 851.

Spence, J.C.H., Weierstall, U., and Chapman, H.N. *Rep. Prog. Phys.* **75**, (2012), 102601.

Spieß, L., Schwarzer, R., Behnken, H., and Teichert, G. *Moderne Röntgenbeugung*. B.G. Teubner Verlag/ GWV Fachverlag GmbH, 2005.

Sprung, M. *P10 Coherence Beamline User Guide*. 2014. URL: `http://photon-science.desy.de/sites/site_photonscience/content/e58/e176720/e177229/e178737/e179091/e179098/e219987/P10_User_Guide_v01102013_eng.pdf`.

Stanley, H.E., Teixeira, J., Geiger, A., and Blumberg, R.L. *Physica A* **106**, (1981), 260.

Sterling, A.M. and Sleicher, C.A. *J. Fluid Mech.* **68**, (1975), 477.

Stickel, J.J. and Powell, R.L. *Annu. Rev. Fluid Mech.* **37**, (2005), 129.

Stone, H.A. *Annu. Rev. Fluid Mech.* **26**, (1994), 65.

Strüder, L. and al., et. *Astron. Astrophys.* **365**, (2001), L18.

Sugimoto, T., Wang, Y., Itoh, H., and Muramatsu, A. *Colloids Surf. A* **134**, (1998), 265.

Sutton, M. *Evaluation of coherence factor for high Q data*. 2014. URL: `http://www.physics.mcgill.ca/~mark/coherence/yorick/highqbeta.pdf`.

Sutton, M., Mochrie, S.G.L., Greytak, T., Nageler, S.E., Berman, L.E., Held, G.A., and Stephenson, G.B. *Nature* **352**, (1991), 608.

Tagawa, Y., Oudalov, N., Visser, C.W., Peters, I.R., Meer, D. van der, Sun, C., Prosperetti, A., and Lohse, D. *Phys. Rev. X* **2**, (2012), 031002.

Timmann, A., Döhrmann, R., Schubert, T., Schulte-Schrepping, H., Hahn, U., Kuhlmann, M., Gehrke, R., Roth, S.V., Schopp, A., Schroer, C., and Lengeler, B. *Rev. Sci. Inst.* **80**, (2009), 046103.

Toennies, J.P. and Winkelmann, K. *J. Chem. Phys.* **66**, (1977), 3965.

Trebbin, M., Krüger, K., Deponte, D.P., Roth, S.V., Chapman, H.N., and Förster, S. *Lab on a Chip* **14**, (2014), 1733.

Trebbin, M., Steinhauser, D., Perlich, J., Buffet, A., Rith, A.V., Zimmermann, W., Thiele, J., and Förster, S. *PNAS* **110**, (2012), 6706.

Tropea, C., Yarin, A., and Foss, J.F. *Hanbook of Experimental Fluid Mechanics; Band1*. Springer-Verlag Berlin Heidelberg, 2007.

Veen, F. Van der and Pfeiffer, F. *J. Phys.: Condens Matter* **16**, (2004), 5003.

Vega, E.J., Montanero, J.M., Herrada, M.A., and Gañán-Calvo, A.M. *Phys. Fluids* **22**, (2010), 064105.

Vermant, J. and Solomon, M.J. *J. Phys.: Condense Matter* **17**, (2005), R187.

Wagner, J. *J. Appl. Cryst.* **37**, (2004), 750.

Wagner, N.J. and Brady, J.F. *Physics Today* **62**, (2009), 27.

Wang, D., Weierstall, U., Pollack, L., and Spence, J. *J. Synchrotron Rad.* **21**, (2014).

Wang, X., Kruis, F.E., and McMurry, P.H. *Aerosol Sci. Technol.* **39**, (2005), 611.

Warren, B.E. *X-Ray diffraction.* Addison-Wesley, 1969.

Weber, C. Z. *Angw. Math. Mech.* **2**, (1931), 136.

Wegner, S., Börzsönyi, T., Bien, T., Rose, G., and Stannarius, R. *Soft Matter* **8**, (2012), 10950.

Weierstall, U., Doak, R.B., Spence, J.C.H., Starodub, D., Shapiro, D., Kennedy, P., Warner, J., Hembree, G.G., Fromme, P., and Chapman, H.N. *Exp. Fluids* **44**, (2008), 675.

Wernet, Ph., Nordlund, D., Bergmann, U., Cavalleri, M., Odelius, M., Ogasawara, H., Näslund, L.A., Hirsch, T.K., Ojamäe, L., Glatzel, P., Petterson, L.G.M., and Nilsson, A. *Science* **304**, (2004), 995.

Wikfeldt, K.T., Leetmaa, M., Ljungberg, M.P., Nilsson, A., and Petterson, L.G.M. *J. Phys. Chem. B* **113**, (2009), 6246.

Wilson, K.R., Rude, B.S., Smith, J., Cappa, C., and Co, D.T. *Rev. Sci. Inst.* **75**, (2004), 725.

Wochner, P., Castro-Colin, M., Bogle, S., and Bugaev, V. *Int. J. Mat Res.* **106**, (2011), 874.

Wochner, P., Gutt, C., Autenrieth, T., Demmer, T., Bugaev, V., Ortiz, A.D., Duri, A., Zontone, F., Grübel, G., and Dosch, H. *PNAS* **106**, (2009), 11511.

Wygnanski, I., Sokolov, M., and Friedman, D. *J. Fluid Mech.* **69**, (1975), 283.

Xu, L., Kumar, P., Buldyrev, S.V., Chen, S.H., Poole, P.H., Sciortino, F., and Stanley, H.E. *PNAS* **102**, (2005), 16558.

List of Figures

List of Tables

Publications

1. S. Lee, W. Roseker, C. Gutt, B. Fischer, H. Conrad, F. Lehmkühler, **I. Steinke**, D. Zhu, H. Lemke, M. Cammarata, D.M. Fritz, P. Wochner, M. Castro-Colin S.O. Hruskewycz, P.H. Fuoss, G.B. Stephenson, G. Grübel, and A. Robert. Single shot speckle and coherence analysis of the hard X-ray free electron laser LCLS. OPTICS EXPRESS, **21**, 024647 (2013).

2. C. Gutt, P. Wochner, B. Fischer, H. Conrad, M. Castro-Colin, S. Lee, F. Lehmkühler, **I. Steinke**, M. Sprung, W. Roseker, D. Zhu, H. Lemke, S. Bogle, P.H. Fouss, G.B. Stephenson, M. Cammarata, D.M. Fritz, A. Robert, and G. Grübel. Single shot Spatial and Temporal Coherence Properties of the SLAC Linac Coherent Light Source in the Hard X-Ray Regime. Phys. Rev. Lett., **108**, 024801 (2012).

3. F. Lehmkühler, A. Sakko, **I. Steinke**, C. Sternemann, M. Hakala, C.J. Sahle, T. Buslaps, L. Simonelli, S. Galambosi, M. Paulus, T. Pylkkänen, M. Tolan, and K. Hämäläinen, Temperature-Induced Structural Changes of Tetrahydrofuran Clathrate and of the Liquid Water/Tetrahydrofuran Mixture, J. Phys. Chem. C, **115**, 21009 (2011).

4. F. Lehmkühler, A. Sakko, C. Sternemann, M. Hakala, K. Nygard, C.J. Sahle, A. Galambosi, **I. Steinke**, S. Tiemeyer, A. Nyrow, T. Buslaps, D. Pontoni, M. Tolan, and K Hämäläinen, Anomalous Energetics in Tetrahydrofuran Clathrate Hydrate Revealed by X-ray Compton Scattering, J. Phys. Chem. Lett., **1**, 2832 (2010).

Acknowledgments

Eidesstattliche Erklärung

Hiermit erkläre ich an Eides Statt, dass ich die vorliegende Doktorarbeit meine eigene Arbeit ist, abgesehen von der verwendeten Literatur und der Beratung durch meine wissenschaftlichen Betreuer. Sie wurde weder ganz noch in Teilen an anderer Stelle im Rahmen eines Prüfungsverfahrens vorgelegt.

Hamburg, den

(Ingo Steinke)